Study of Magnetic Tunnel Junction based Gradiometric Sensor for Magnetic Flux Leakage Testing

Study of Magnetic Tunnel Junction Based Gradiometric Sensor for Magnetic Flux Leakage Testing

Department of Applied Physics

Graduate School of Engineering

TOHOKU UNIVERSITY

Muhamad Arif Ihsan bin Mohd Noor Sam

Supervisor: Professor Hiroaki Matsueda

Contents

Chapter 1: Introduction

1.1 Non-destructive Testing

Non-destructive testing (NDT) is the process of inspecting or evaluating a material for defects or damages without causing any destroying the tested material or system. Used in manufacturing, fabrication and inspections to ensure product integrity and reliability, to control manufacturing processes, lower production costs and to maintain a uniform quality level of a wide range of industrial components such as power generation [1], automotive [2], and railway [3] where the failure of components may result on human, economic or environmental losses, such as airplane crashes and derailments.

1.2 Methods of Non-destructive Testing

There are several NDT methods available such as, visual inspection, dye penetrants, X-ray, ultrasonic testing, and magnetic flux leakage (MFL) testing. The difference between these NDT methods is the physical concept of each method and the way they are able to detect the defects of the inspected material.

Visual inspection [4] is based on the part examination by a qualified operator following a specific procedure, being often applied to electronics system boards and aircrafts engines. However, due to human limitations, the use of accessories such magnifying glasses are necessary in order to aid the operator to inspect the part under test minutely. However, there is always a possibility that some defects are unable to be detected.

Dye penetrant method is commonly used to reveal surface cracks by using a colour dye. The technique is based on the ability of a liquid to be drawn into a ‘clean’ surface breaking flaw by capillary action [5]. Consequently, the part under test is carefully cleaned to remove the excess penetrant from the surface, leaving a portion of the solution

housed on the superficial defects. The penetrant solution stuck into the flaw can be readily highlighted using a proper developer.

NDT systems based on radiography methods requiring a radiation source and a proper detector, being often used to detect internal voids on welded joints [6]. The part under test is submitted to the radiation, while an imaging media is positioned behind it. Consequently, different absorptions of the incident radiation along the material reveals the defects.

Ultrasonic methods [7] rely on the dissemination of acoustic waves on the part under test. A high frequency wave is introduced into the part by an emitter. When the wave hits a material with an anomaly, the acoustic waves reflect, and detected by a receiver. The modification of the acoustic wave reflection intensity allows to locate internal defects and its depth on the part under test.

The concept behind MFL [8] is detecting the leaking of magnetic flux using a magnetic sensor. The target is first magnetized, and a magnetic sensor is passed along the target. The presence of an anomaly or defect will cause the magnetic flux to leak, and it will be picked up by the sensor. From the signal obtained, the presence and position of the fracture(s) will be determined.

1.3 Magnetic Flux Leakage

In MFL technique [9], the tested material or component is uniformly magnetized. If any defect is present in the object, magnetic flux lines leak out of the object surface around the defect. The leakage flux can be detected using magnetic field sensors.

Success of MFL testing depends on several factors such as, proper magnetization of the object, detection of the magnetic flux leakage using a suitable sensor, and the distance between the sensor and the tested material or lift-off value. It is necessary to ensure that the magnetisation is perpendicular to the expected orientation of the defects such that the magnetic flux leakage field is produced at the surface of the object, for detection by the sensor. When the magnetic field is small, the magnetic flux lines are not

able to come out of the defect region. However, if the magnetic field is large, the flux leakage may be masked by the surface noise.

Lift-off value is an important factor for detection of defects in MFL testing. Lift-off value affects the magnetisation level and the signal shape. A large lift-off value will result in a decrease in the MFL signal amplitude, thus making more difficult to detect the presence of defects. Ideally, constant and a minimum lift-off value is always preferred.

1.3.1 Magnetic Flux Leakage Testing Theory

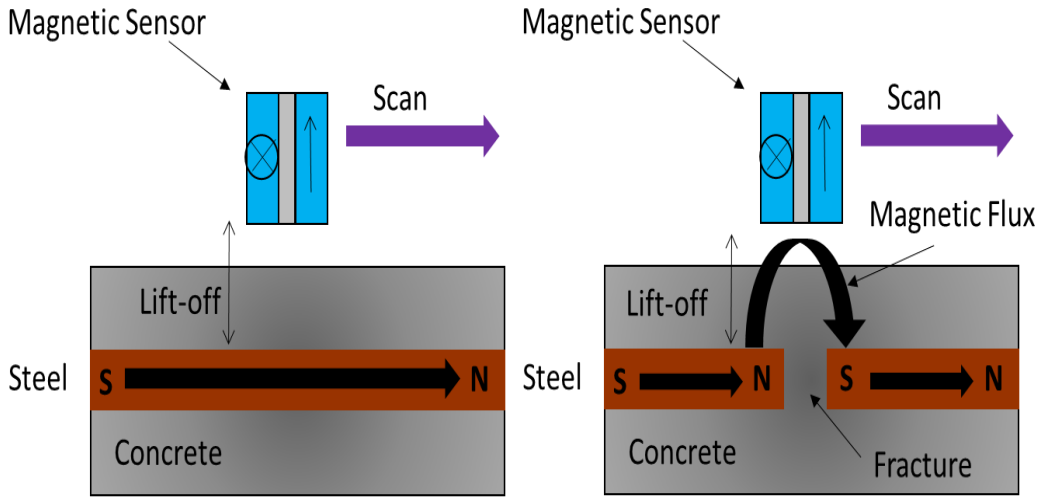

Figure 1.1: Representation of the MFL measurement. Figure on the left shows the situation when there are no fractures in the steel rebar. Figure in the right shows when a fracture is present.

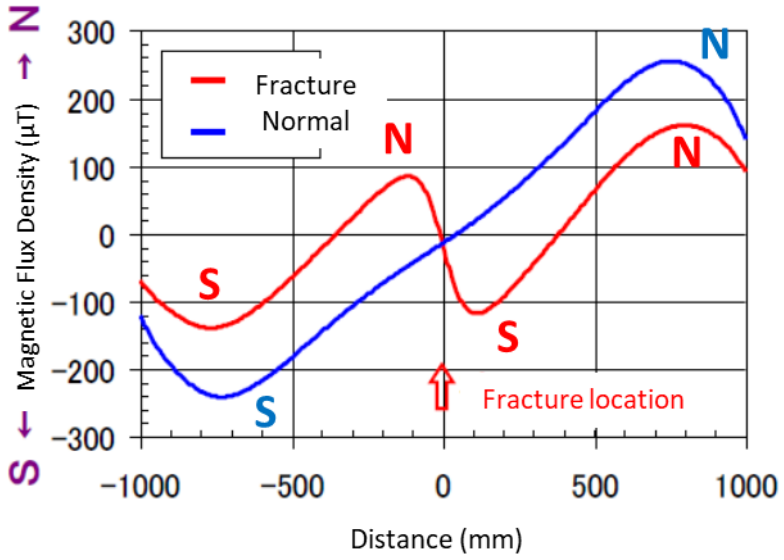

Figure 1.2: Example of the signal obtained from measurement of sample that has no fractures (blue) and sample that has a fracture (red). [9]

As shown in Figure 1.1, when the reinforced concrete is magnetized, the process will turn the steel rebar into a pseudo-permanent magnet. After the magnetization process, a magnetic sensor is moved along the concrete surface. In the normal case, the magnetic flux flow will be like that of a bar magnet i.e., from the South Pole to the North Pole of the magnet. Therefore, as seen in Figure 1.2, the magnetic flux density will increase accordingly from South Pole to the North Pole, resulting in a linearly increasing graph.

However, when there are fractures in the steel rebar, this will change the geometry of the pseudo-bar magnet. For example, in Figure 1.1, the fracture will split the steel rebar into two, resulting in two pseudo-bar magnets. The magnetic flux flow will also change because of the interaction of the two different poles at the location of the fracture. Therefore, as in Figure 1.2, since there are two pseudo-bar magnets as aforementioned, the signal read by the sensor will result in two linear graphs. However, at the point of interaction a "leak" in the magnetic flux occurs where the graph dips because of the difference in the magnetic flux density. By analysing the signal and identifying the peak(s) and trough(s) in the signal obtained by the magnetic sensor, the presence and location of fractures can be determined.

1.3.2 Mathematical Approach

The magnetic flux at the fracture can be observed from a mathematical approach. From Figure 1.3, the assumption is that at the fracture location, there are two different magnetic poles or "magnetic dipoles" due to the different poles of the bar magnets.

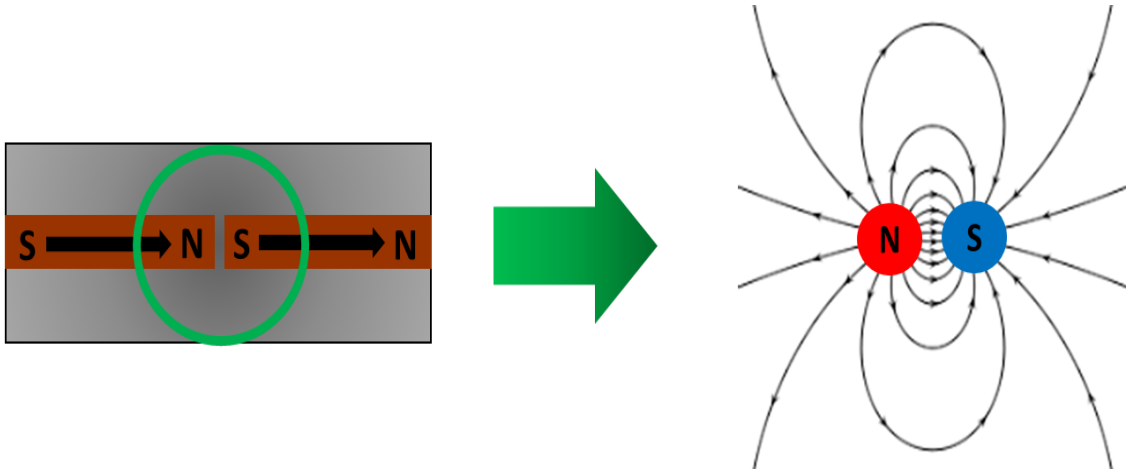

Figure 1.3: Mathematical approach of the different magnetic poles due to the presence of fracture in the steel rebar

The magnetic dipoles can be seen from an electrostatic analog for a magnetic moment: two opposing charges separated by a finite distance. The magnetic field of magnetic dipole depends on the strength and direction of a magnet's magnetic moment $\boldsymbol{m}$ but drops off as the cube of the distance such that:

$$\boldsymbol{H}(\boldsymbol{r}) = \frac{1}{4\pi}\frac{3\boldsymbol{r}(\boldsymbol{m}\cdot\boldsymbol{r})}{|\boldsymbol{r}|^5} - \frac{\boldsymbol{m}}{|\boldsymbol{r}|^3} \qquad \textbf{1.1}$$

where $\boldsymbol{H}$ is the magnetic field produced and $\boldsymbol{r}$ is a vector from the centre of the magnetic dipole location where it is measured. The inverse cube nature of this equation is more readily seen by expressing the location vector $\boldsymbol{r}$ as the product of its magnitude times the unit vector in its direction ($\boldsymbol{r} = |\boldsymbol{r}|\boldsymbol{n}$) so that:

$$\boldsymbol{H}(\boldsymbol{r}) = \frac{1}{4\pi}\frac{3\boldsymbol{n}(\boldsymbol{n}\cdot\boldsymbol{m}) - \boldsymbol{m}}{|\boldsymbol{r}|^3} \qquad \textbf{1.2}$$

From here, the magnetic flux density can be obtained by $\mu_0\boldsymbol{H} = \boldsymbol{B}$:

$$\boldsymbol{B}(\boldsymbol{r}) = \frac{\mu_0}{4\pi}\frac{3\boldsymbol{n}(\boldsymbol{n}\cdot\boldsymbol{m}) - \boldsymbol{m}}{|\boldsymbol{r}|^3} \qquad \textbf{1.3}$$

What could be understood for the equations above is that as the distance of the fracture from the magnetic sensor (lift-off) increases, the magnetic flux density decreases or weakens. Therefore, a magnetic sensor with high sensitivity is required for deeper fractures as it is located further away from the concrete's surface.

1.4 Magnetic Sensors

1.4.1 Hall Sensors

Hall sensors can detect variation of magnetic fields using the Hall-effect, which was discovered by Edwin Hall in 1879 [10]. He discovered that a voltage difference appears across a thin rectangle of conductor placed in an applied magnetic field perpendicular to the plane of the rectangle when an electric current flows along its length. As shown in Figure 1.8, when an electric current flows through a magnetic field, Lorentz force acts on electron motion and make it parallel to the applied magnetic field direction. Consequently, the induced voltage is proportional to applied magnetic field strength. Since Hall sensors show their sensitivity range in the mT range, low cost, and an ability

to be easily miniaturized an integrated within circuits, they are widely used in a variety field.

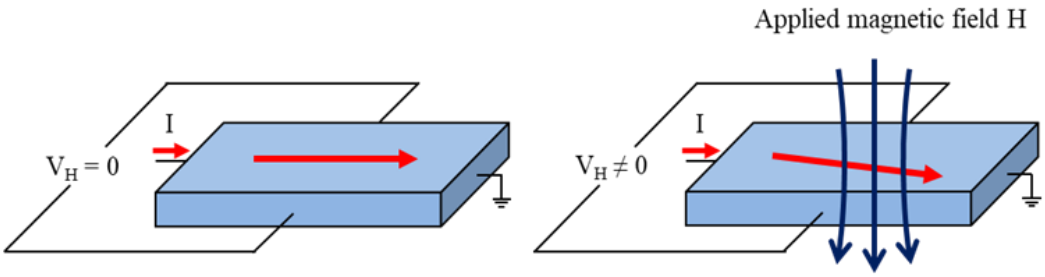

Figure 1.4: Schematic diagram of a Hall sensor. The induced hall voltage V_H is depends on applied magnetic field.

1.4.2 Magneto Impedance Sensors

Magneto-impedance (MI) sensors are high sensitivity magnetic sensor, which take advantage of magnetic impedance effect to detect external magnetic field. When a high frequency current or pulse current is applied this causes a skin effect on the magnetic material, the impedance of a magnetic material (FeCoSiB alloy) will be determined by the strength of external magnetic field. Typically, a morphemes wire is used as the magnetic material, the effect is particularly marked. As shown in Figure 1.5 [11], when an applied current flows through the amorphous wire, the reaction relative to the variation of external magnetic field can be detected by a pickup coil. Owing to ultra-high sensitivity and compatibility with electric circuit, magneto impedance sensors are widely used to detect variation of magnetic field as smaller as 0.1 nT. However, due to skin effect in ferromagnetic material, the reaction relative to external magnetic field closely depends on field frequency, and it is insensitive to the variation of external magnetic field when a high frequency external field is applied.

The MI is usually quantified as the ratio of impedance change, and its maximum value (at each frequency), given by [12]

$$MI_{max}(\%) = \frac{Z_{max} - Z_{min}}{Z_{min}} \times 100 \qquad \textbf{1.4}$$

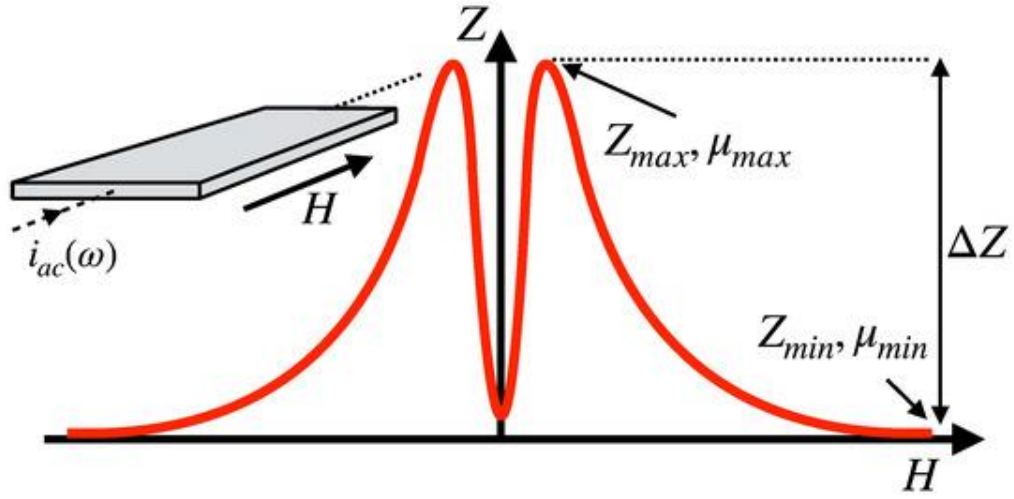

Figure 1.5: Sketch of the dependence of the impedance on the applied magnetic field in a soft magnetic sample with transverse anisotropy (in-plane easy axis, perpendicular to the current flow and the applied field).

1.4.3 Magnetoresistance Sensors

Magnetoresistance is the tendency of a material (preferably ferromagnetic) to change the value of its electrical resistance in an externally applied magnetic field. According to the applied magnetic field intensity and orientation, the material will change its electrical resistance which lies in a range limited by a maximum (R_{max}) and minimum (R_{min}). Therefore, the magnetoresistive effect can be expressed by the change in resistance (ΔR) relative to the minimum resistance which is the reference value.

$$MR = \frac{R_{\max} - R_{\min}}{R_{\min}} = \frac{\Delta R}{R_{\min}} \qquad \textbf{1.5}$$

In multicomponent or multilayer systems which are applied in thin film magnetic sensor technologies, anisotropic magnetoresistance (AMR), giant magnetoresistance (GMR), or tunnel magnetoresistance (TMR) can be observed.

1.4.3.1 Anisotropic Magnetoresistance

Discovered in 1857 by William Thomson [13], anisotropic magnetoresistance describes the property of a material in which the electric resistance changes according to the angle between the direction of the electric current and the direction of magnetization [14].

AMR effect arises from the spin-orbit coupling electrons in *d* orbitals deforming slightly as the direction of the magnetization rotates. As a result of, it changes the amount of scattering undergone by the conduction electrons along the lattice [15]. A low resistance state occurs when the field and the magnetization are transverse to the electric current flow, where the electronic orbits are in the plane of the current and there is a small cross-section for scattering. On the other hand, when the magnetic fields are parallel to the electric current, the electronic orbits are oriented perpendicular to the current and the cross-section for scattering is increased, resulting in a high resistance state, as shown in Figure 1.6.

The AMR effect is used in a wide of array of sensors for measurement of Earth's magnetic field (electronic compass), for electric current measuring (by measuring the magnetic field created around the conductor), for traffic detection and for linear position and angle sensing.

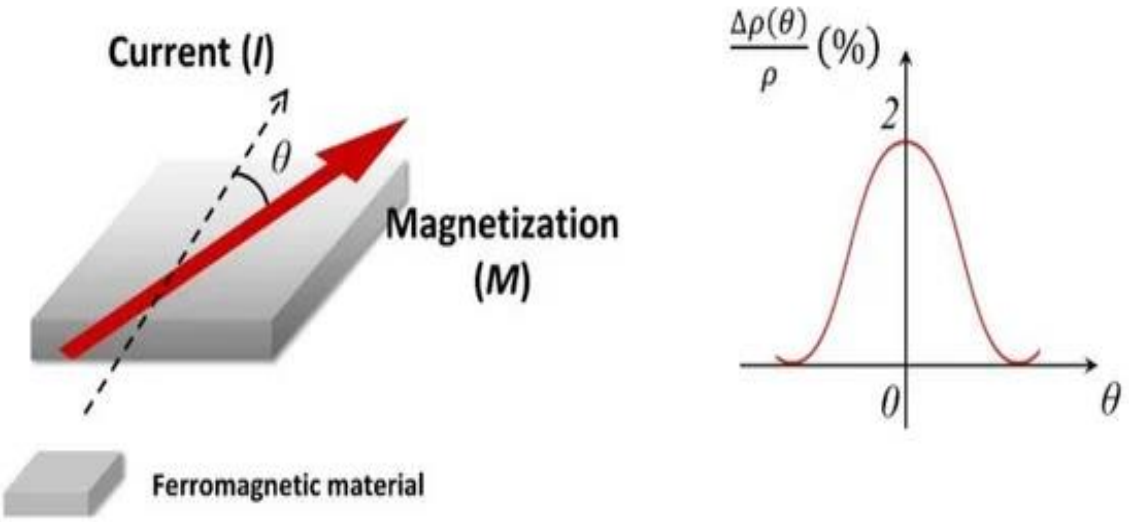

Figure 1.6: Schematic diagram of anisotropic magnetoresistance (AMR) [16].

1.4.3.2 Giant Magnetoresistance

Giant magnetoresistance is a quantum mechanical magnetoresistance effect observed in multilayers composed of alternating ferromagnetic and non-magnetic conductive layers. It was discovered in 1988 by A. Fert [17] and P. Grunberg [18]. The effect is observed as a significant change in the electrical resistance depending on whether the magnetization of adjacent ferromagnetic layers is in a parallel or an antiparallel alignment. The overall resistance is low for parallel alignment and high for antiparallel alignment. By applying an external magnetic field, the magnetization direction can be controlled.

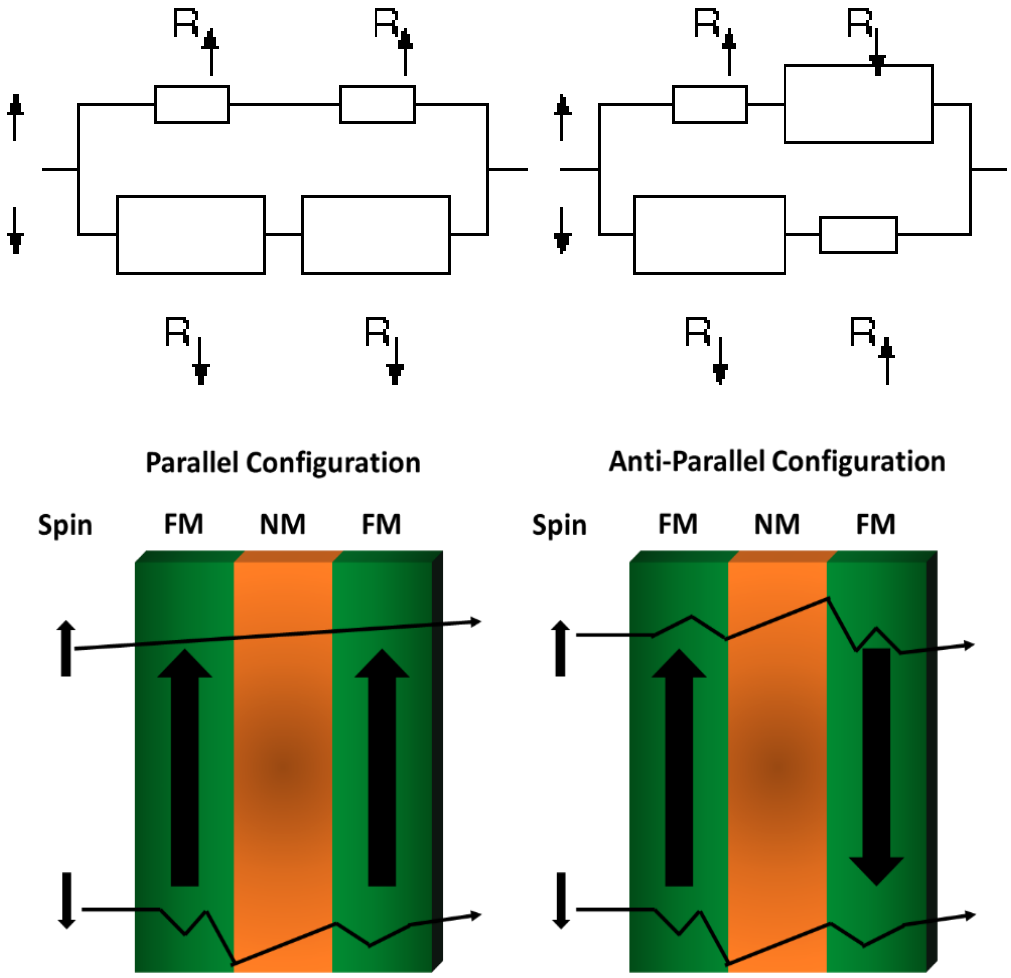

Figure 1.7: (Top) The electric circuit shows the equivalent resistances of each respective states. (Bottom) Diagram shows the scattering of the spin-up and spin-down electrons according to the different orientation of magnetization of the ferromagnetic layers.

The GMR effect is based on the spin-dependent scattering at the non-magnetic/ferromagnetic interfaces, where the total resistance comes from the spin-up and spin-down electrons (two current model) [19]. Based on Figure 1.7, when the magnetization of the ferromagnetic layers is in a parallel orientation, spin-up conduction electrons are weakly scattered while spin-down electrons are strongly scattered, resulting in a low resistance state. In the antiparallel configuration, both spin-up and spin-down electrons are strongly scattered, thus a high resistance state is formed.

The main application of GMR is magnetic field sensors, which are used in hard disk drives to read data, microelectromechanical systems (MEMS) and other devices.

1.4.3.3 Tunnel Magnetoresistance

Magnetic tunnel junctions (MTJs) are magnetoresistive sensors based on ferromagnetic/insulator multilayer structure. When a voltage or current is applied to the ferromagnetic electrodes, the electrons will flow from one electrode, across the insulator (barrier), into the other electrode. Since this process is forbidden in classical physics, the tunnel magnetoresistance is strictly a quantum mechanical phenomenon.

In spin-dependent tunnelling effect, observed and interpreted by M.Julliere in 1975 [20] (later known as the Julierre model), the tunnelling current depends on the relative orientation of the magnetizations of the ferromagnetic layers [21]. By assuming the spin is conserved during the tunnelling process, the current can be described in a two-current model [22]. The total current is split in two partial currents, one for the spin-up electrons and the other for the spin-down electrons.

At the Fermi level, ferromagnetic materials have a strong spin imbalance, this means each density of states for the spins are different. Therefore, when the magnetization directions of the two ferromagnetic layers are facing the same direction (parallel state), tunnelling occurs between majority spin states and between minority spin states of each respective layer, resulting in a low resistance state. However, when the magnetization directions are facing in opposite directions (anti-parallel state), tunnelling occurs between

majority/minority spin states of one layer to minority/majority spin states of the other, resulting in high resistance state.

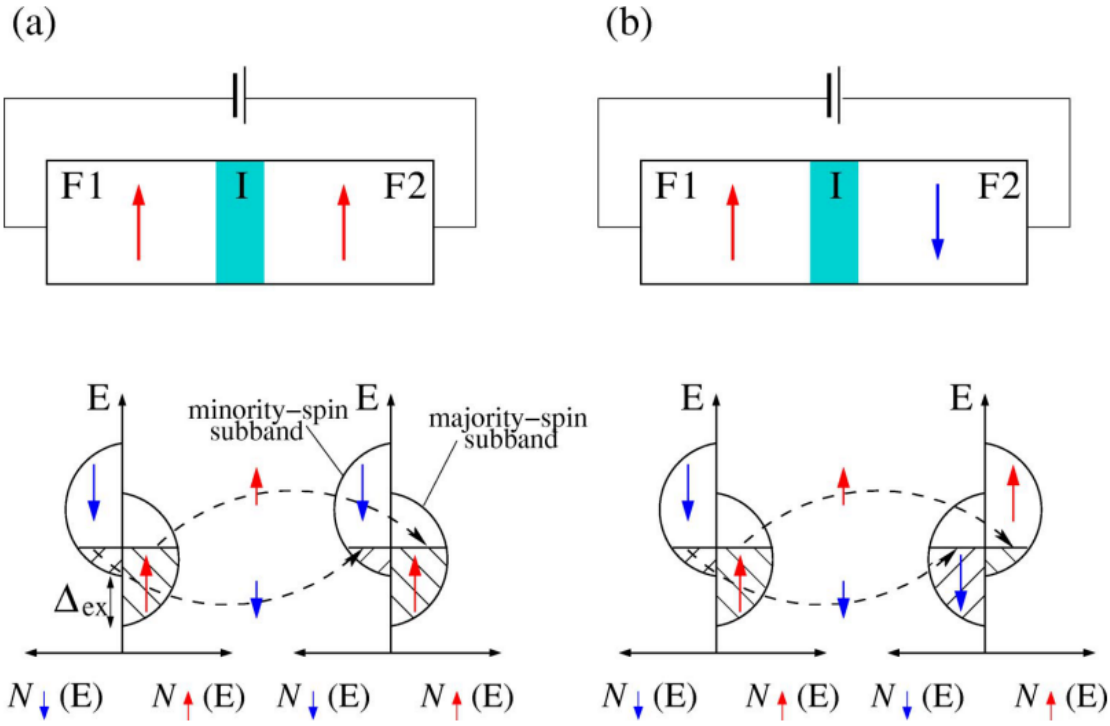

Figure 1.8: Schematic illustration of electron tunnelling in ferromagnet / insulator / ferromagnet (F/I/F) tunnel junctions and two current model for parallel (a) and anti-parallel (b) alignment of the magnetizations with the corresponding spin resolved density of the d states in ferromagnetic metals that have exchange spin splitting Δ_{ex}. Arrows in the two ferromagnetic regions are determined by the majority-spin sub-band. Dashed lines depict spin-conserved tunnelling [23]

The spin polarization P is calculated from the spin dependent density of states (DOS) D at the Fermi energy:

$$P = \frac{D_{\uparrow}(E_{\mathrm{F}}) - D_{\downarrow}(E_{\mathrm{F}})}{D_{\uparrow}(E_{\mathrm{F}}) + D_{\downarrow}(E_{\mathrm{F}})} \qquad \textbf{1.6}$$

The relative resistance change is given by the spin polarizations of the two ferromagnets, P_1 and P_2:

$$\mathrm{TMR} = \frac{2P_1P_2}{1 - P_1P_2} = \frac{R_{\mathrm{AP}} - R_{\mathrm{P}}}{R_{\mathrm{P}}} \qquad \textbf{1.7}$$

The TMR ratio can be defined as:

$$\mathrm{TMR} = \frac{R_{\mathrm{AP}} - R_{\mathrm{P}}}{R_{\mathrm{P}}} \qquad \textbf{1.8}$$

where R_{AP} is the electrical resistance in the anti-parallel state, whereas R_P is the resistance in the parallel state.

1.5 Magnetic Tunnel Junctions

1.5.1 MTJ Structures

Basic Structure

The basic structure of a magnetic tunnel junction consists of two ferromagnetic layers separated by a thin insulating barrier, where one layer has its magnetization direction fixed (pinned layer) by an adjacent antiferromagnetic layer, while the other is free to rotate (free layer) according to the applied external magnetic field. The magnetization of the pinned layer (ferromagnetic layer) is fixed in a certain direction due to an exchange coupling (exchange bias effect [24]) at the antiferromagnetic/ferromagnetic interface.

In real structures, buffer layers or seed layers are inserted to enhance the crystal texture and the smoothness of the interface, which has shown to improve the magnetic tunnel junction properties [25]. To prevent corrosion and oxidation of the structure, a thin cap layer or cover layer [26].

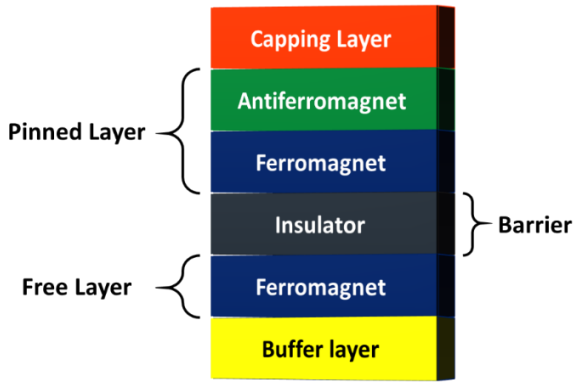

Figure 1.9: Basic structure of a MTJ sensor

Synthetic Antiferromagnet Structures

Synthetic Antiferromagnet (SAF) pinned layers [27], were used to enhance the exchange bias field, improve the thermal properties, resulting in a structure with a higher magnetic stability and slow decrease of the pinning field with increasing temperature respectively. Another advantage of the SAF structure is because of if its lower net moment [28], it is able to reduce the magnetostatic coupling between free and the pinned layer.

The SAF consists of two ferromagnetic layers (FM1 and FM2) sandwiching a thin nonmagnetic layer (NM). The ferromagnetic layer that is alongside the Antiferromagnet (pinning layer) is pinned through exchange coupling, while the FM2 (reference layer – RF) is antiferromagnetically coupled to FM1 (pinned layer – PL) as described by RKKY theory [29], which states that the coupling oscillates between ferromagnetic and antiferromagnetic according to the thickness of the nonmagnetic layer.

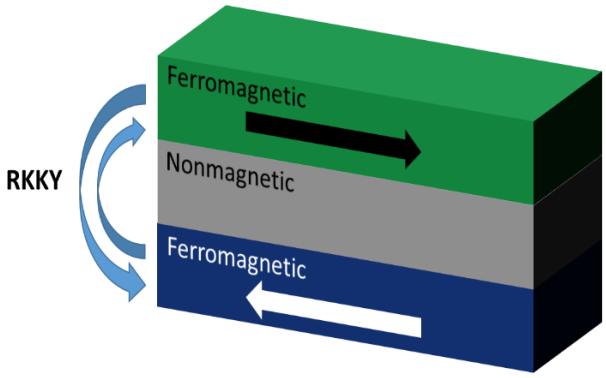

Figure 1.10: Schematic of synthetic antiferromagnets

Magnetic Tunnel Junction based on MgO (001) barrier

In 2001, a theoretical study based on first-principles calculation predicted that an extremely high TMR ratio can be observed for Fe/MgO/Fe trilayers, where the insulating barrier is a crystalline MgO layer with (001) texture [30]. The result shows that a coherent lattice matching between the (001) plane of body-centered cubic (bcc) Fe and the (001) plane of MgO results in a spin-dependent match between evanescent states within the tunnel barrier and electronic states of the Fe electrode. Figure 1.11(a) illustrates the

tunneling in a MTJ with an amorphous AlO barrier, the Fe layer (001) was deposited as the top electrode. Due to the amorphous AlO barrier, the crystallographic symmetry is nonexistent in the barrier and Bloch states with various symmetries can couple with evanescent states in AlO and restrain the tunneling effect. This tunneling process can be regarded as an incoherent tunneling [23]. Usually, in 3d ferromagnetic materials, Bloch sates with Δ_1 and Δ_2 symmetries have totally different spin polarization at Fermi level E_F. Julliere's model assumes that tunnelling probabilities are equal for all the Bloch states in the electrodes, and none of the momentum and coherency of Bloch states can be conserved in this incoherent tunneling. However, some experiments show inconsistent results [31][32], which indicates tunneling probability in actual MTJs depends on the symmetry of each Bloch sate. In addition, considering that the Δ_1 Bloch states with higher spin polarization and offer higher tunneling probability compare with other Bloch states [33][34] if only the highly spin-polarized Δ_1 states coherently tunnel through a barrier, as shown in Figure 1. 11(b), a very high spin polarization of tunneling current as well as a very high MR ratio can be obtained. Furthermore, as shown in Figure 1.12, because small lattice mismatch between bcc Fe (001) layer and a crystalline MgO (001) barrier layer, a perfect barrier layer can be epitaxially grown in an MTJ.

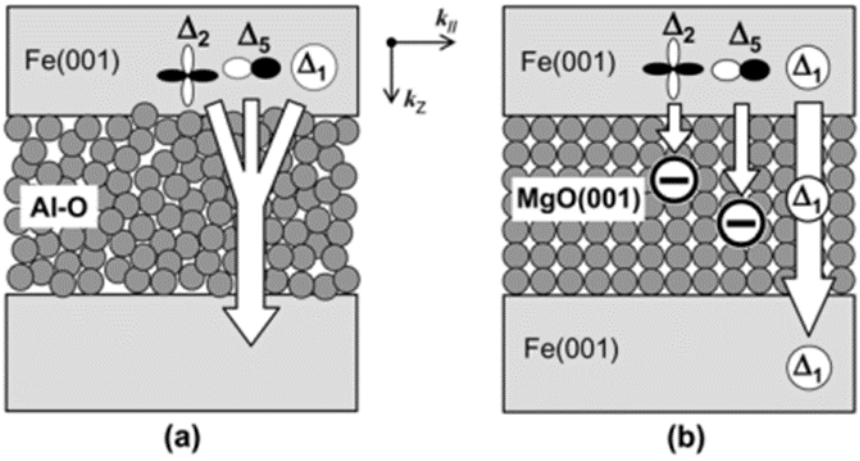

Figure 1.11: Schematic illustrations of electron tunnelling through (a) an amorphous Al-O barrier and (b) a crystalline MgO (001) barrier [23].

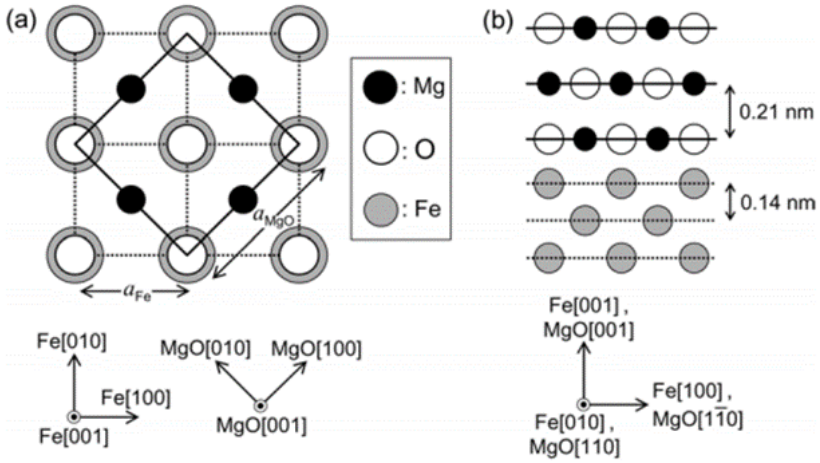

Figure 1.12: Crystallographic relationship and interface structure of epitaxial bcc Fe (001)/NaCl-type MgO (001): (a) top view and (b) cross-sectional view. a_{Fe} and a_{MgO} denote the lattice constants of bcc Fe and NaCl-type MgO unit cells.

More importantly, the coherent tunneling can be realized in this MTJ, which the Δ_1 states are theoretically expected to dominantly tunnel through the barrier layer [30][35]. For the $k_{\parallel} = 0$ direction ([001] direction in this case), in which the tunnelling probability is the highest, there are three kinds of evanescent states (tunnelling states) in the band gap of MgO (001): Δ_1, Δ_5 and $\Delta_{2'}$. Figure 1.13 exhibits the partial DOS for the decaying evanescent states in an MgO barrier layer in the case of parallel magnetic alignment [30]. Bloch states Δ_1, Δ_5 and Δ_2 show different decays in barrier layer, and the slowest decay can be observed for Δ_1 states, therefore we can expect the dominant tunnelling channel is determined by Δ_1 states. Band dispersion of bcc Fe for the [001] ($k_{\parallel} = 0$) direction is shown in Figure 1.14, because Fe Δ_1 band have high spin polarization at E_F, a high TMR ratio can be obtained in the epitaxial Fe (001)/MgO (001)/Fe (001) MTJ is when Δ_1 electrons dominantly tunnel. Also, Figure 1.15 shows the tunnelling probability as a function of $k_{\parallel}$ wave vectors (k_x and k_y). Different spin conductance can occur for P and AP states. Because the spikes of tunnelling probability appear at finite $k_{\parallel}$ points for the minority-spin conductance in P and AP sates, the tunnelling conductance in the AP state is much smaller than that in the P state, which results in high MR ratio. Thus, an epitaxial MTJ with a crystalline MgO (001) tunnel barrier is the ideal device which can offer high TMR ratio.

Therefore, some studies have been focusing attention to MTJ with crystalline MgO (001) barrier. M. Bowen *et al*. reported that as high as 60% of TMR ratio was observed in MTJ of Fe/MgO/Fe trilayers at 30K [36]. Their result proved that the spin polarization of tunneling electrons is closely depends on the actual electronic structure of the entire electrode/barrier system. The improved crystal perfection and orientation for MgO (001) barrier are very likely to lead to even higher TMR values. Furthermore, Yuasa *et al*. proposed a high MR ratio up to 180% at room temperature in single-crystal Fe/MgO/Fe MTJs, deposited by using molecular beam epitaxy (MBE) [37]. The obtained giant TMR effect is correlated to symmetry of electron wave function in spin-polarized tunneling.

Moreover, they showed that TMR oscillates significantly as a function of MgO barrier thickness, indicating that coherency of wave functions is conserved across the MgO barrier. These results suggested that achieving (001)-oriented single-crystal MgO barrier and good band matching between MgO barrier and electrode play critical roles for improving TMR in MTJ. Therefore, MTJs based on MgO barrier layer have attracted much attention, which enabled us to design and use MTJ to measure change of external field with high output signal [38].

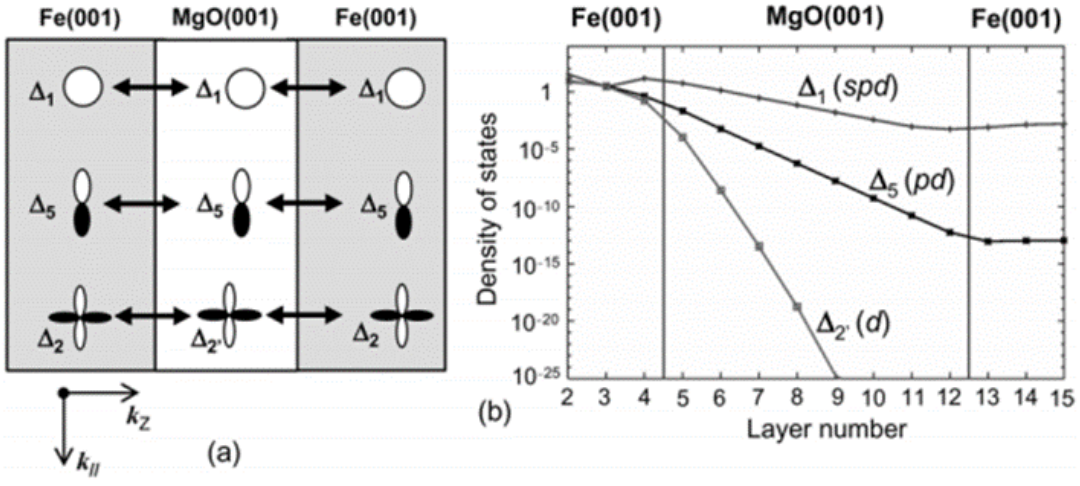

Figure 1.13: (a) Coupling of wave functions between the Bloch states in Fe and the evanescent states in MgO for the $k_{\parallel} = 0$ direction. (b) Tunnelling DOS of majority-spin states for k = 0 in Fe(001)/MgO(001)(8 ML)/Fe(001) with parallel magnetic state[30].

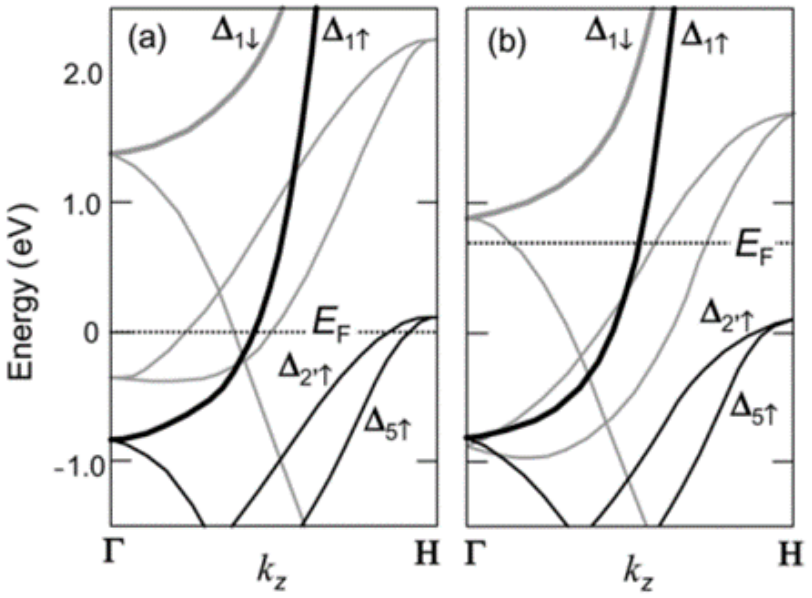

Figure 1.14: (a) Band dispersion of bcc Fe in the [001] (*Γ*-*H*) direction. (b) Band dispersion of bcc Co in the [001] (*Γ*-*H*) direction. (Redrawn from Bagayako *et al*. [39]) Thin black and grey lines respectively represent majority-spin and minority-spin bands. Thick black and grey lines respectively represent majority-spin and minority-spin 1 bands. EF denotes Fermi energy.

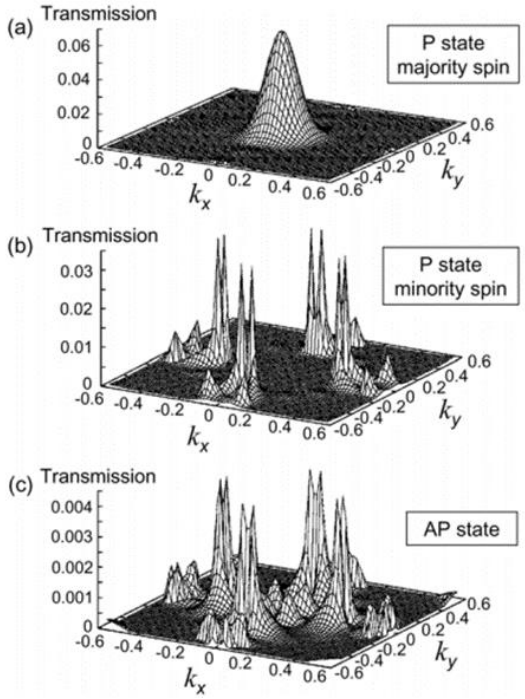

Figure 1.15: (a) Tunnelling probability in a Fe(001)/MgO(001)(4 ML)/Fe(001) MTJ as a function of k_x and k_y wave vectors. (a) Majority-spin conductance in the parallel magnetic state (P state), (b) minority-spin conductance in the P state, (c) conductance in the antiparallel magnetic state (AP state).

CoFeB as a Promising Ferromagnet

In 2004, Parkin *et al.* reported a TMR ratio of 220% at room temperature in CoFe/MgO/CoFe MTJ deposited by sputtering [40]. The MTJ structure was oriented (001) in the direction perpendicular to the film surface and epitaxial along the direction perpendicular to the film surface. In 2005, Djayaprawira et al. reported a TMR ratio of 230% at room temperature in CoFeB/MgO/CoFeB MTJ structures whereby CoFeB is an amorphous material for the ferromagnetic material [41]. They reported (001) oriented MgO film was grown on the sputtered amorphous CoFeB film by the sputtering method and the upper CoFeB film was also formed in an amorphous structure. In order to obtain a high TMR ratio, it is necessary that the ferromagnetic layer, which has interface with barrier, is also crystallized. It is important that MgO must be (001) orientation during film formation. If the MgO barrier layer is not in (001) orientation, CoFeB will not have a structure even after heat treatment is performed since MgO is model for CoFeB crystallization as seen in Figure 1.16.

Furthermore, in 2008, Ikeda and colleagues optimized the fabrication conditions of CoFeB/MgO/CoFeB MTJ structure to achieve TMR near the theoretical limit of 604% at room temperature and 1144% at low temperature [42]. The CoFeB/MgO/CoFeB MTJ, also is considered to have many practical advantages since deposited films from the buffer layer to the top ferromagnetic electrode layer are all by sputtering. The ability to form a film by sputtering method means that it is possible to cope with a substrate with a large area with good reproducibility and mass production. When considering the device application of MTJ, the characteristic that this mass production is possibly becomes an important advantage. Secondly, MgO spontaneously grows to (001) oriented film between amorphous CoFeB. Unlike Fe (001)/MgO (001)/ Fe (001) MTJ, which requires epitaxial growth from the substrate, there are wide choices in the buffer layer etc., It is possible to select structures for improvement of various characteristics.

Furthermore, since it has an amorphous structure, it is also advantageous which can be formed on inexpensive silicon on insulator (SOI) substrate. Therefore, CoFeB/MgO/ CoFeB MTJ was chosen as the base structure in this study.

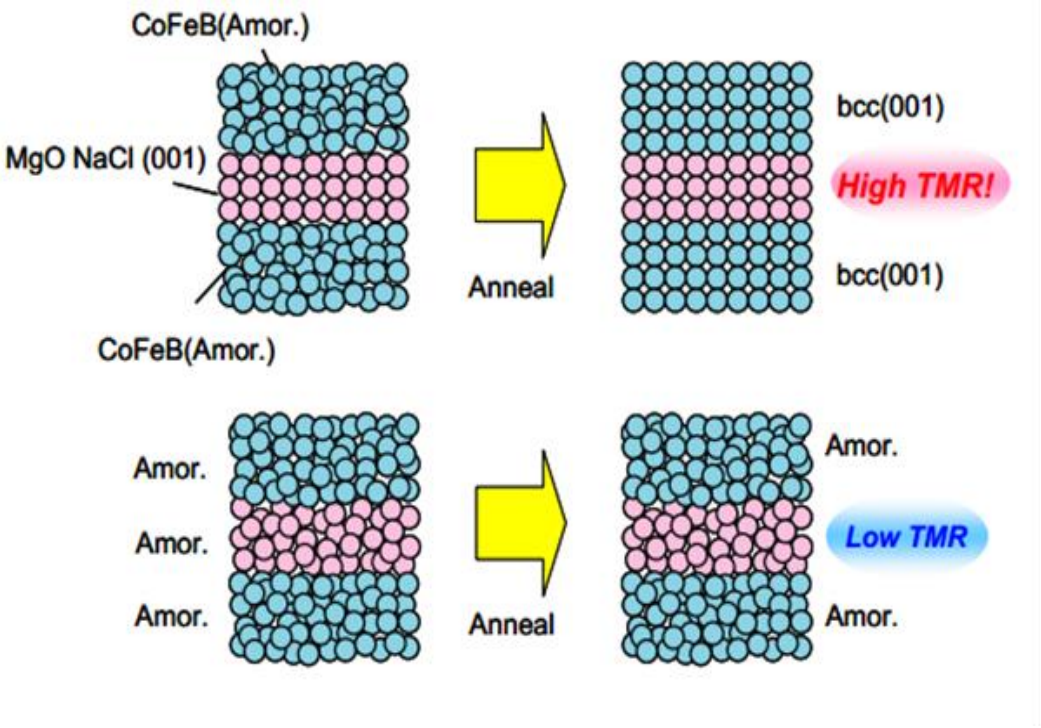

Figure 1.16: Crystallization mechanism of CoFeB [43]

CoFeSiB/Ru/CoFeB MTJ Free Layer Structure

Although CoFeB/ MgO/CoFeB MTJ develops a high TMR ratio by crystallizing the CoFeB layer by heat treatment, the value of H_k increases with crystallization, resulting in a decrease in sensitivity and a maximum value of magnetic field sensitivity is about 8 %/Oe [44]. A high magnetic field sensitivity of 25.3 %/Oe has already been achieved with MTJ using NiFe/Ru/CoFeB free layer with soft magnetic NiFe alloy (Permalloy) and synthetic structure with Ru. However, sensitivity of 40 %/Oe has been reported with CoFeB/MgO/CoFeB MTJ and CoFeSiB electrode [45].

Discovered by P. Duwez and colleagues in 1960 [46], amorphous alloy is an artificial substance having a disordered atomic arrangement like glass. In 1974, T. Masumoto *et al.* and others reported for the first time that iron-based amorphous alloys

had excellent soft magnetic properties [47]. The elements constituting the amorphous magnetic material are those in which the atomic weight of the magnetic transition metal (Fe, Ni, Co) and the semimetal (B, Si, C, P) is about 8:2, or the proportion of the magnetic transition metal and metal (Zr, Nb, Hf, etc.) is known to be a ratio of approximately 9:1. Soft magnetic properties of amorphous magnetic materials are thought to be due to the disorder in the order of atomic size. Large instability such as grains and grain boundaries do not exist in the amorphous crystals, therefore impurities that cause ‘traps’ are small and additionally due to the symmetry of the crystal, crystal magnetic anisotropy is not exhibited.

Sensor sensitivity improvement requires reduction of H_k, so a soft magnetic material is required. Conventionally used NiFe alloy is an important parameter for soft magnetic characteristics, there is not strictly a composition in which the magneto crystalline anisotropy constant K_1 and the magnetostriction constant λs simultaneously satisfy "zero". By adopting the (111) -oriented fcc structure, NiFe also affects the CoFeB layer growing into a bcc structure in which MgO is oriented in (001) orientation as a template after heat treatment. As a result, compared to CoFeB/MgO/CoFeB MTJ, there was a problem that the temperature at which the TMR ratio decreases is low and resistance to heat treatment is not sufficient.

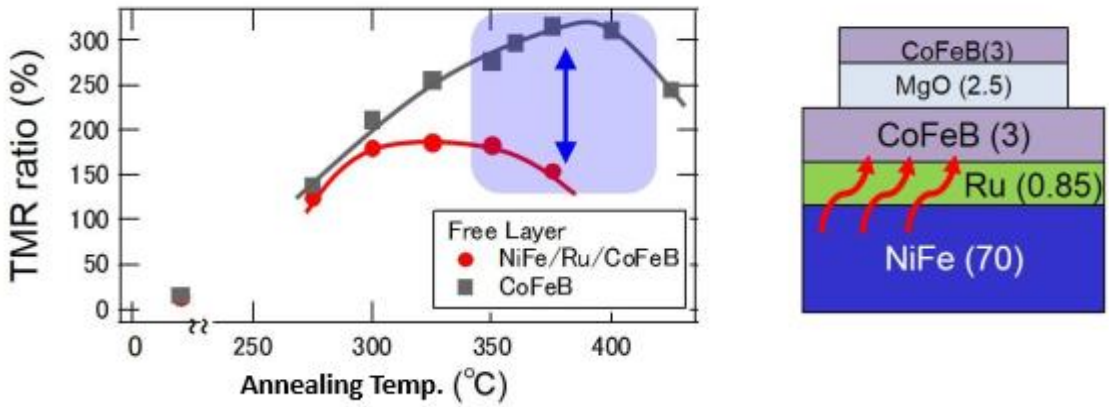

Figure 1.17: Free layer heat treatment temperature dependence of TMR ratio [48]

Since CoFeSiB has an amorphous structure, the crystal magnetic anisotropy constant K_1 is ideally zero. Also, when λ_s becomes zero the composition becomes $Co_{70.5}Fe_{4.5}Si_{15}B_{10}$. In other words, it is considered to be a material that is very excellent in soft magnetic properties. For CoFeB/MgO/CoFeB MTJ, it is necessary to perform heat treatment at about 300°C to 400°C in order to obtain a high TMR ratio. However, the amorphous alloy is crystallized by heat treatment at a high temperature and the soft magnetic characteristics deteriorates, so a high crystallization temperature is necessary, annealing stability was tested up to 450°C and crystallization was not observed [48]. As described above, since amorphous has no grains attributed to crystals, the surface roughness is also beneficial. In MTJ, which is a multilayer structure, there is the possibility of producing a high quality MgO insulating barrier layer due to low roughness. Therefore, high TMR ratio and low H_k could be reached and sensitivity of the MTJ sensor can be increased.

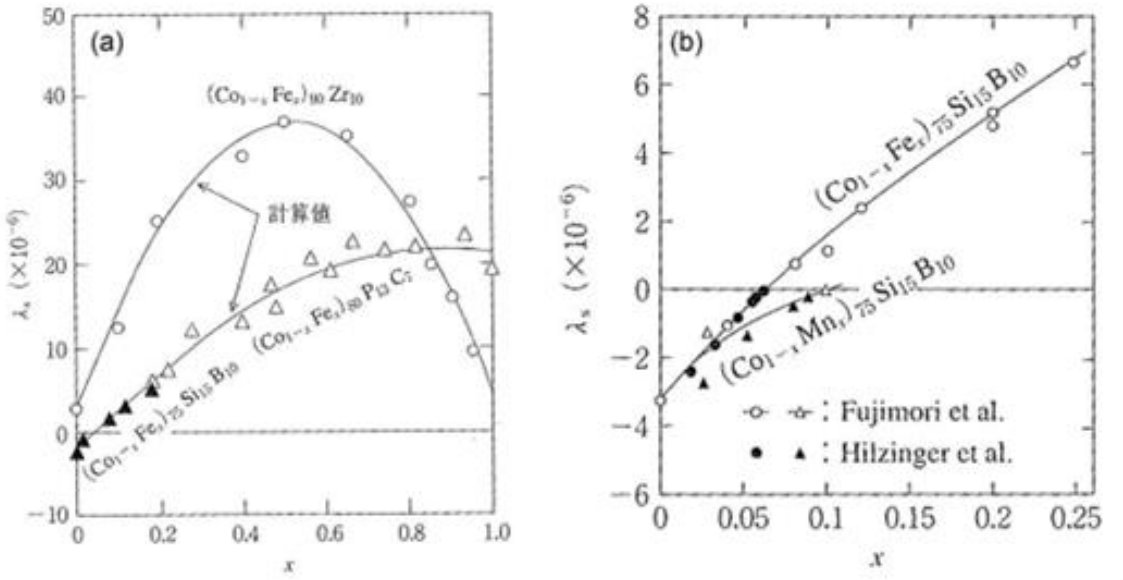

Figure 1.18: Atomic concentration ratio (dependence of x) of magnetostriction (λ_s) of the Co-Fe-Si-B amorphous alloy [48].

Although the CoFeSiB described in the previous section is soft magnetic, due to the amorphous structure, in the structure of CoFeSiB/MgO/CoFeB MTJ, is not well coherent and the TMR ratio decreases considerably compared with CoFeB/MgO/CoFeB MTJ. In a previous study, only a value of about 20% at the maximum was obtained [49].

Therefore, the sensor that is used in this research consists of a three-layer structure of CoFeSiB/Ru/CoFeB [45]. A thick CoFeSiB layer is used because it was shown that the sensitivity with increasing thickness as seen in Figure 1.19. Due to the RKKY interaction, the magnetization of the CoFeB layer is reversed following the magnetization reversal of the CoFeSiB layer, whereby H_k is greatly reduced. The Ru layer serves as a means of dividing the crystal structure of amorphous CoFeSiB and CoFeB that crystallizes to bcc. However, depending on the second annealing temperature, it may influence the overall sensitivity as shown in Figure 1.20. At T_{2nd} = 280℃ and 300 ℃, a linear resistance response against the external field was observed, in contrast to T_{2nd} = 320 ℃, the magnetoresistance curve shows that the resistance jumps around zero field. This behaviour indicates the rotation of the magnetic easy axis of the bottom free layer. Therefore, appropriate control of the second annealing temperature is needed to obtain both good linear response and high sensitivity.

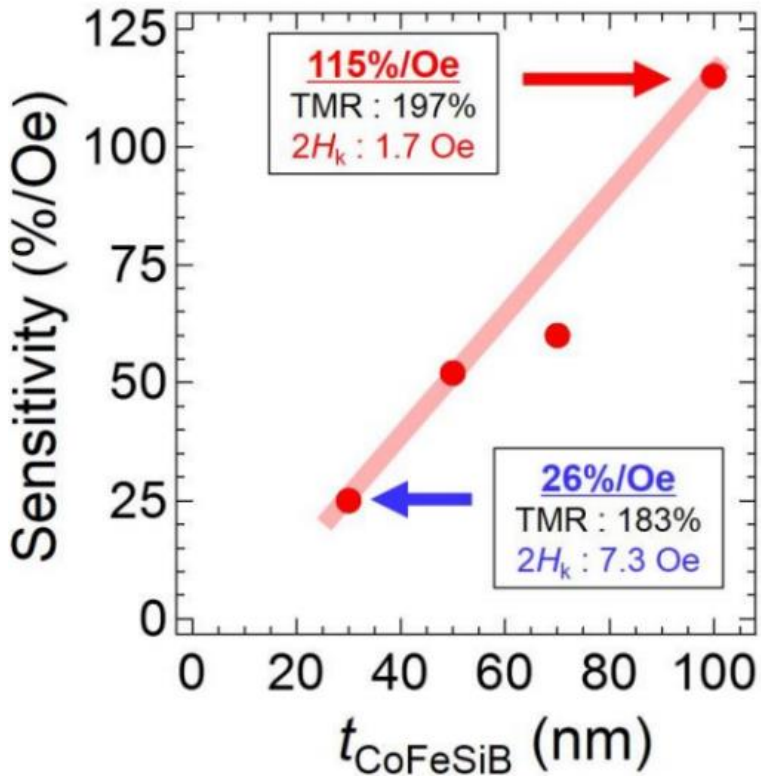

Figure 1.19: CoFeSiB thickness dependence on sensitivity

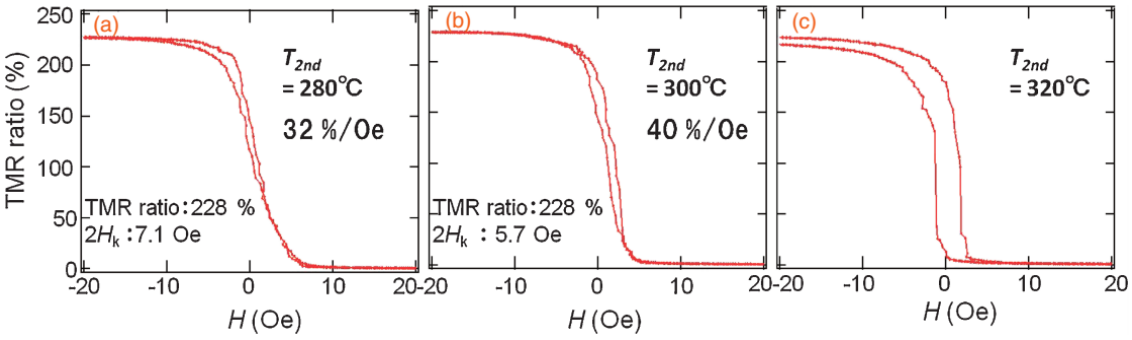

Figure 1.20: Magnified views of magnetoresistance curves in MTJs with middle thin Ru layer after second annealing process. (a) T_{2nd} ¼ 280 ℃, (b) T_{2nd} ¼ 300 ℃, and (c) T_{2nd} ¼ 320 ℃.

1.5.2 Sensor Sensitivity

The sensor sensitivity is defined as the derivative of the resistance with respect to the applied magnetic field. The MTJ sensor sensitivity S_{sensor} is expressed by slope of the linear region (assuming that it is linear), which can be normalized by the sensor minimum resistance (R_{min}) to compare the sensitivity of different sensors.

$$S_{\text{sensor}} = \frac{R_{\max} - R_{\min}}{\Delta H}\frac{1}{R_{\min}} = \frac{TMR}{\Delta H} \qquad \textbf{1.9}$$

Where $R_{\max}$ is the value of the sensor's maximum resistance (in anti-parallel state) and ΔH is the linear operating range of the sensor. From the equation, it can be understood that in order to increase or improve the sensors sensitivity, an increase in the TMR and a decrease in the saturation fields is required. However, the TMR ratio of a magnetic tunnel junction depends on the applied voltage until it starts to decrease almost linearly reaching a value which represents half of the maximum TMR ratio. The reason for the deterioration of the TMR value, is thought to be due to the presence of defects in the insulating barrier, which starts to conduct as the voltage acting on the sensor increases. Therefore, a high-quality barrier is required to improve the sensors properties.

1.6 Magnetic Tunnel Junction Linearization

Since the parallel and antiparallel states of magnetization are caused by the difference in coercive force between the respective magnetic layers, it is understood that the magnetoresistance curve is symmetrical about the zero magnetic field. Generally, in the spin-valve type MTJ [50], since the magnetic field is swept in the easy axis direction of the free layer and the measurement is performed at the same direction, then a magnetoresistance curve with hysteresis can be obtained. Such a MR curve can be used for applications in which the value of a magnetic field is read in two values, but it is not possible to measure a magnetic field as a continuous value. For the sensor to detect low magnetic fields, it requires a response that is linear and hysteresis free magnetic response, centred at zero applied field and without response discontinuities as shown in Figure 1.21.

Tondra *et al*. and Mazumdar *et al*. reported that a linear response to the magnetic field in the easy axis direction can be obtained by applying a bias magnetic field in the direction of the hard axis of the free layer and performing measurement along hard axis, as shown in Figure 1.22 [51][52]. Later study measured the bias magnetic field dependence of the sensitivity about 15%/mT. In order to obtain a linear magnetoresistance curve Negulescu *et al*. reported a structure in which both pinned layer and free layer has anti-ferromagnetic layer then optimization of two orthogonal annealing temperatures lead linear response [53].

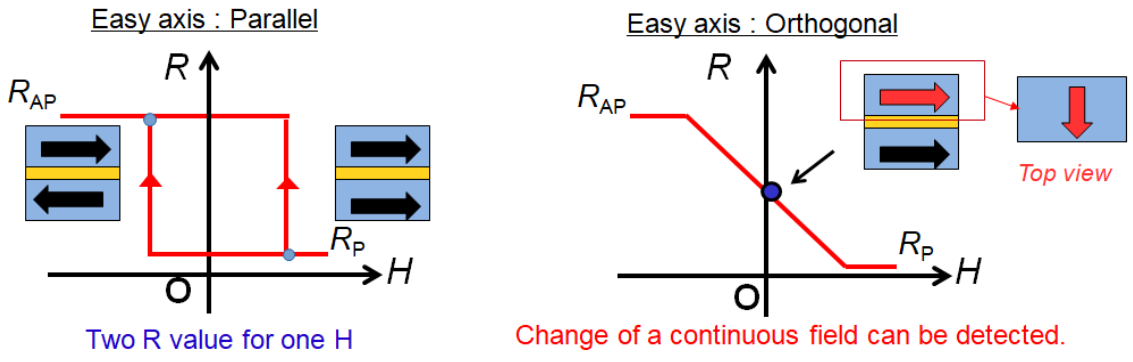

Figure 1.21: Hysteresis response MR curve and linear response MR curve

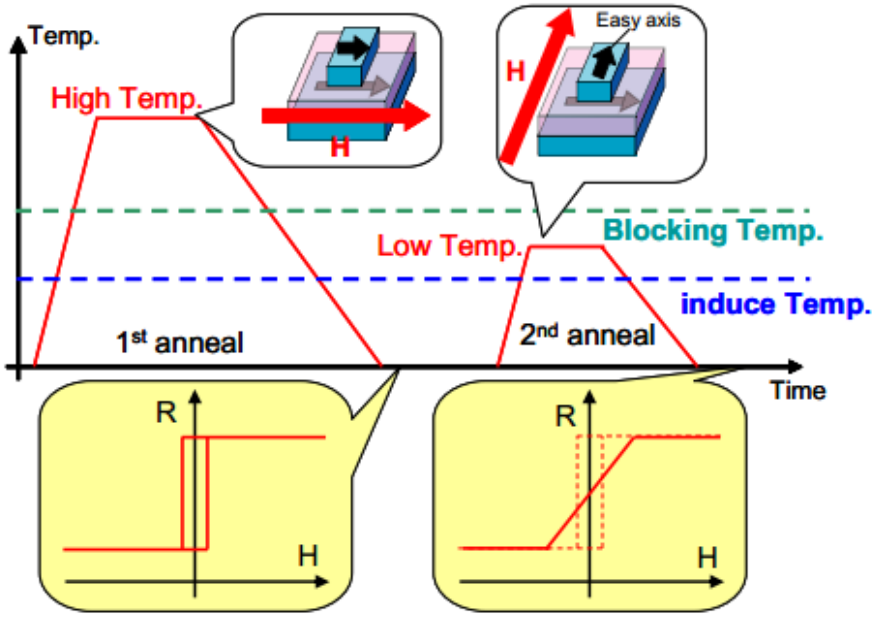

Figure 1.22: Schematic flow of annealing for linear response [48]

1.7 Magnetic Tunnel Junction Noise and Detectivity

1.7.1 Sources of Noise in MTJ

The noise that are present in an MTJ structure are spontaneous thermal and voltage fluctuations presented in every active or passive elements of an electric circuit, which disturbs the desired signal. Therefore, it is important that the noise affecting the sensors signal output must be low enough so that it would not interfere with the signal.

The main noise sources are the thermal and shot noise, 1/f electric and magnetic noise, and the random telegraph noise (RTN) [54].

Thermal Noise

Thermal electronic noise, also known as Johnson-Nyquist noise [55], is due to the random motions of charge carriers agitated by local temperature variations near Fermi level, even when no voltage bias is applied. Since the thermal motion of electrons provides the collision with impurities and electrons, therefore the thermal noise is

constant along the frequency spectrum and proportional to the conductor resistance and the device absolute temperature. The electromotive force due to the thermal agitation is theoretically described by the Nyquist formulation [56].

$$S_{v^2}^{thermal} = 4k_B TR \qquad \textbf{1.10}$$

where k_B is the Boltzmann constant, *T* is the absolute temperature and *R* is the resistance of the MTJ structures.

Shot Noise

Shot noise [57], is due to the electrons tunnelling across the insulating barrier. The thin insulator layer can be seen as a circuit discontinuity which leads to a current made of pulses exhibiting fluctuations in a short time scale [58]. This time-dependent fluctuation phenomenon is independent on the frequency and correlated to the thermal noise, and associated with the discreteness of electrical charge.

In an MTJ the total white noise (thermal + shot noise) can be expressed by:

$$S_{v^2}^{white} = 2eIR^2 \coth\left(\frac{eV}{2k_B T}\right) \qquad \textbf{1.11}$$

where *e* is the electron charge, *I* the sensor bias current, *V* the bias voltage across the MTJ, *R* the resistance, k_B the Boltzmann's constant and *T* the absolute temperature.

Random Telegraph Noise

The random telegraph noise (RTN) is the result of an abrupt magnetic domain activity around pinning sites in ferromagnetic materials [59]. There are two factors of the fluctuations, either from repeated capture of electrons into trapping centres [60] or from the motion of domain walls [61]. The sudden variations in the orientation during the sensing layer magnetization reversal process results in a non-coherent spin rotation.

The voltage spectrum of the random telegraph noise exhibits a frequency dependence, exhibiting a Lorentzian profile which is often shadowed at low frequencies by the 1/*f* magnetic noise [62]. However, an evidence of random telegraph noise can be

observed in a magnetic transport curve showing a step like profile during the sensing layer rotation.

Once the magnetic layers become crystallized due to annealing, the magnetic fluctuations will reduce thus RTN effect will become weaker [63].A lower noise level can also be achieved by applying a low bias voltage and selecting a large resistance area product ($R \times A$), since the random telegraph noise increases with the bias current [64].

1/f Noise

The low frequency voltage noise spectrum in a magnetoresistive sensor shows a behaviour inversely proportional to the frequency ($1/f$ noise) up to a specific knee frequency, beyond which the noise becomes frequency independent or white noise [65]. The $1/f$ noise results from the combination of an electric and magnetic component. The electric $1/f$ noise is associated with voltage fluctuations at the low frequency range caused by charge trapping in crystal defects which reduces the mobility of carriers [65], while the magnetic component is related with magnetic fluctuations associated with the magnetization alignment switching status at the interface between pinned layer and free layer [66]. The magnetic $1/f$ noise is absent only in the parallel and antiparallel state [67], due to the fact that the $1/f$ maximum noise power density lies between the saturation states which corresponds to the linear rotation of the free layer magnetization. The $1/f$ power spectral density is well described by Hooge's relation [68].

$$S_{v^2}^{1/f} = \alpha_H \frac{I^2 R^2}{Af} \qquad \textbf{1.12}$$

Where α_H is the phenomenological Hooge's constant, R the sensor resistance at the operating point, I the sensor bias current, f is the operating frequency and A the sensor area. As mentioned above, $1/f$ noise is frequency-dependent, and its voltage power spectrum increases with the sensor bias current. Once the $1/f$ noise has an electric and magnetic component, the phenomenological Hooge constant can also be decomposed in an electric and magnetic contribution.

$$\alpha_H = \alpha_{\text{electric}} + \alpha_{\text{magnetic}} \qquad \textbf{1.13}$$

α_{electric} is related with resistance-area product, the TMR ratio, the bias voltage, and the insulator barrier [69], whereas α_{magnetic} depends on the applied magnetic field, being minimized in the saturation states [70]. At the same time, the Hooge's constant can be used as an indicator to evaluate the sensor intrinsic noise at low frequency.

1.7.2 Detectivity

The detectivity of a sensor is the ability of the sensor to measure the magnetic field at a specific frequency with a determined bandwidth. In other words, any signal lower than the detectivity of the sensor will result in any output change. The detectivity formulation corresponds to the noise level expressed in magnetic field units

The total voltage noise in a single magnetic tunnel junction arises manly from the thermal noise, shot noise and 1/*f* electric and magnetic noise.

$$S_{v^2}^{\text{total}} = 2eIR^2 \coth\left(\frac{eV}{2k_{\text{B}}T}\right) + \alpha_{\text{H}}\frac{V^2}{Af} \qquad \textbf{1.14}$$

Taking account, the total noise power density, the detectivity of the sensor can be defined as:

$$D_{\text{sensor}} = \frac{1}{S_{\text{sensor}}}\left(\sqrt{\frac{2eR}{V}\coth\left(\frac{eV}{2k_{\text{B}}T}\right)} + \sqrt{\frac{\alpha_{\text{H}}}{Af}}\right) \qquad \textbf{1.15}$$

From the equation, it is understood that at low frequency, the 1/*f* noise is the main contributor. On the other hand, at higher frequencies both thermal noise and shot noise is more dominant.

1.7.3 Sensor Array

The range of applications using MTJ sensors has been limited by their noise level, by their voltage bias dependence and limited electrical robustness [71]. A strategy to overcome the robustness issue and to reduce the effect of the voltage bias dependence is by integrating MTJs in series. Compared to a single MTJ, a series integrated MTJs, as shown in Figure 1.23, can offer high sensitivity for detecting variations in magnetic field

due to accumulated effect [72], as shown in Table 1.1. By increasing the serial MTJ numbers, the overall sensor detectivity could be significantly improved. Overall, for detecting small field changes, integrating the MTJ elements into a series type structure is a viable approach in the development of MTJ sensors [73].

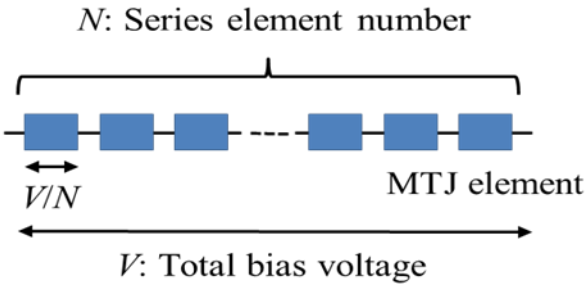

Figure 1.23: Model of serial MTJs. [74]

Table 1.1 Comparison of single MTJ and serial MTJs [74]

	Single MTJ	Serial-N MTJs
Signal amplitude (ΔV)	$\Delta V = IR$	$\Delta V = NIR$
Voltage noise (S_V^2)	$S_V^2 = 2eIR^2 \coth(\frac{eV}{2k_BT}) + \frac{\alpha V^2}{Af}$	$S_V^2 = N[2eIR^2 \coth(\frac{eV}{2Nk_BT}) + \frac{\alpha V^2}{N^2 Af}]$
Detectivity (D)	$D = \frac{1}{TMR \times \Delta H}(\sqrt{\frac{2eR}{V}\coth(\frac{eV}{2k_BT})} + \sqrt{\frac{\alpha}{Af}})$	$D = \frac{1}{TMR \times \Delta H\sqrt{N}}(\sqrt{\frac{2eR}{V}\coth(\frac{eV}{2k_BT})} + \sqrt{\frac{\alpha}{Af}})$

1.8 Gradiometric Sensors

A gradiometer measures the gradient (numerical rate of change) of a physical quantity, such as a magnetic field or gravity. There are several types of gradiometers mainly the axial gradiometer and planar gradiometer. The axial gradiometer consists of two sensors placed one above the other (z – axis). The result coming from the device is the difference in magnetic flux at that point in space, in other words, the result is the difference between what each of the sensors detects. It is most commonly used as a method to reduce any noise affecting the reference sensor or the main sensor. The main sensor is used to detect the target magnetic field (bio-magnetic, geomagnetic), this includes any noise affecting it. On the other hand, the second sensor or gradiometer sensor is used to only detect the noise. By taking the difference between these two sensor signals, ideally only the target signal will be left, resulting in a noise-free magnetic signal. This type of gradiometer is used often with SQUID based sensing system, as shown in Figure 1.24 [75][76].

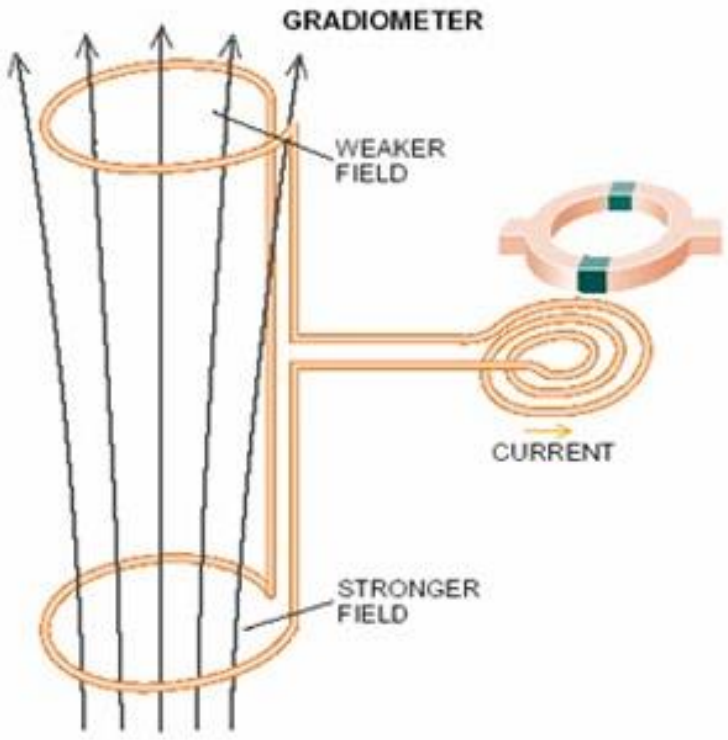

Figure 1.24: SQUID based axial gradiometer [77]

The planar gradiometer consists of two sensors placed next to each other (x -axis). The result coming from the device is the difference in flux between the two sensors. This type of configuration also has the potential to reduce any noise since both sensors will essentially take in the same noise intensity, as shown in Figure 1.25. However, the target signal will also be affected. Since there is a distance between the sensors, the sensors signal will also be shifted according to the distance, therefore the final signal will have different shape and intensity. Finding the right distance or baseline, is important to find the right balance to ensure the system is able to reduce noise and increase the signal without causing any deterioration.

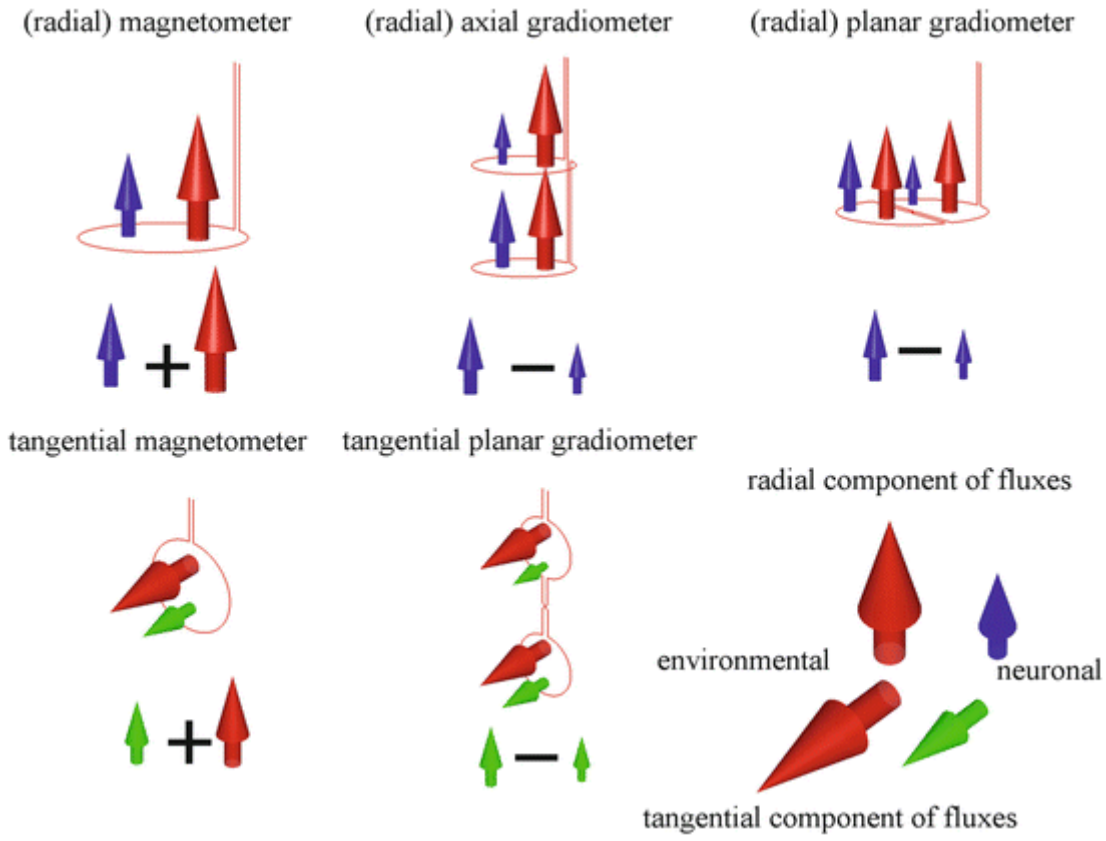

Figure 1.25: Different configurations for each respective gradiometer type [78].

1.9 Preceding Research on MFL

One of the preceding research that is used as reference is conducted by M.Hirose *et al.*, where they studied the various factors concerning the MFL testing [9]. As seen in Figure 1.26, in their research, they used a MFL testing measurement setup consisting of a permanent magnet and a magnetic sensor from the Shikoku Research Institute Inc., measuring various steel rebar with different measurement conditions. However, the factor that we will mainly be focusing on is the lift-off factor. Based on their results, the higher the lift-off, the smaller the change in the magnetic flux as seen in Figure 1.27. Using this information, we are able to expect really low magnetic flux intensity as we go to high lift-off range, thus the need for a high sensitivity sensor. Since this research maximum lift-off is 16 cm, we aim for measurements at higher than 16 cm. The research also established a method for measuring steel rebars that are in a structurally bent, which can be used for future references.

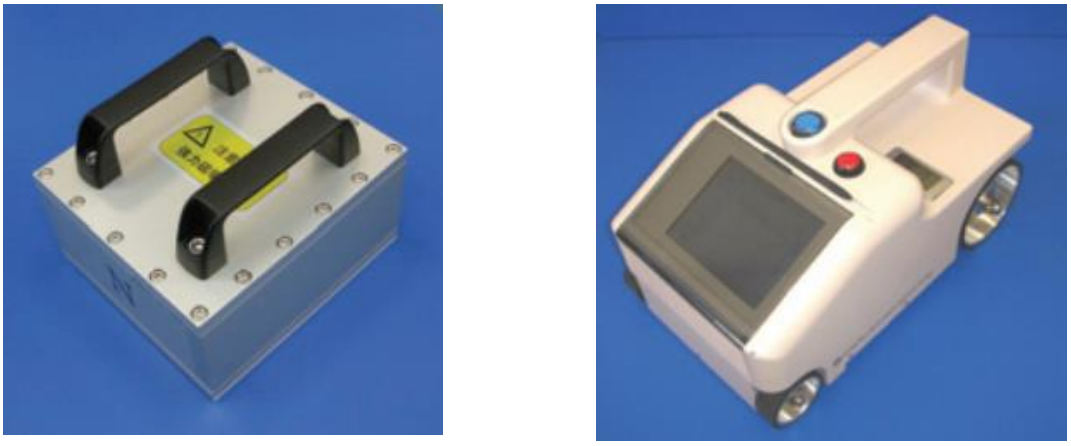

Figure 1.26: The permanent magnet with a strength of 7.0 mT (left) and the magnetic sensor used (right)

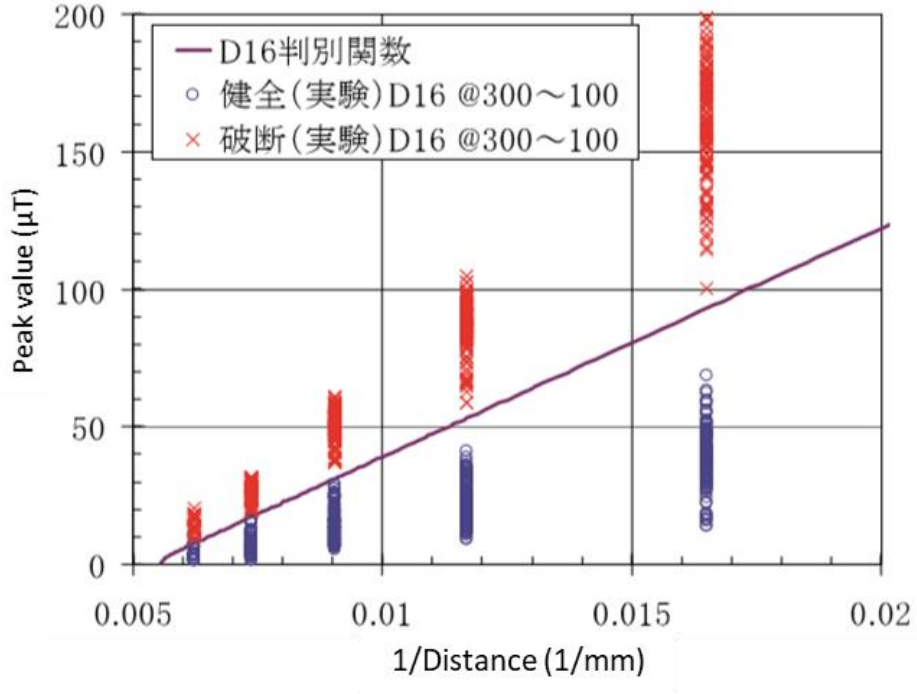

Figure 1.27: Results shown for different lift-offs. The linear line shows Mahalanobis' Distance calculation where if the point is below the linear section, it is clear of defects, while if the point is above is contains fractures

Another research is done by Wu Dehui *et al.*, from the Department of Electromechanical Engineering, Xiamen University, where they designed a non-destructive method by measuring the change rate of magnetic flux leakage [79]. The way they designed the measurement system is by placing two Hall sensors next to each other, essentially in the form of a planar gradiometer. The Hall sensors will measure the magnetic flux are placed inside a U-type magnetic yoke, then moved along the target specimen, as shown in Figure 1.28.

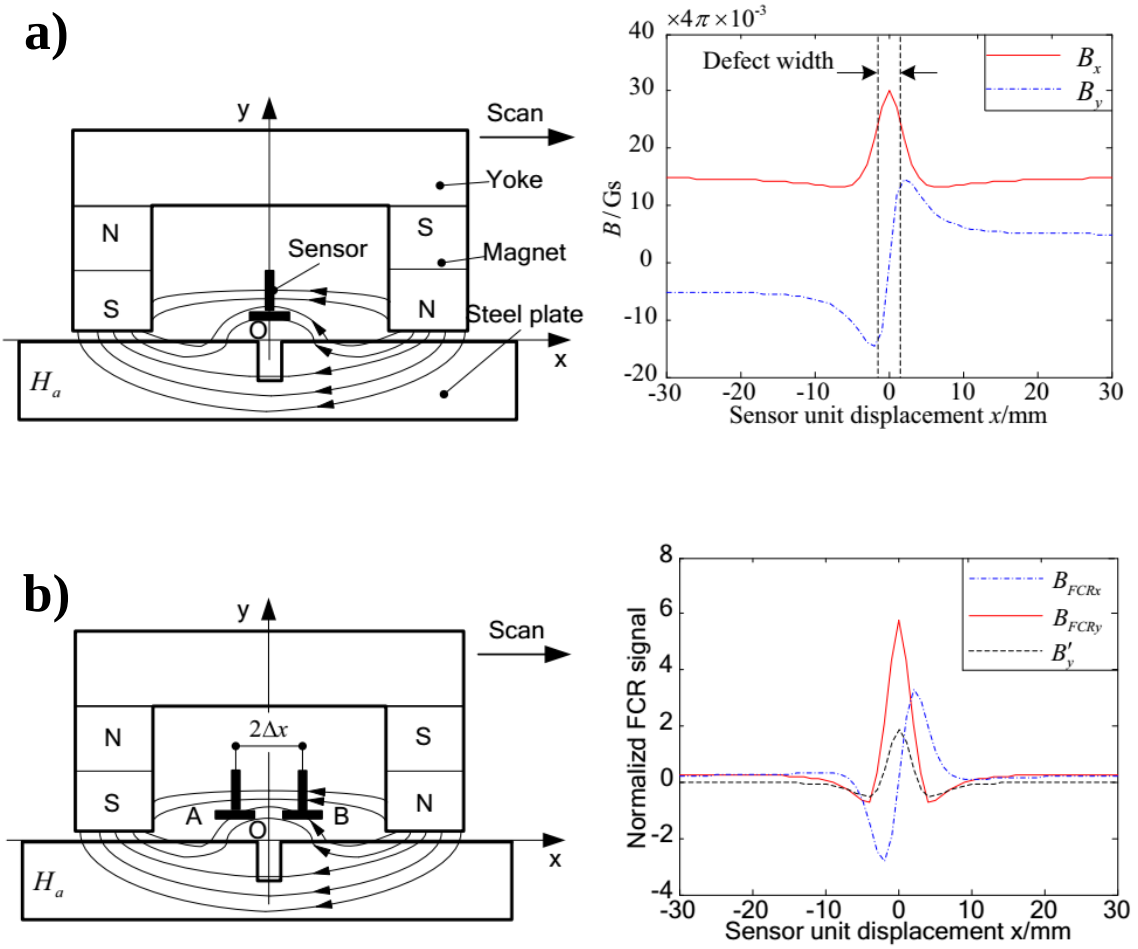

Figure 1.28: a) The left diagram shows the traditional MFL method using a single sensor setup with its respective output on the right. b) The left diagram shows the proposed flux change rate method with its respective output on the right

In the traditional method, shown in Figure1.28 (a), the B_y signal (or in my case the signal of the *z*-axis), consists of peak-and-trough signal with the defect location being the middle point between them. On the contrary, the designed system in Figure 1.28 (b) changes the signal to a large single peak.

$$B_{FCRy}(0) = B_y(0+\Delta x) - B_y(0-\Delta x) = 2B_y(\Delta x)$$
$$= 2\ln\frac{[(\Delta x + w)^2 + y^2]}{[(\Delta x - w)^2 + y^2]}. \qquad \textbf{1.16}$$

According to equation 1.15, when the sensors are placed within a distance of $2\Delta x$ between each other, the resulting signal will be twice as large. This is because the trough and peak signal from sensor A and sensor B respectively, overlap each other causing the signal increase and change into a single peak signal.

$$N_{b\_FCR}(x, y) = N_b(x + \Delta x, y) - N_b(x - \Delta x, y) \approx 0 \quad \textbf{1.17}$$

The group also theorized that the resulting noise that affects the sensor could be reduced to around 0 based on equation 1.16. This is in line with the description of the planar gradiometer mentioned in the previous section.

1.10 Research Motivation

This aim of this research is for the development of a MTJ based system for the MFL testing of reinforced concrete. Some real structures such as buildings, bridges, and trail racks use reinforced concrete as a support, with some of the steel rebar located deep within the concrete. Therefore, this research set the lift-off value of ≥ 200 mm as the target to determine the real field application of MTJ based NDT system. However, in reality, at measurement at high lift-off results in the leaked signal to be small and weak. Moreover, the measurements are done in an unstable environment with various sources of magnetic noise (environmental, machinery), causing the signal to be even more difficult to detect. Therefore, I propose a planar gradiometer measurement setup using highly sensitive magnetic tunnel junction (MTJ) sensors. The MTJ sensors have been proven to have excellent sensitivity in the nT range, thus it is the perfect candidate for application in non-destructive testing. Table 1.2 shows MTJ sensors [80] performance compared to other commercially available magnetic sensors, such as Hall sensors [81], AMR sensors [82], GMR sensors [83], MI sensors [84], and SQUID [85]. Compared to other sensors, MTJs are only outmatched by the SQUID in terms of detectivity, however, since the SQUID needs to operate at low temperatures, which comes with added cost, it is not as cost efficient as the rest of the sensors. To solve the problem of the magnetic noise affecting the sensors, two MTJ sensor modules are placed in a planar (x-axis) gradiometric setup with a specified distance between them ($2\Delta x$), the system is able to

reduce the overall magnetic noise since both modules will be affected by the same noise. This is based on the reports by the groups mentioned in the previous section, however, there is not enough evidence regarding planar gradiometers as a whole, especially using MTJ sensors. Therefore, I believe this setup will assist in detecting defects at large lift-offs values, through excellent sensor sensitivity and noise reduction.

Table 1.2 Comparison of MTJ sensors with other magnetic sensors

Sensor	Running Cost	Detectivity	Operation Temp.
Hall Sensor	○	10^{-6} T	Room Temp.
AMR	○	10^{-4} T	Room Temp.
GMR	○	10^{-6} T	Room Temp.
MI	△	10^{-12} T	Room Temp.
SQUID	×	10^{-16} T	Low Temp.
MTJ	○	10^{-13} T	Room Temp.

Based on my own experience measuring a reinforced concrete specimen in the outside environment, the main issue was the magnetic noise. Up until that point, I was able to measure a 1 cm gap in the same specimen inside the experiment room. With this in mind, I proceeded to measuring in the outside environment to determine the applicability of the MTJ sensor system. However, the environmental noise was too large that it overwhelmed the sensor, immediately saturating the sensor signal to its respective maximum and minimum dynamic range (±4 V), as shown in Figure 1.29. It made the detection of the gap impossible, since its signal was covered by the environmental noise, therefore using the gradiometer setup, it might be possible to negate or reduce its effect.

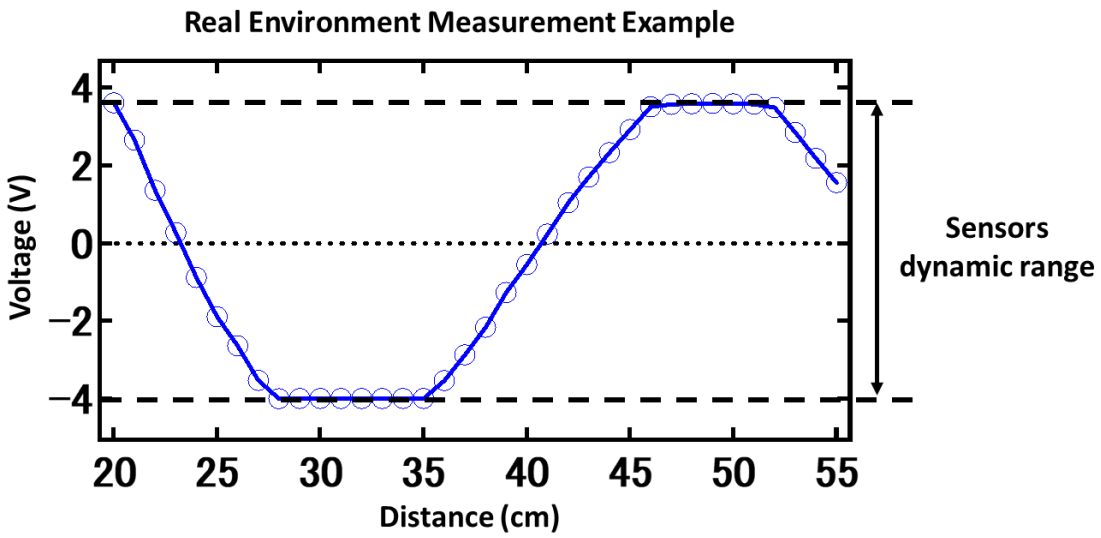

Figure 1.29: Real environment measurement data. Due to the environmental noise, the sensor signal is saturated at its dynamic range value.

Another motivation of this research is to find hopefully find a new pathway in for the application for spintronic sensors. Table 1.3 shows the historical development of spintronic phenomena followed by the devices that has come through based on it. However, for the best of 50 years, most of the applications are MRAM-based, followed by application for bio-magnetic field detection. Recently, it has been found that MTJ sensors are able to detect a weak, sub-pT, magnetic field at a low frequency, demonstrating real-time measurement of magnetocardiography (MCG) and nuclear magnetic resonance (NMR) of protons using developed sensors [80]. The recent MTJ sensors have proven their excellent properties, therefore it should have more opportunities to be applied in various fields. With that in mind, I believe that through the results of this research using the designed MTJ based gradiometric setup, the pathway for MTJ sensor application in the field of non-destructive testing is open and could be realized in the near future.

Table 1.3: Historical development of spintronic phenomena and devices [86]

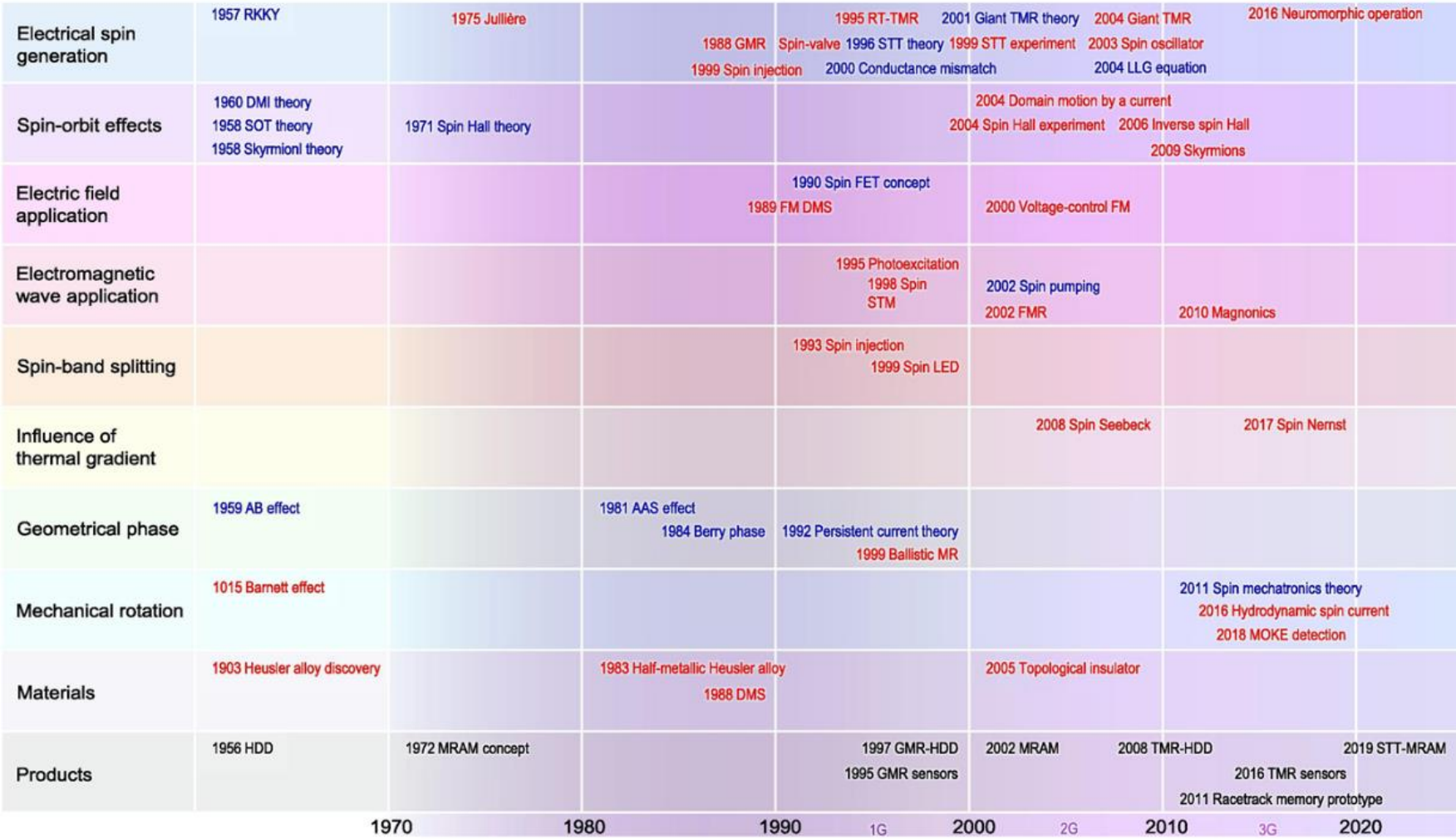

1.11 Research Objective

Based on the introduced preceding research on MFL, in addition to the motivation of my research that I have stated above, the objective of this research is for the development of a MTJ based gradiometric sensor for the MFL testing capable of detecting defects (for this research in the form of a gap) at high lift-off of ≥ 200 mm.

In order to achieve this objective, the following investigations were carried out

1) Investigating the noise reduction properties of the MTJ based gradiometric system
2) Optimizing or determine the suitable baseline ($2\,\Delta x$) value for the gradiometric system for this research
3) Measurement of steel bar sample at with various gap widths and at various lift-off values.

Chapter 2: Magnetic Flux Leakage Testing Setup

2.1 Measurement Setup

2.1.1 Measured Specimen (Steel Bar)

In this research, the measured specimens consist of 2 steel bars of the same type with a diameter of 20 mm and length of 500 mm, as shown in Figure 2.1. For the gap (defect measured), the steel bars were connected end to end, this way the gap size could be freely changed. The measured gap sizes varied from 1 mm to 10 mm.

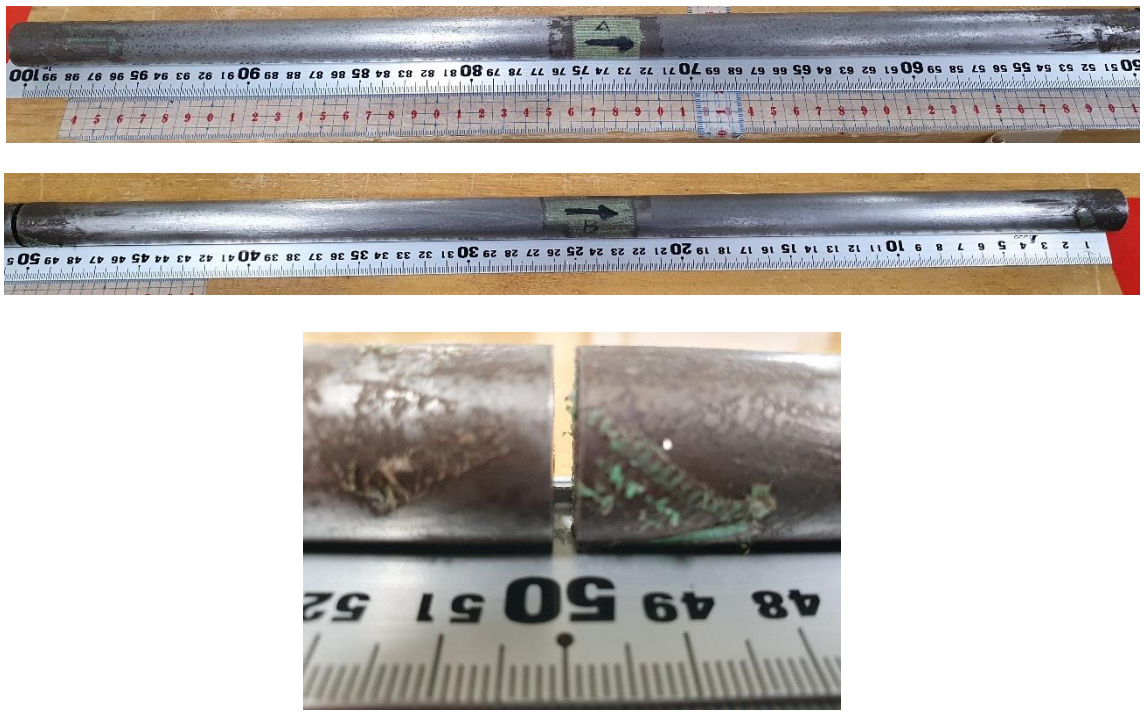

Figure 2.1: The 2 steel bars used (top and middle). The gap (bottom) is adjustable by changing the distance between steel bars

Even though the steel bar type and size used for this research is different to in the actual concrete specimen (railway sleepers), by scaling the size down, it is easier to conduct the measurements. In reality, the concrete sleeper weighs around 300 kg, therefore it would be difficult to maneuver it around, and since the steel bars are placed inside the concrete, it would be difficult to change the size of the gap. Nevertheless, in

the future, I would again conduct the experiments on a real specimen, to further proof the capability of the fabricated measurement system.

2.1.2 Measurement Technique

The technique used throughout the experiments is based on MFL testing method, where the reinforced concrete is first magnetized to induce magnetization in the steel rebars. In this research, the steel bars are passed through a solenoid, consisting of an 875-turn coil, with a 2.0 A bias current, resulting in a 2.3 mT magnetic field.

The steel bars were magnetized only once before every measurement, and its magnetic field were measured with a Gauss meter to verify its strength. I observed that the value was unchanged. This may be due to the remanence of the steel bar. The MTJ sensors will then be passed along the concrete according to the measurement setups.

2.1.3 Equipment

To be able to convert the magnetic flux density into a quantifiable quantity, the MTJ sensors resistance will change according to the magnetic flux which will cause the voltage to fluctuate. From the fluctuations, the fractures presence and location will be detectable. Shown in Figure 2.2, in this research I used an ADVANTEST R6142 Programmable DC Voltage/Current Generator to supply bias current to the MTJ sensor, an TEXIO Regulated DC Power Supply for +/- voltage of the amplifier circuit and the output will be observed and recorded through a personal computer. The sensor modules are attached to motor unit, controlled by a LEGO EV3 Brick, as shown in Figure 2.3. The motors moving speed and distance were programmed via the Visual Basic coding language to move the length of the steel bar specimen at a speed of 50 mm/sec. Using a CONTEC USB I/O Terminal, seen in Figure 2.3, the raw analog sensor output could be seen in real time digitally on the computer. From there, the raw data would be further processed, and the final data could be viewed in graph form.

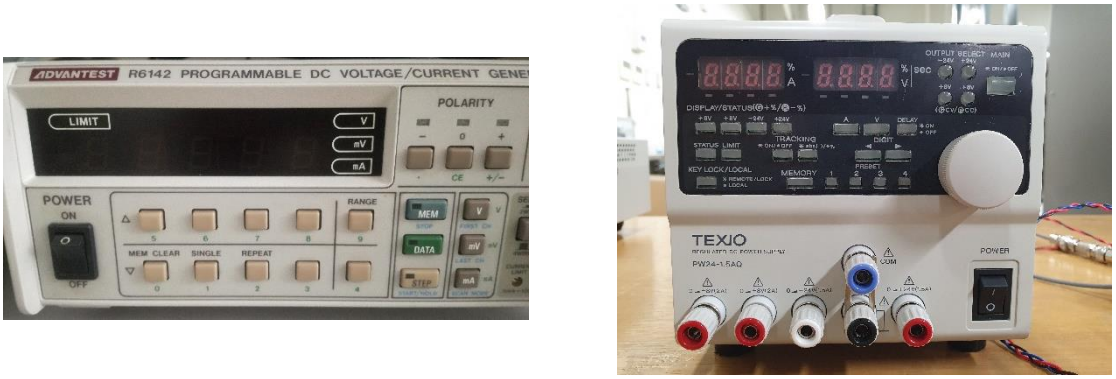

Figure 2.2: The current generator (right) and voltage generator (left) used

Figure 2.3: The USB I/O Terminal (right) and LEGO EV3 Brick for the motors (left)

2.2 MTJ Sensor Setup

2.2.1 Wheatstone bridge

A Wheatstone bridge is an electrical circuit first described by Samuel Hunter Christie (1784-1865) in 1833, being however popularized by Sir Charles Wheatstone, who invented many uses for this circuit once he found the description in 1843. It is commonly used in electronic devices to measure an unknown electrical resistance. The

fundamental concept of the Wheatstone bridge is two voltage dividers, both fed by the same input, where the circuit output is taken from both voltage divider outputs, as shown in Figure 2.4, and is given by the following expression:

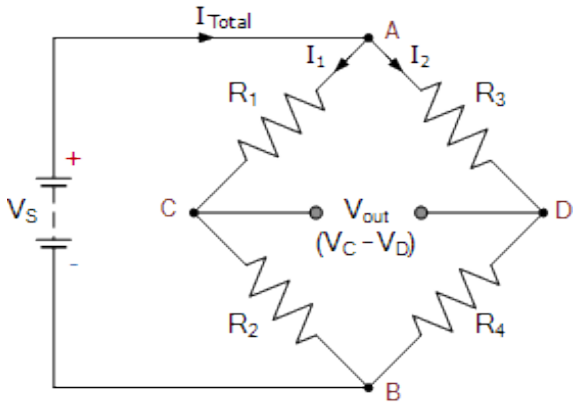

Figure 2.4: The Wheatstone bridge

$$V_{\text{out}} = \left(\frac{R_3}{R_1 + R_3} - \frac{R_4}{R_2 + R_4}\right) I_{\text{total}} \qquad \textbf{2.1}$$

In its classic form, a galvanometer (a very sensitive DC current meter) is connected between the output terminals and is used to monitor the current flowing from one voltage divider to the other. If the two voltage dividers have the same ratio $R_1/R_2 = R_3/R_4$, then the whole circuit is balanced, resulting in $V_{out} = 0$. If one of the resistors changes even a little bit in value, the bridge will become unbalanced and current will flow through the galvanometer.

Even though a unique resistance can be used as sensing element, a Wheatstone bridge setup is always a good recommendation as the starting step in the design of resistive sensors, since it provides a differential output as a function of the resistance variation. In fact, using MTJs as resist elements in a Wheatstone bridge allows to have a linear magnetic field sensor with an offset-free signal. [87]

In this research, I focused on one MTJ sensor if a full Wheatstone bridge setup in each sensor module. As seen in Figure 2.5, the bridge circuit consists of an MTJ sensor connected in series with a resistor (R_2) that is close to the sensor's resistance (750 Ω for MTJ 1 and 720 Ω for MTJ 2) in one arm of the bridge, while in the other arm, similar

resistors (R_1 and R_3) are connected in series. Ideally, the initial value of the bridge setup would be 0 V, however since the resistance of the MTJ sensors fluctuate according to the surrounding magnetic field, I could only get a value that is close to 0 V.

The voltage from the bridge circuit (from point C and D) will then be passed through an instrumentation amplifier, where the signal will be amplified by 1 time. The amplifier circuit will act as a buffer amp, and as a method to reject common mode noise. Since there are two voltage source points (C and D), there may exists 'noise' in the voltage signal. As seen in Figure 2.5 (above the instrumentation amplifier), the normal voltage signals from A and B will be in different phases, when these pass through the amplifier, the signal will be subtracted accordingly. On the contrary, the noise will be in the same phase in both A and B, when it is passed through the amplifier, it will be rejected producing a noise-less signal.

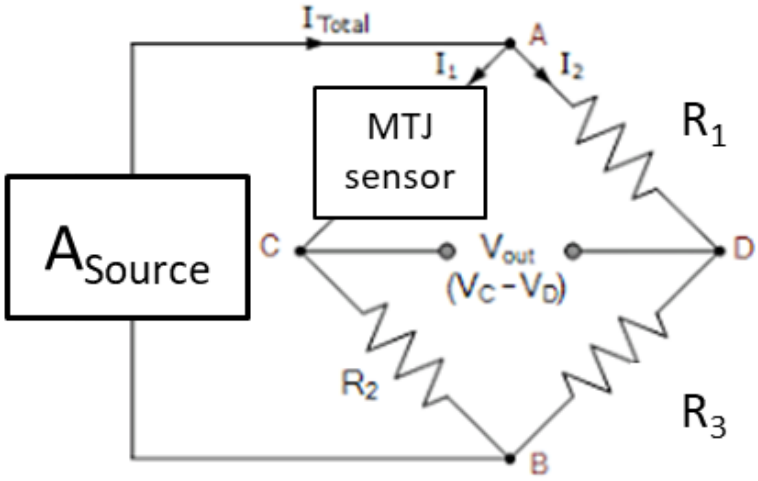

Figure 2.5: MTJ sensor module used in the measurement setup

2.2.2 MTJ Sensor Characterization

MTJ sensors have researched for their applications in various fields from memory storage to biomedical due to their high sensitivity range. Therefore, it is possible that MTJ sensors could perform as well in the low magnetic field environment of MFL testing at high lift-off. However, before measurements can conducted in real field environment, it

is important that the sensors are first measured in a controlled environment to observe and understand their characteristics.

I measured each sensor module to evaluate the change in resistance according to an applied magnetic field. The sensor was designed and fabricated by Tohoku University's Spin Sensing Factory (SSF), as shown in Figure 2.6. Each MTJ sensors consists of 1764 MTJ structures in series configuration, with a sensing area of 7x7 mm^2. The measurements were conducted using a Helmholtz coil located inside a magnetic shield room. The sensor is placed inside the coil with the sensing direction parallel to the applied magnetic field. The sensor is connected to a current generator which supplies the bias current (1.0 mA) and the resistance change will be recorded automatically by a digital multimeter controlled from a computer.

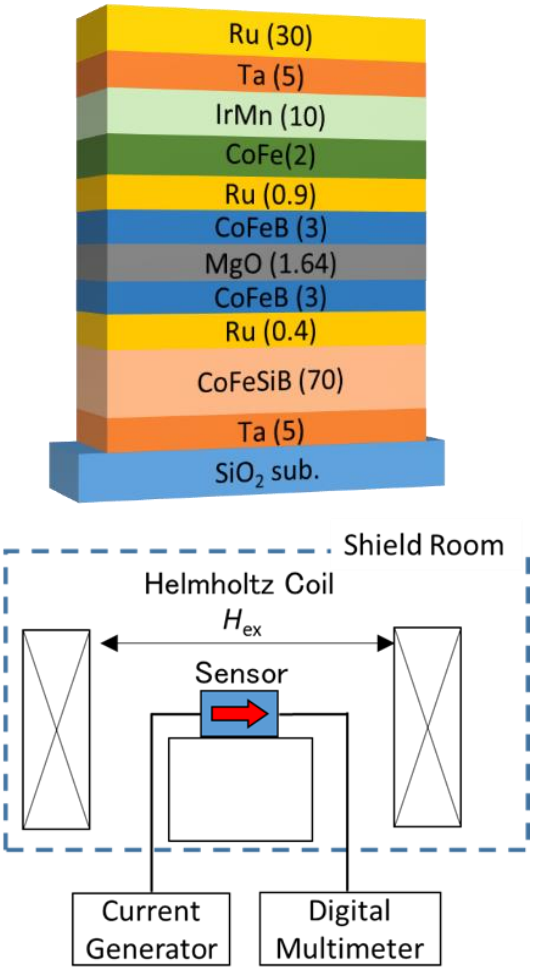

Figure 2.6: Top diagram shows the MTJ sensor structure used throughout the experiments. Bottom diagram shows the measurement setup for the sensor characterization. Note that the sensing direction is parallel to the applied magnetics field's direction

From the results, the MTJ sensor had a normal reaction towards the applied magnetic field. Normal in the sense that according to the direction and strength of the magnetic field, the orientation of the free layer changes, resulting in the resistance change. The low resistance state shows when the magnetization orientation is in parallel direction, while the high resistance state shows for the anti-parallel orientation. The linear response is important for a MTJ to be applied as a sensor since it shows the different resistance according to the magnetic field [52].

Table 2.1: MTJ sensor sensitivity based on the linear section of the magnetic response graph

	Sensor 1	**Sensor 2**
Sensitivity	42.321 V/mT	39.734 V/mT

2. 3 Summary

Even though the steel bar type and size used for this research is different to in the actual concrete specimen (railway sleepers), by scaling the size down, it is easier to conduct the measurements. In reality, the concrete sleeper weighs around 300 kg, therefore it would be difficult to maneuver it around, and since the steel bars are placed inside the concrete, it would be difficult to change the size of the gap. Nevertheless, in the future, we would again conduct the experiments on a real specimen, to further proof the capability of the fabricated measurement system.

I measured each MTJ sensor module used in my research to evaluate the change in resistance according to an applied magnetic field. With this, I was able to determine their sensitivity. The first MTJ sensor module has a sensitivity of 42.321 V/mT and the second MTJ sensor modules' sensitivity is 39.734 V/mT. To be able to convert the magnetic flux density into a quantifiable quantity, the MTJ sensors resistance will change according to the magnetic flux which will cause the voltage to fluctuate. From the fluctuations, the fractures presence and location will be detectable. In this research I was able to directly observe the sensor signal by passing it through an AD converter and into

a PC where all the signal processing takes place. The overall block diagram of the circuit flow is shown in Figure 2.8, while the overall measurement setup is shown in Figure 2.9.

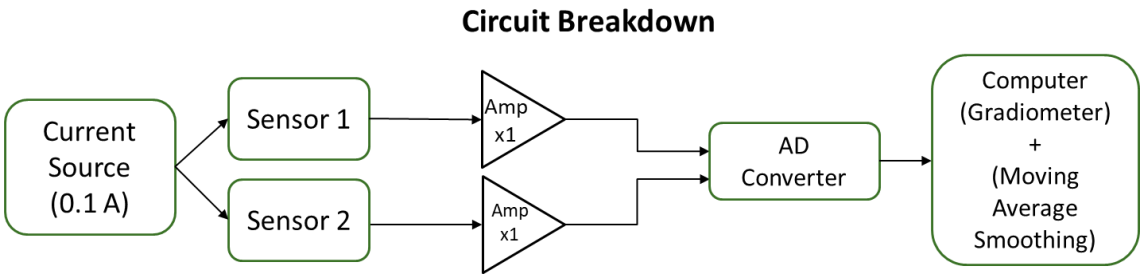

Figure 2.8: Block diagram of the components in the circuit

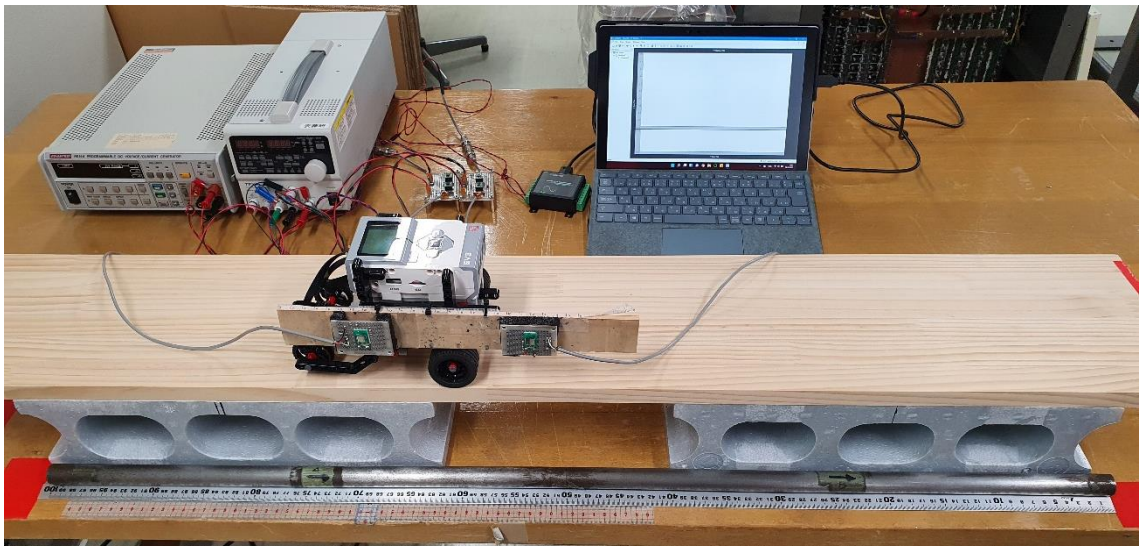

Figure 2.9: Measurement setup

Chapter 3: Noise reduction of MTJ based Gradiometric Sensors

3.1 Noise measurement

In real field application, the measurements would be conducted in the outside environment, exposing the sensors probe(s) to various noises or disturbances. The Earth's magnetic field and equipment noise may interrupt the sensors' ability to detect the leaked magnetic flux, especially if the defect signal is small. By using a gradiometric setup, the sensors are placed in the same plane (*x*-axis), which means the magnetic noise sources would affect them with the same intensity. After subtracting the sensors output, the total magnetic noise from the sensors should be close to zero.

In order to proof this concept, we conducted an experiment with the goal of investigating the noise reduction effect of the gradiometric setup compared to a single MTJ sensor. The experiment was conducted in a magnetic shield room, which helps to efficiently control the biased magnetic field on the sensor. By applying magnetic fields at different intensities and taking the sensors output, we are able to determine the base noise level for both single sensor setup and gradiometer setup.

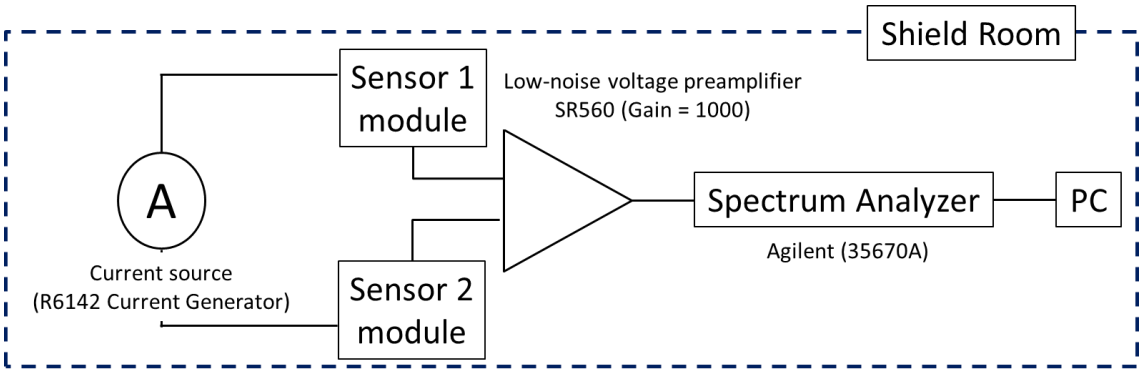

Figure 3.1: Diagram showing the noise measurement setup. The low-noise voltage preamplifier can measure each individual sensor output and able to take its difference (gradiometer function).

As seen in Figure 3.1, a current generator will supply a bias current of 0.1 A to each sensor. The sensors are placed in the middle of a Helmholtz coil, which will supply the bias magnetic field at a frequency of 10 Hz. The initial sensor signals will be passed through a low-noise voltage amplifier, with a gain of 1000, to maximize the output. The signal will then go through a spectrum analyzer, which will isolate the sensor signal at 10 Hz using FFT analysis, where the final signal value will be determined by the 10 Hz peak.

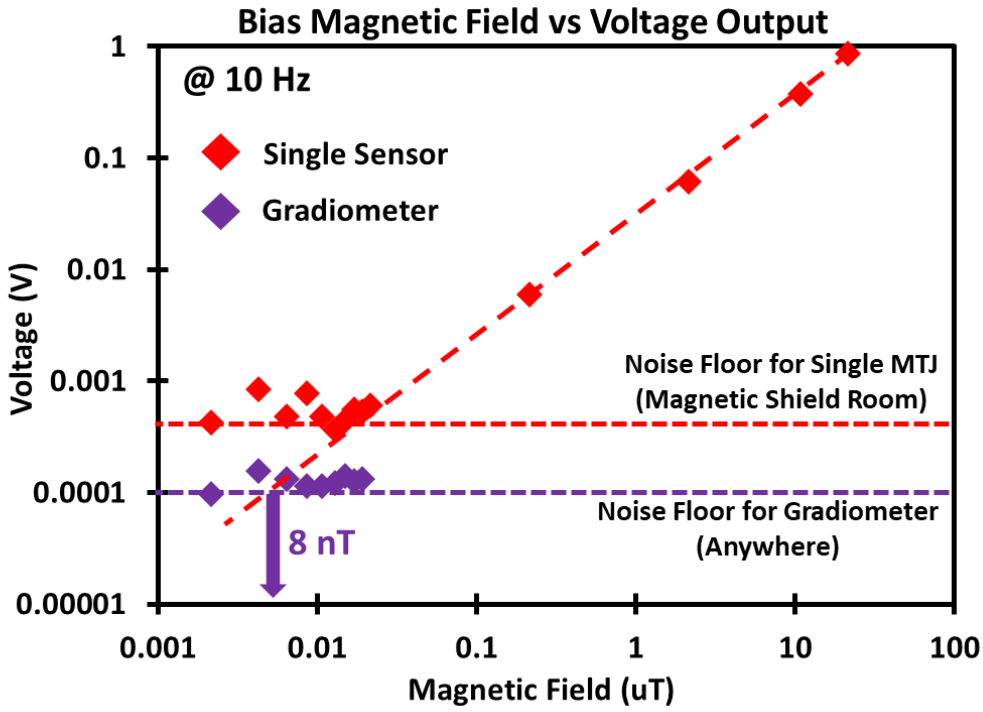

Figure 3.2: The voltage output of the sensor setups at various bias magnetic fields. The point where the output starts to saturate is the noise base level for every setup.

The results are shown in Figure 3.2, where it is seen that the noise level of each setup is different from each other. To find the overall detectivity of the gradiometric setup, similar steps were taken as for the single sensor, however, instead of using the linear part of the gradiometer graph, the single sensor graph was used. This is because, in our planar gradiometric setup, we are taking the change in the magnetic flux caused by the defect, therefore the sensor response towards the magnetic flux does not change, only its position as seen in Figure 3.3. However, since the sensors exist in the same plane, their response towards the noise should be the same and by taking the difference between their outputs,

the resulting signal resulted in a lower value than the single sensor. By combining the sensor sensitivity of the single sensor and noise base level of the gradiometric setup, the resulting detectivity was 8 nT.

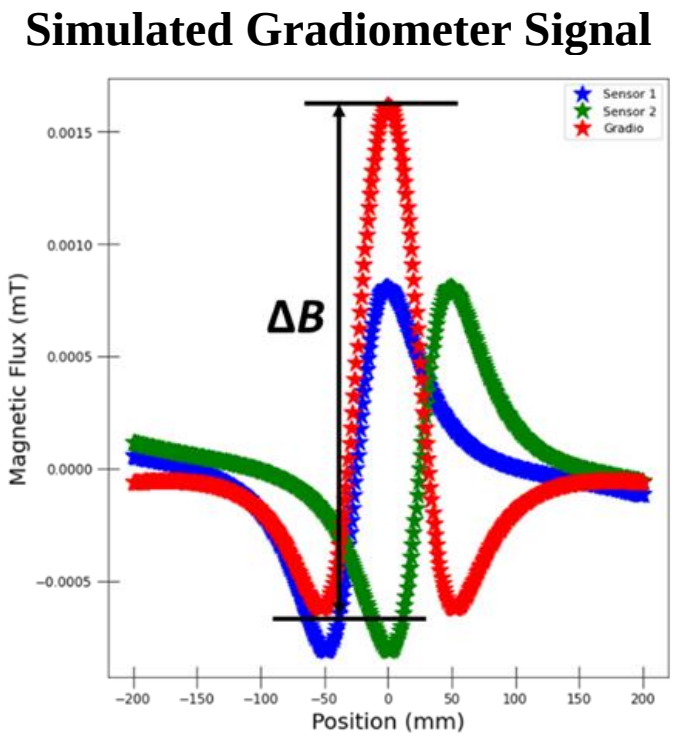

Figure 3.3: Simulated gradiometer signal. The sensors responses (blue and green) are similar and because they are placed at a distance apart from each other (baseline), which results in a shift in their response. By subtracting their outputs, the gradiometer signal (red) is obtained

3.2 Discussion

A point that needs to be clarified is why the resulting voltage for the gradiometer is not equal to 0 V. There are two factors, the first being the sensitivity in the Sensor 1 Module and the Sensor 2 Module are different. Ideally, their values should be the same, which would produce identical response and results in the final signal being 0 V. However, as mentioned in the previous chapter, there is a slight difference in their sensitivity value, resulting in a different output for each respective sensor module at each bias magnetic field. When their outputs are subtracted via the gradiometer method, the signal does not become 0 V, however, it is still lower than the single sensor response.

The second factor is regarding the difference between the noise sources, specifically magnetic noise, and electrical noise. In this experiment, the reduction of environment noise was investigated, with the bias magnetic field simulating the magnetic noise source. However, for electrical noise, in this case the noise coming from the circuitry, it is quite different, and it is independent of the bias magnetic field. Even at zero bias magnetic field, when there is a current flow, the resistance in the circuit will resulting a voltage reading. In the designed measurement setup, two different modules were used (Sensor 1 and Sensor 2), and although their circuit design are the same, they are built separately from each other. This in turn, will result in their own different electrical noise. Similar to the situation mentioned above, by subtracting their output, the result will not be 0 V.

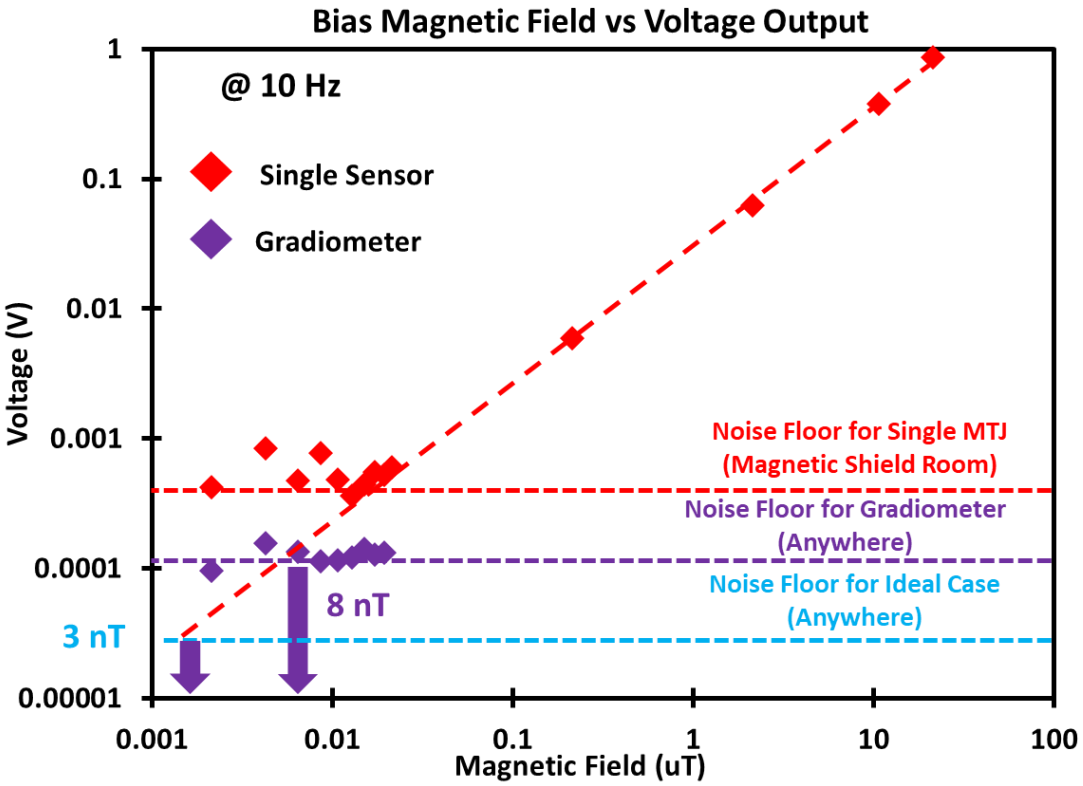

Figure 3.4: Result of adjusting the sensor sensitivity through calculations to simulate an ideal case. The blue line shows that the ideal detectivity is around 3 nT.

From our initial results, I tried to adjust the sensor modules sensitivity by multiplying the final sensor output in order to produce identical signal levels, or in other words to produce the most ideal case as mentioned previously. The results are shown in Figure 3.4, whereby in an ideal case, the detectivity is improved from 8 nT to 3 nT.

With this in mind, for future designs, combining the circuits for each module into one would be the way forward. Ideally, the resulting electrical noise would be lower than multiple circuits, thus resulting in a lower noise base level. However, since it is quite difficult to completely erase any electrical noise due to the nature of the circuitry, finding the right balance between the noise base level and the target measurement range is key for future applications. Another method is, to add another step in the circuit or data processing procedure of adjusting each sensor modules output to have identical signals. Nevertheless, in this gradiometric setup, the resulting detectivity is 8 nT.

3. 3 Summary

By measuring the response of the gradiometric setup towards a bias magnetic field with various intensity, the designed gradiometric setup detectivity was 8 nT. However, as mentioned in the previous chapter, there is a slight difference in their sensitivity value, resulting in a different output for each respective sensor module at each bias magnetic field. When their outputs are subtracted via the gradiometer method, the signal does not become 0 V, therefore the noise cancellation effect is does not perform as well. However, it is still lower than the single sensor response.

Another important point is regarding the difference between the noise sources, specifically magnetic noise, and electrical noise. In this experiment, the reduction of environment noise was investigated, with the bias magnetic field simulating the magnetic noise source. However, for electrical noise, in this case the noise coming from the circuitry, it is quite different, and it is independent of the bias magnetic field. Since the circuits are separate for each module, it is difficult to cancel the electrical noise.

Chapter 4: Baseline Optimization

4.1 Baseline Simulation

Before I begin with experimenting with the steel bar, I used simulation to determine the disturbance caused by a defect in a steel bar. The simulation software we used throughout the research is Magpylib [88], a free Python package for magnetic field computation. However, there are some limitations to the simulation program, thus the results will not reflect real world situation but will only serve as a guideline for my research.

The baseline optimization is important for the planar gradiometer because the signal depends on giving a single peak signal after subtracting the signals of sensor 1 module and sensor 2 module. The baseline is referred to as the total distance between the sensors, which is $2\,\Delta x$. From this point, we will refer the baseline as $2\,\Delta x$.

$$\boldsymbol{B_{Gradiometer} = B_y(0 + \Delta x) - B_y(0 - \Delta x) = 2B_y(\Delta x)} \qquad \textbf{4.1}$$

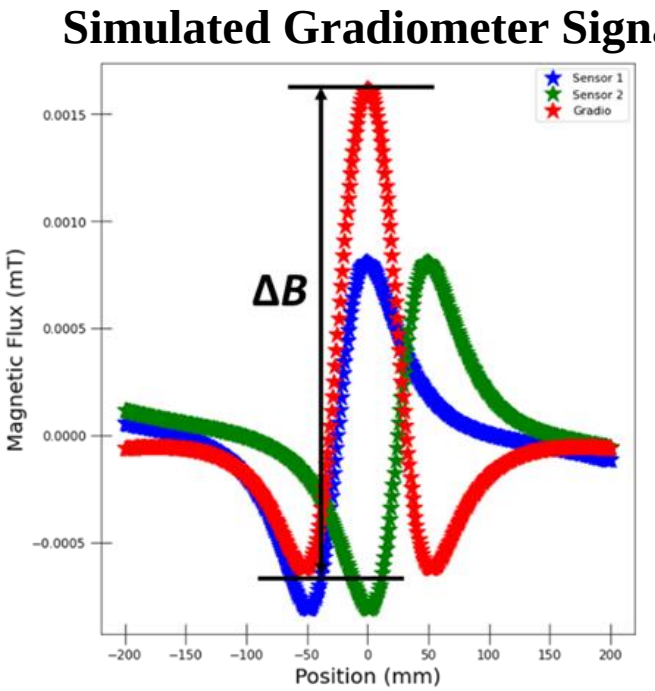

Figure 4.1: Simulated single sensor signal. The value of $2\,\Delta x$ corresponds to the distance between the peak and the trough.

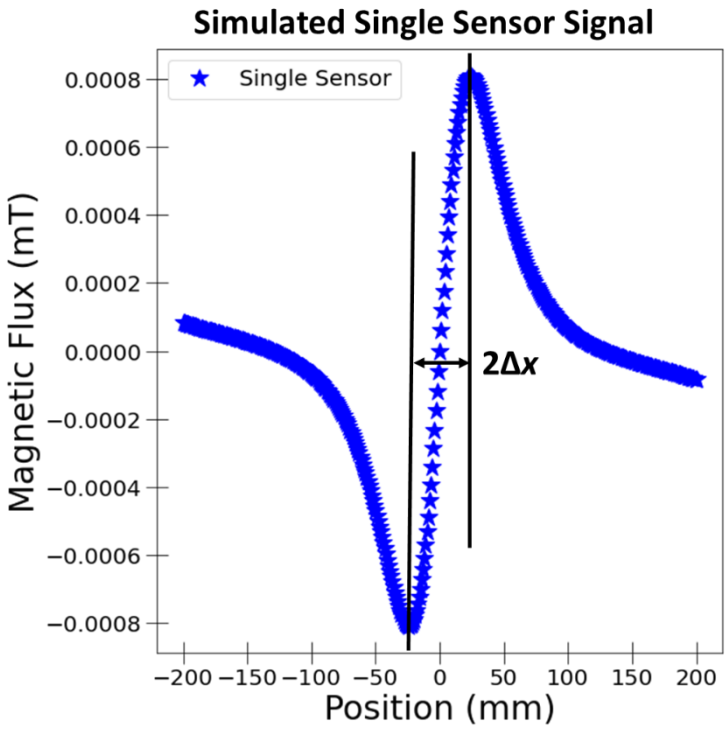

Figure 4.2: Simulated gradiometer signal. By shifting each sensor by a value of Δx, the corresponding trough of Sensor 1 Module and peak of Sensor 2 Module overlap. Subtracting the signals will result in a larger single signal peak.

From equation 4.1, I could see that when each sensor is placed at a distance of Δx from the point of origin, the gradiometer signal produced will be twice as large as the single sensor signal. As explained in Figure 4.2, by creating an overlap of the trough and peak of each respective sensors, the final gradiometer signal will create a larger single signal peak. The location of the signal peak will determine the location of the measured defect and from a practicality point of view, the single-peak signal is preferred than the peak-and-trough signal, since it is much easier to determine its precise location.

With the relationship established, it is important to find the best $2\Delta x$ value for our designed measurement system. Therefore, I proceeded with investigating the dependence of $2\Delta x$ on the final signal output. Although, it was investigated in previous reports [78], most of their investigated cases were of different samples.

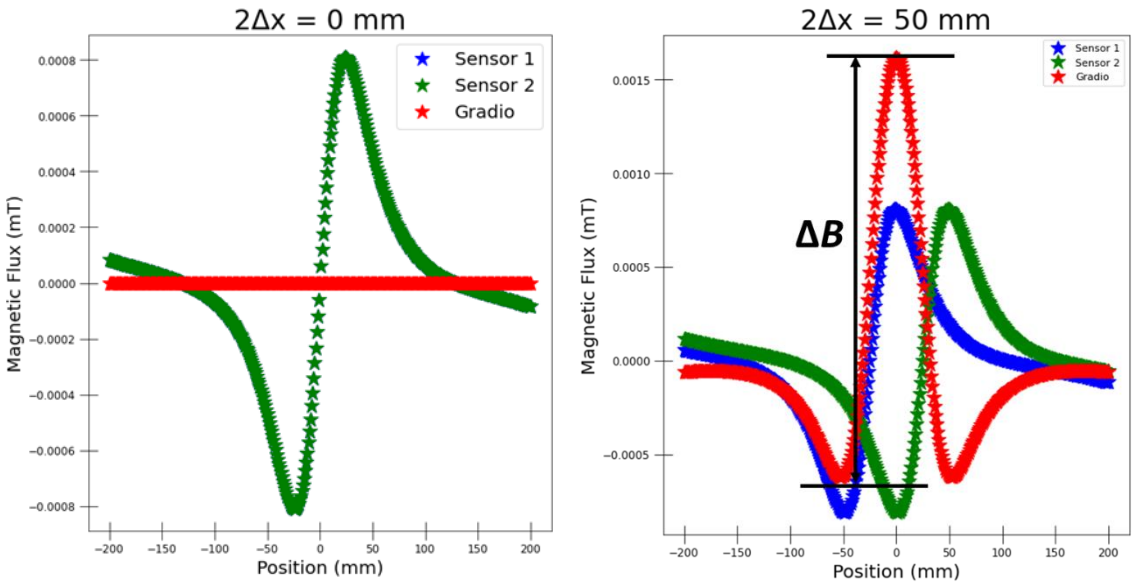

Figure 4.3: The figure shows the resulting magnetic field for each sensor and the gradiometer signal. The left figure shows for $2\Delta x = 0$ mm and the right shows for $2\Delta x = 50$ mm. The value of ΔB of the gradiometer signal is determined by the subtracting the highest peak with the lowest peak.

I simulated the steel bar specimen similar to that will be used in this research (d = 20 mm, l = 1000 mm, w = 2 mm), with a magnetization value of 2.3 mT. To simulate the positions of the MTJ sensors, I placed each sensor at a fixed lift-off of 4 cm, with varying baseline values ($2\Delta x = 0 \sim 10$ cm). Then I subtracted the signal output from each sensor to obtain the gradiometer signal as seen in Figure 4.3.

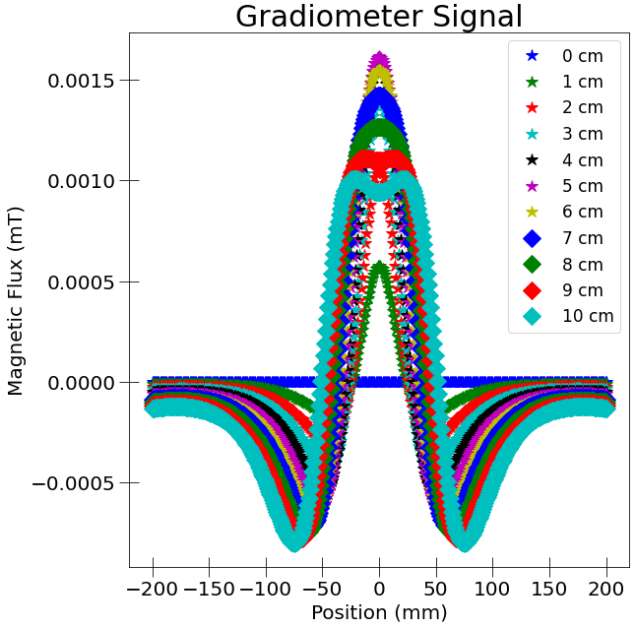

Figure 4.4: Compilation of the simulated gradiometer signal for their respective $2\Delta x$ value.

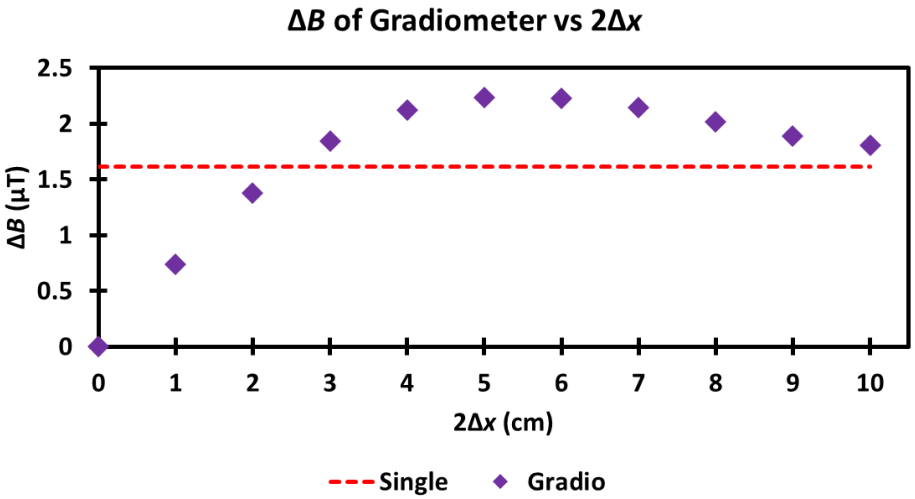

Figure 4.5: Comparison between the single sensor signal with the gradiometer signal for their respective $2\Delta x$ value.

From the results in Figure 4.4, it could be observed that the gradiometer changes the shape of the peak of the signal output from a peak-trough signal to a single peak signal, regardless of the $2\Delta x$ value. However, I observed that there is a dependence on the value $2\Delta x$ to the change in the gradiometer signal, as shown in Figure 4.5. The gradiometer signal increases with $2\Delta x$, however, at a certain point ($2\Delta x$ = 5 cm), the signal reaches its maximum point and starts to decrease after that point. This is due to the location of the peak and trough of the single sensors are not overlapping with each other; therefore, the gradiometer signal does not increase efficiently. The same could be said with the signal less than 5 cm.

From my simulations, the gradiometer signal did not reach twice of the single sensor signal. The single sensor was 1.6 μ T, whilst the gradiometer signal was 2.2 μ T. However, using the results as a guideline for the actual steel bar measurements, we understood several things. The first being that depending on the value of $2\Delta x$, the gradiometer signal changes, resulting in an improved signal peak or a deteriorating peak. Therefore, it is important to find the suitable value in order to obtain the best results. The second point is that the final signal may not be as predicted from theoretical calculations. From equation 4.1, it is predicted that the final signal would be twice as large as the original signal, however, it is not shown to be so from my simulation results. Although there is an increase in the gradiometer signal, the rate of which maybe not as theorize.

Nevertheless, since this is only a simulation, I need to further see how it actually effects the real environment measurements.

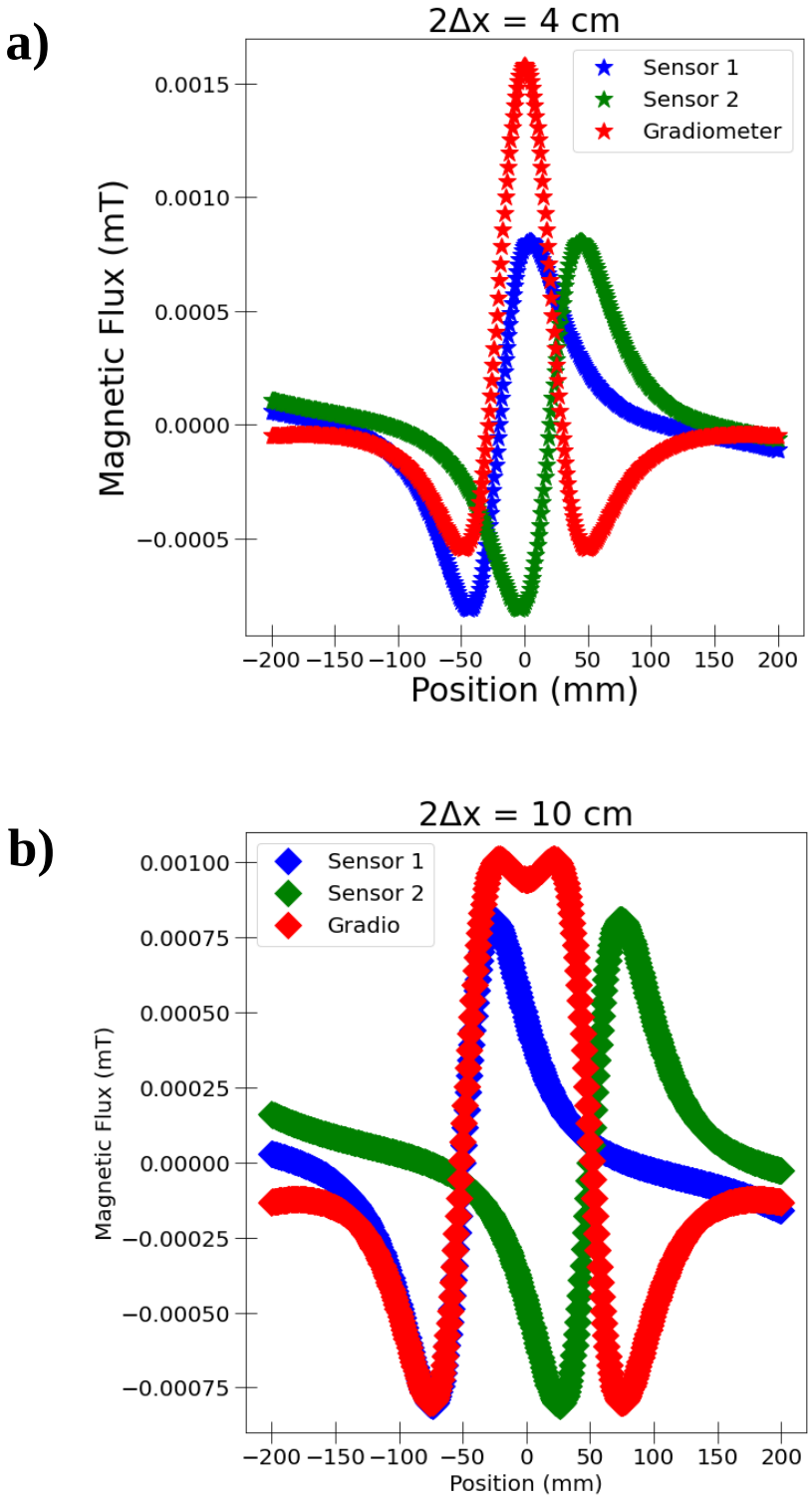

Figure 4.6: Gradiometer signal for $2\,\Delta x$ = 4 cm (a) and 10 cm (b). Due to the peak and trough of the single sensors do not overlap, it affects the final gradiometer signal value.

4.2 Steel Bar Measurements

Next, I moved on to the steel bar measurements to determine the best $2\Delta x$ for out MTJ based gradiometric sensor. For my initial experiments, I tried to determine the value of $2\Delta x$ based on the peak-and-trough signal of the single sensors, since as mentioned in the previous section, the distance of the peak and trough is equal to $2\Delta x$. The steel bar condition and experimental setup is as explained in Chapter 2, except I measured using each sensor module individually.

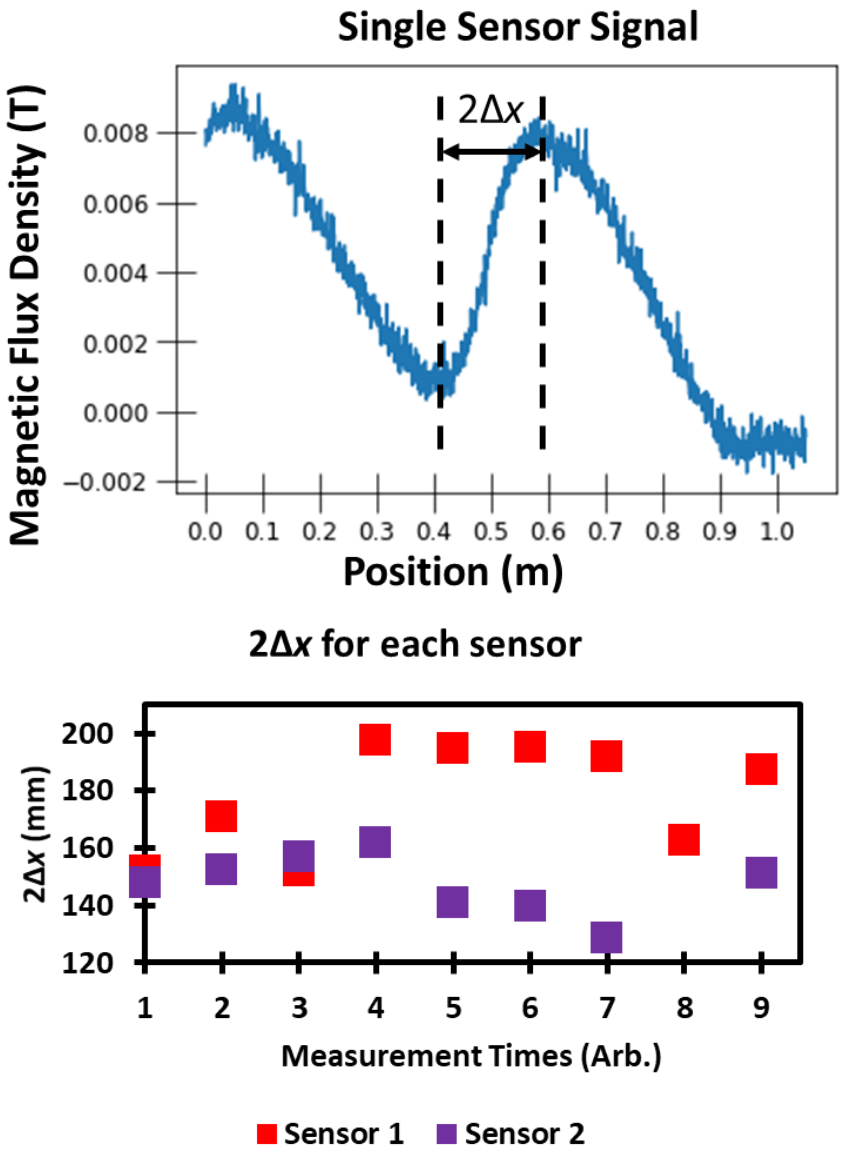

Figure 4.7: The top graph shows for single sensor signal for lift-off = 4 cm. The bottom graph shows the $2\Delta x$ for each respective sensor modules.

As seen in from the results in Figure 4.7, the single sensor produced a clear peak-and-trough signal, and from there I determined its distance. However, by doing multiple measurements for both modules (bottom graph of Figure 4.7), the value $2\Delta x$ for each sensor fluctuates with a range of 120 mm ~ 200 mm. From these initial results, it is difficult to determine the best value to be used in our gradiometric setup. Therefore, the next step is to compare the gradiometer signal using the range of $2\Delta x$ and determine the best value from the results.

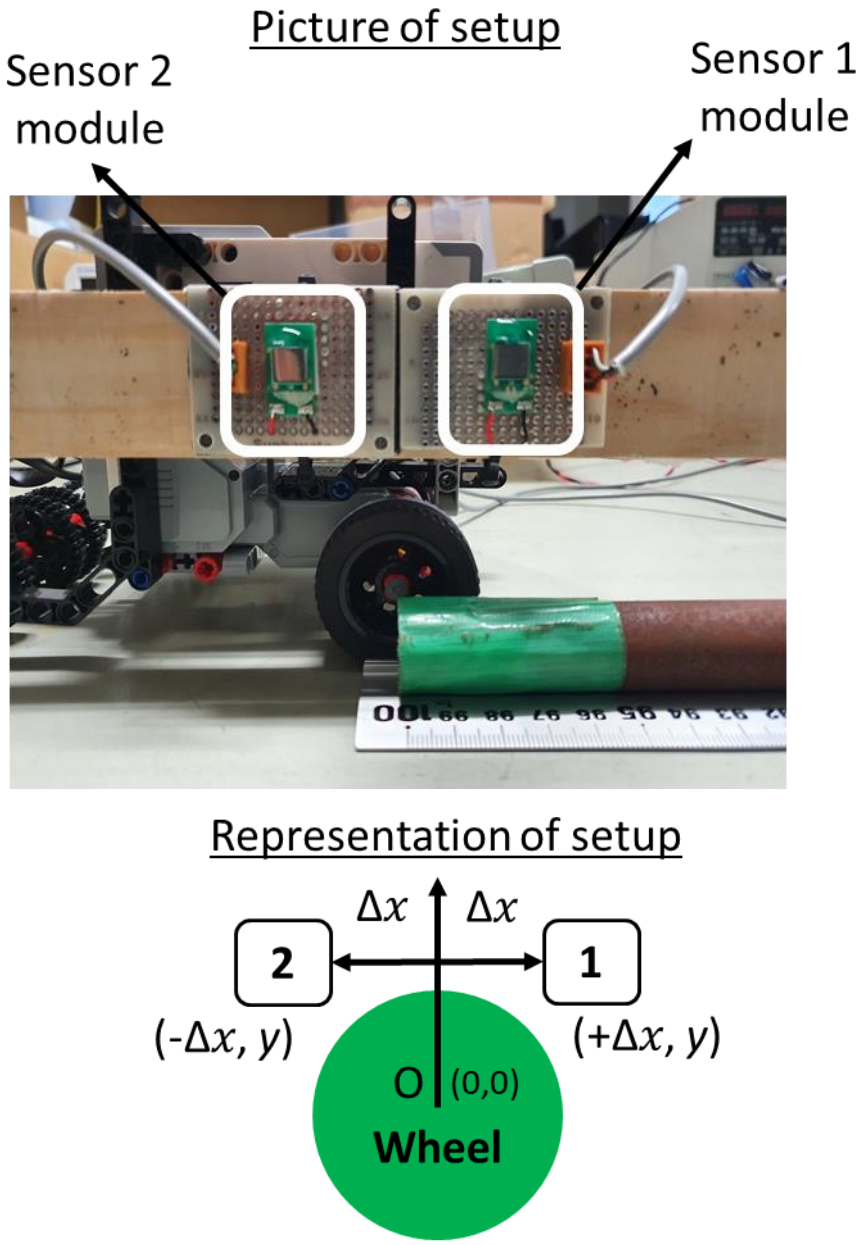

Figure 4.8: The top diagram shows the actual measurement setup. The bottom diagram shows how the value of Δx for each sensor is determined.

From the diagram in Figure 4.8, the MTJ sensor modules are attached on a board which is connected to the motor controlling unit which was explained in the earlier chapter. For our measurements, the point of origin where the value of Δx for each sensor module is determine from, is the centre of the wheel. By changing the distance of the sensor modules from the wheel centre, I could effectively determine the gradiometer signal with varying values of $2\Delta x$. The range of $2\Delta x$ investigated is based on the previous results ($2\Delta x$ = 120 mm ~ 200 mm), and I also measured at different lift-offs from 40 mm to 80 mm. This will help determine the effectiveness of $2\Delta x$ value at different lift-off. The gap width was set at 10 mm.

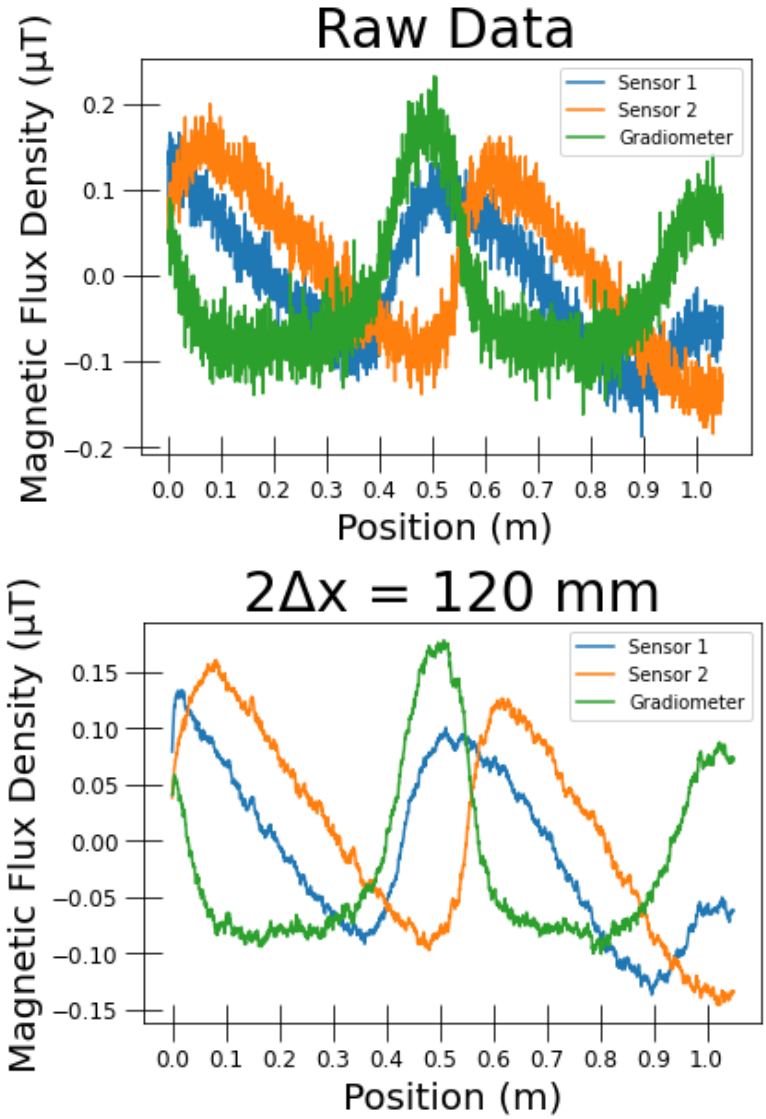

Figure 4.9: The results show the signals obtained at lift-off = 60 mm. The top graph shows for raw data values. Bottom graph shows the signal after smoothing averages process.

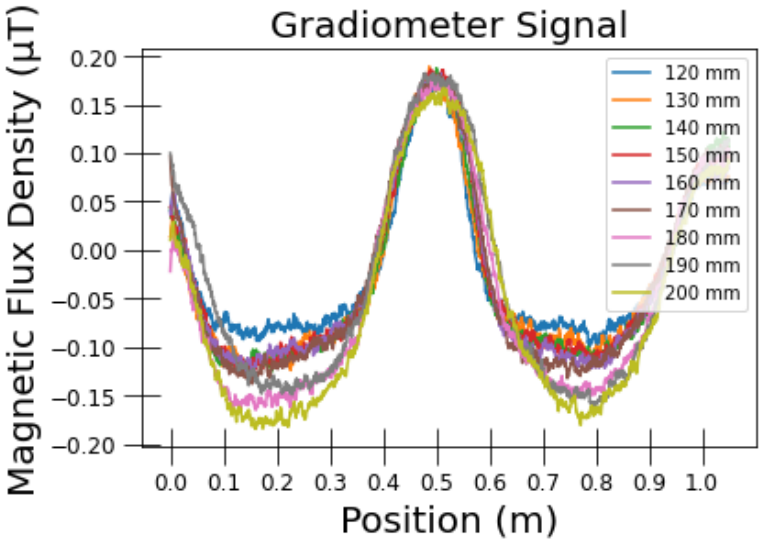

Figure 4.10: Compilation of gradiometer signal at lift-off = 60 mm for their respective $2\,\Delta x$

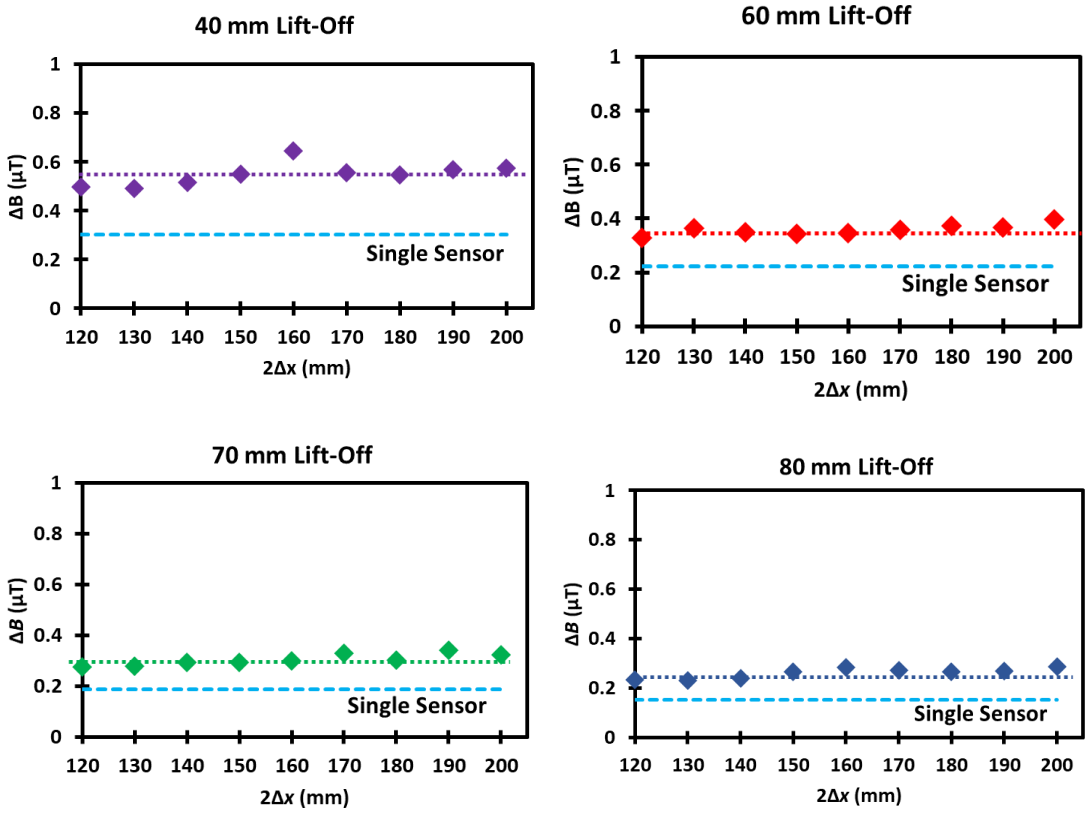

Figure 4.11: Compilation of single sensor and gradiometer signal at their respective lift-offs and $2\,\Delta x$.

Figure 4.9 shows the results for the $2\Delta x$ values at lift-off = 60 mm before and after smoothing averaging process. Since the amount data recorded, is quite large, it is difficult to determine the exact values from the raw data, therefore through the smoothing averaging process we could get a more accurate reading. From the results, I could see that the gradiometer signal corresponds well with that of the simulation results, whereby the peak-and-trough signal changes to a single peak signal. The final gradiometer signal for all $2\Delta x$ values at lift-off = 60 mm is shown in Figure 4.10. For better comparison, I compiled the measured data by comparing the gradiometer signal to the single sensor signal according to their lift-offs, as shown in Figure 4.11. From initial observation, the gradiometer signal is higher for all $2\Delta x$ values regardless of the lift-off. This corresponds well to both previous reports and my initial simulation results. However, contrary to the simulation results, the increased signal does not have an optimum value. Compared to the simulation results, whereby the gradiometer peak signal deteriorates and changes shape above certain $2\Delta x$ values, based on the results shown in Figure 4.10, there is no occurrence of that happening in our measured signal. In fact, all signals were clear single peak signals. Therefore, based on the results, regardless of the lift-off, my gradiometer setup showed no dependence on the $2\Delta x$ values, thus no optimum value could be determined since all gradiometer signal results were similarly larger than the single sensor results.

4.3 Gap Location Prediction

Based on the measured results, my designed gradiometric system using MTJ sensors produced improved signals independent of the $2\Delta x$ values at various lift-offs. However, it is also important to make sure the system is able to accurately predict and locate the gap position. From the gradiometer signal, as mentioned in the previous sections, the gap is determined by the position of the peak, which makes it easier and more reliable than the single sensors' peak-and-trough signal. Therefore, using the results obtained in Figure 4.10, I determined the systems predicted gap location for each $2\Delta x$ values at their respective lift-offs.

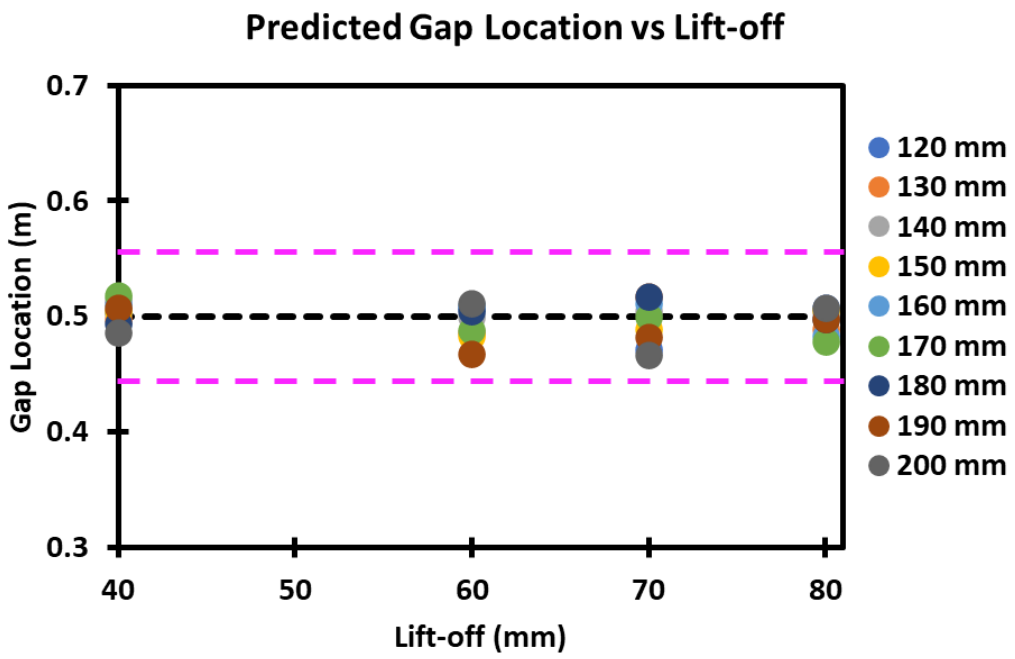

Figure 4.12: Compilation of predicted gap location for each $2\Delta x$ values at their respective lift-offs. The dashed line indicates the actual gap location which is at 0.5 m. The pink dashed lines indicate the accepted error rate of $\pm 10\%$.

The results are as shown in Figure 4.12. From observing the results, I could see that predicted gap location has a large distribution. There are not many reports mentioning the acceptable error rate in real life non-destructive testing, therefore I assumed that if the predicted gap location is within $\pm 10\%$ error of the actual location, it is considered viable. From that condition, our designed system could predict the location of the gap with acceptable accuracy, independent of $2\Delta x$.

4.4 Discussion

As mentioned in the results above, the results from my gradiometric sensor system differs from the previous reports and our simulation results, in the sense that there is no clear correct value for $2\Delta x$ of the gradiometer. In fact, from all of the data we obtained, our system was able to successfully increase the overall signal and determine the location of the gap with accuracy.

Based on previous reports, the Δx is optimal when it is equal to the lift-off, as seen in the equation below

$$\Delta x = \sqrt{w^2 + y^2} \qquad \textbf{4.2}$$

In the equation, w is the width of the defect while y is the lift-off. From the equation, since the lift-off of our measurement as considerably larger than the width $y >> w$, the value of Δx is equal to the value of y, which means $2\Delta x$ is twice of the lift-off value. Taking that into consideration, from our experiments at lift-off 60 mm, 70 mm, and 80 mm, the highest signal should be when $2\Delta x$ is 120 mm, 140 mm, and 160 mm respectively. However, as mentioned in the previous section, the gradiometer signal continued to increase even after the predicted optimal value.

There are several reasons that I think have a factor in this difference. The value of $2\Delta x$ is also the distance between the peak and trough signal of the single sensor since the gradiometer is taking the subtracted value of the MTJ sensor modules' 2 peak and MTJ sensor modules' 1 trough. Therefore, I should be able to determine the optimum value by analyzing the single sensor signal. However, as seen in Figure 4.7, the value has a large distribution and there is no constant value for each respective sensor. This may be due to the effect of the electrical noise and the recorded data during the measurements. As stated in the previous chapter, gradiometer system was able to reduce the effect of magnetic noise, assuming that both sensor modules are being affected by the same noise intensity. However, for electrical noise it is quite different since both modules use separate circuits (although identical). The fluctuations seen the raw data could be coming from the electrical noise and because the data is recorded for every 0.5 mm in 1000 mm, even the slightest fluctuation could cause a large impact on the final peak value. The simple solution is to record less data points, however, that will come at a cost of accuracy. The next best thing is to combine the circuits into one large circuit as previously mentioned.

One of the factors is in the previous reports, the measurement condition is not similar. The first difference is that the measured sampled and defects are not similar to ours, in their case the sample was a steel plate with rectangular slots as the target defect. Compared to mine, which is gap between steel bars. Therefore, using their calculations

and results as a direct comparison is not ideal. Another factor is the target lift-off, with previous measuring at an order of < 10 mm lift-off, compared to our lift-off values in the order of several centimeters. At lower lift-off, having a larger $2\Delta x$ might have a larger influence on the final gradiometer signal, with a much larger signal, and the change in the magnetic field distribution is more abrupt since the magnetic dipoles (defects) are located closer to the sensors.

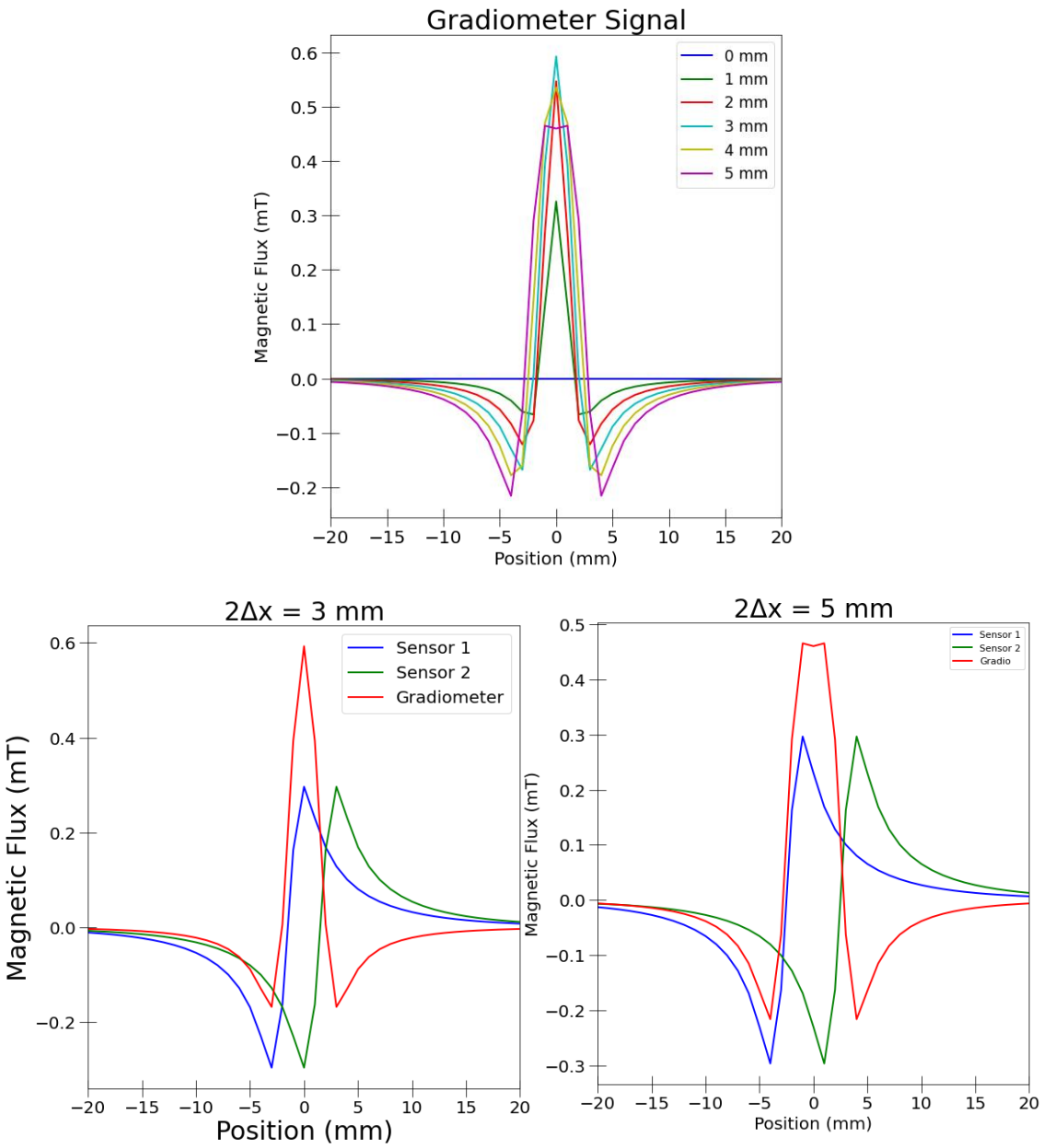

Figure 4.13: Simulation of gradiometer signal at lift-off = 1 mm. Top graph shows for $2\Delta x$ values from 0 mm to 5 mm. Bottom graphs show for $2\Delta x$ = 3 mm and 5 mm

I conducted another simulation to investigate the gradiometer effect at a low lift-off (1 mm), the other simulation conditions were similar to the previous simulations at higher lift-off. From the results in Figure 4.13, it is clearly seen the difference between the signals. At low lift-offs, a change in the $2\Delta x$ of the mm order is enough to change the gradiometer signal significantly, whereas at high lift-off, the order is in the cm (results in Figure 4.4 and 4.6). The simulation confirms that at low lift-off (mm order), the $2\Delta x$ value has a larger impact on the signal compared to higher lift-off values. Since the effect is not as large at high lift-offs, this could explain why in my experiments, the gradiometer signal in independent of the $2\Delta x$ values.

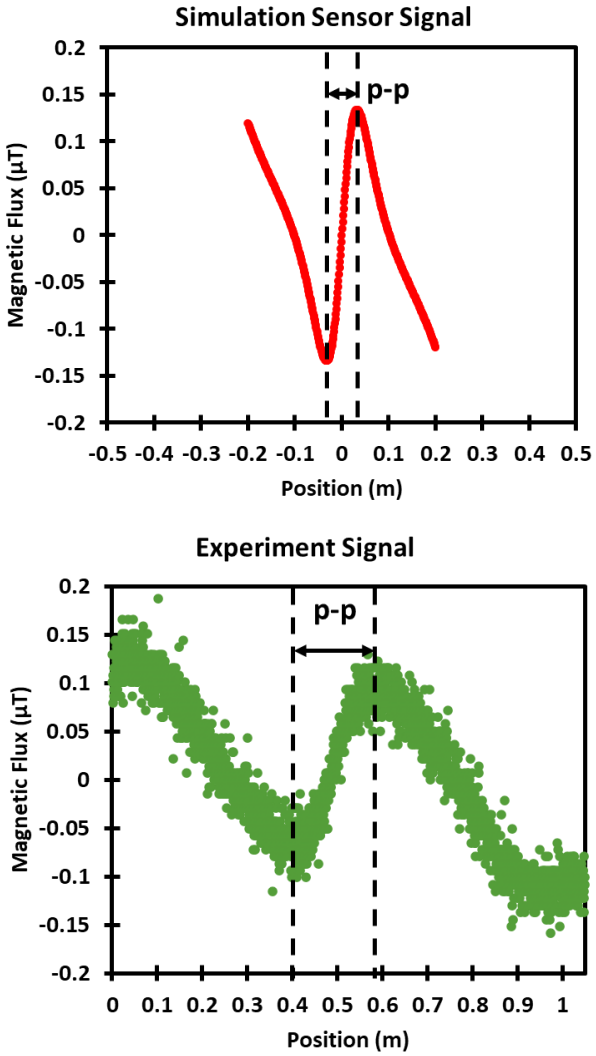

Figure 4.14: Simulation and experiment signal (gap width = 1 mm, lift-off = 60 mm).

Another factor might be the large sensing area of the MTJ sensors themselves. Each MTJ sensor unit consists of 1764 MTJ structures in series configuration. This large amount of structures results in a large sensing area of 7x7 mm^2. In other words, the resulting sensor signal is the average magnetic flux reading of all the MTJ structures in the sensing area. As seen in Figure 4.14, this results in the peak-to-peak (p-p) value of the simulation signal and the real experiment signal to have a large difference, with the p-p of the former being 0.067 m and the latter being ~0.2 m. This large or broad p-p value might have an effect on the gradiometer signal being independent of the $2\Delta x$ values. Unfortunately, the simulation software that I used was not able to simulate the exact response of the MTJ sensors, let alone each individual MTJ structure.

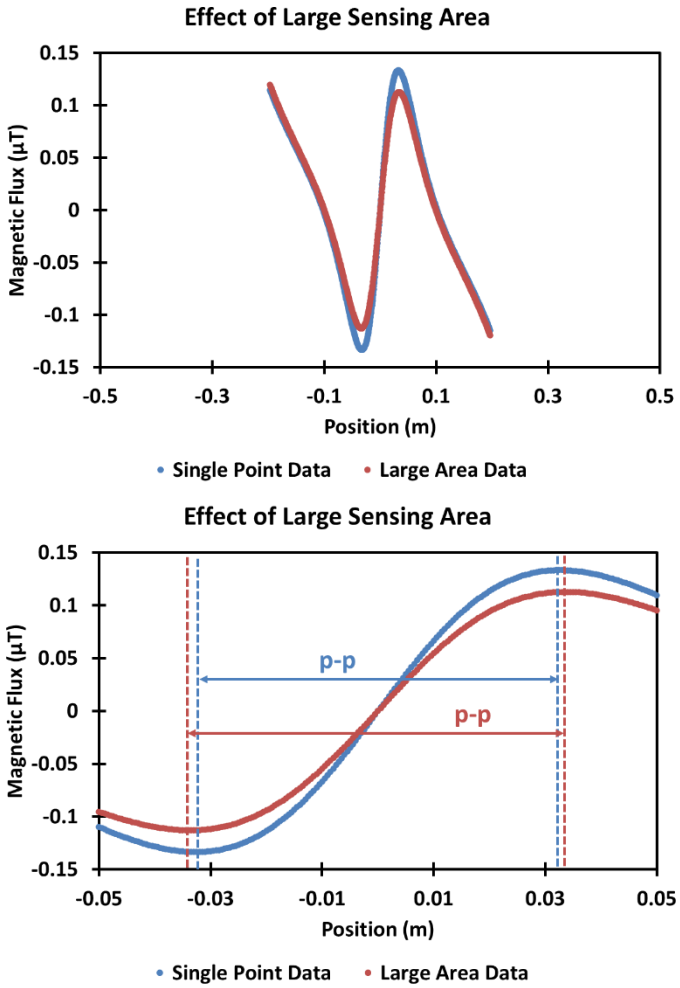

Figure 4.15: Simulation and experiment signal (gap width = 1 mm, lift-off = 60 mm). The bottom graph shows a smaller *x*-axis range.

However, by simulating the large sensing area, I was able to observe a slight broadening of the p-p value. From the results in Figure 4.15, compared to the single point signal's p-p value (0.065 m), the larger sensing area signal was slightly larger (0.067 m). From these results, the extent of the broadening is still not quite as large as the real experiment p-p value, therefore the large sensing area may not have that much influence in the broadening of the signal.

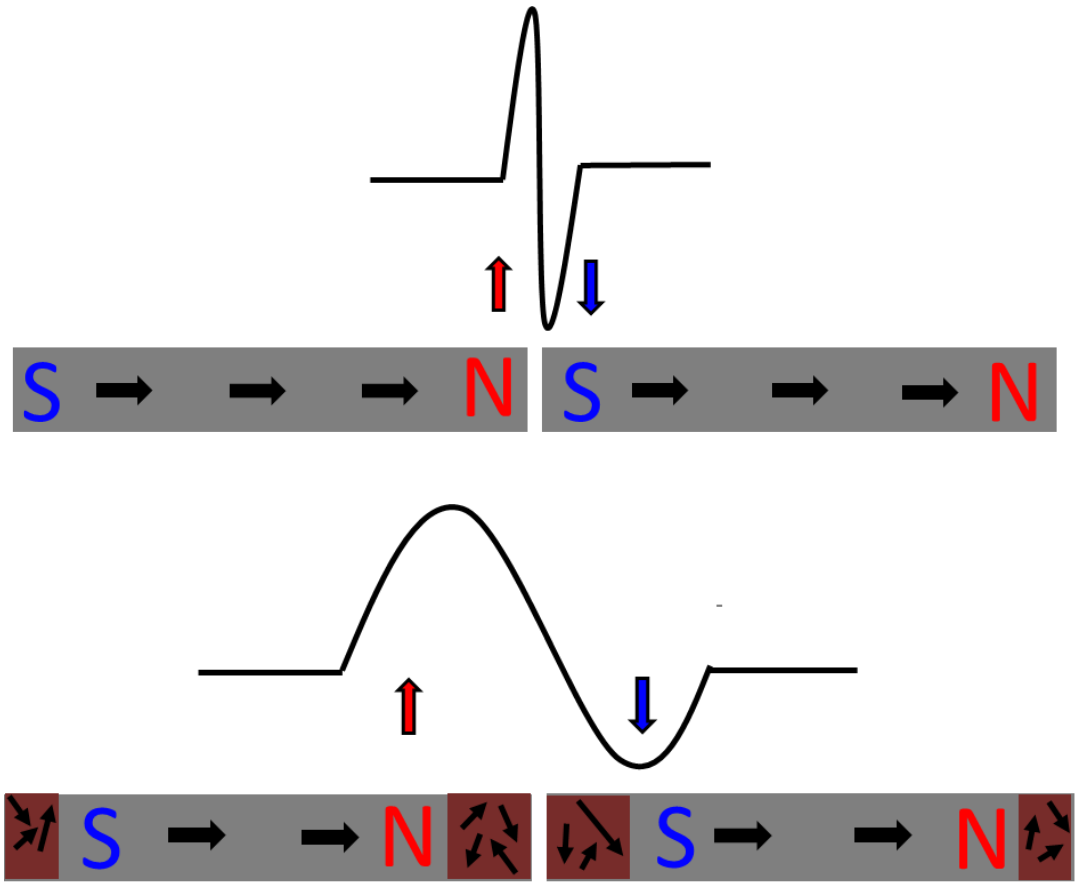

Figure 4.16: Top figure shows for the ideal case, where the magnetic poles are located at the edge, resulting in a sharp peak. Bottom figure shows for the predicted situation for the experiment case, where the magnetic poles are located further from the edge.

Another consideration is the difference of the magnetization state of the steel bars for the ideal case (simulation) and the experiment case. Ideally, in a fully magnetized state, the North and South magnetic poles are located at the edge of the steel bars, as shown in the top figure in Figure 4.16. In this state, the sudden change in the magnetic poles, will cause the resulting signal to produce a sharp peak, as observed in the

simulation results. In contrast, in the experiment case, since the magnetization intensity used is not strong enough to fully magnetized the steel bar, some parts may be demagnetized. As seen in the bottom figure of Figure 4.16, the demagnetized parts of the steel bar, will cause the magnetic poles to shift further away from the edge of the steel bars. From this, the signal will also shift in response to the magnetic poles, resulting in a broader peak. Due to the demagnetized parts present in the steel bars, I believe that it is the reason as why the experiment produces broader peaks, resulting in the independence of the ΔB value to the $2\Delta x$.

Based on the theory above, I think that is why there are some differences to our measurement results compared to other groups and my simulation results. Nevertheless, the results showed that the designed gradiometer managed to change the single sensor signal into a single peak for better detection, with an increase in the signal and accurate gap prediction. Since there is no evidence of a best value for $2\,\Delta\,x$ in our results, I proceeded with choosing 140 mm as our $2\,\Delta\,x$ for the forthcoming experiments, since it still improved on the single sensor signal and it was easiest value to set up for the experiments.

4.5 Summary

From the simulation it could be observed that the gradiometer changes the shape of the peak of the signal output from a peak-trough signal to a single peak signal, regardless of the $2\,\Delta\,x$ value. However, it was observed that there is a dependence on the value $2\,\Delta\,x$ to the change in the gradiometer signal, as shown in Figure 4.5. The gradiometer signal increases with $2\,\Delta\,x$, however, at a certain point ($2\,\Delta\,x$ = 5 cm), the signal reaches its maximum point and starts to decrease after that point. This is due to the location of the peak and trough of the single sensors are not overlapping with each other; therefore, the gradiometer signal does not increase efficiently.

Next, I moved on to the steel bar measurements to determine the best $2\,\Delta\,x$ for out MTJ based gradiometric sensor. For the initial experiments, I tried to determine the value of $2\,\Delta\,x$ based on the peak-and-trough signal of the single sensors, since as mentioned in

the previous section, the distance of the peak and trough is equal to $2\Delta x$. The results showed that the designed gradiometer managed to change the single sensor signal into a single peak for better detection, with an increase in the signal and accurate gap prediction. From my investigation, however, it is understood that in contrast to the previous report, there is no dependence on the $2\Delta x$ value on the gradiometer output, in other words, there is no optimum $2\Delta x$ value, where the output signal is at its maximum. Some of the reasons might be due to difference in lift-off values. At lower lift-off, the change in magnetic flux density is much more abrupt, therefore the slightest change in $2\Delta x$ has a large impact on the output, while at higher lift-off, the change is less abrupt, thus allowing for a larger acceptable range of $2\Delta x$. Another factor might be due to the large sensing area of the MTJ sensors. Through simulation, it is understood that a larger sensing area will cause the p-p values of the single sensor to become broader, and this might have caused the gradiometer signal to become independent $2\Delta x$. However, from the results, it might not have a significant influence in the final signal broadening. The next factor that I considered is that for the experiment case, some parts of the steel bars are demagnetized, causing the magnetic poles to shift away from the edge of the steel bars. This results in the signal to become broader, in contrast to an ideal case from the simulations, where the magnetic poles are located at the edge, resulting in a sharp peak. Since there is no evidence of a best value for $2\Delta x$ in our results, I proceeded with choosing 140 mm as the $2\Delta x$ for the forthcoming experiments.

Chapter 5: Investigation of Gap Width and High Lift-Off Performance

5.1 Gap Width Dependence

However, in real life cases, gap width as large as 10 mm is an extreme case, therefore it is important to investigate the ability of my system to measure gaps at a smaller scale. Using the gradiometer conditions concluded from the previous chapter, we measured the steel bars with gap widths ranging from 1 mm ~ 10 mm, and at various lift-offs (40 mm, 60 mm, 70 mm, 80 mm, and 90 mm). Measuring at varying lift-off would also help confirm the sensors' ability to differentiate them at high lift-offs. The gap width of the steel bars was calibrated with vernier callipers to ensure their distances were accurate as possible.

I will also be looking at the accuracy of the system for smaller gap widths. As mentioned before, not only is the improvement of the sensor important, the accuracy of the predicted gap location is also vital for non-destructive testing. The error rate that I adapted throughout the measurement is $\pm 10\%$ within the actual location, i.e., between 0.45 m ~ 0.55 m, is deemed accurate.

5.1.1 ΔB vs Gap width

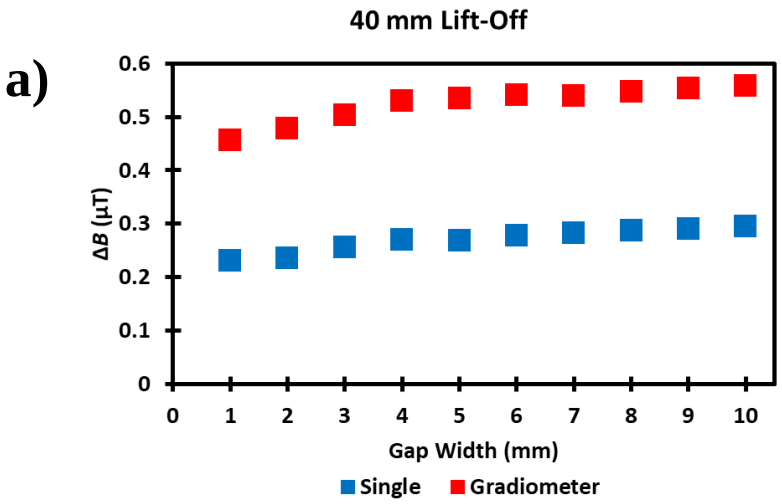

b)

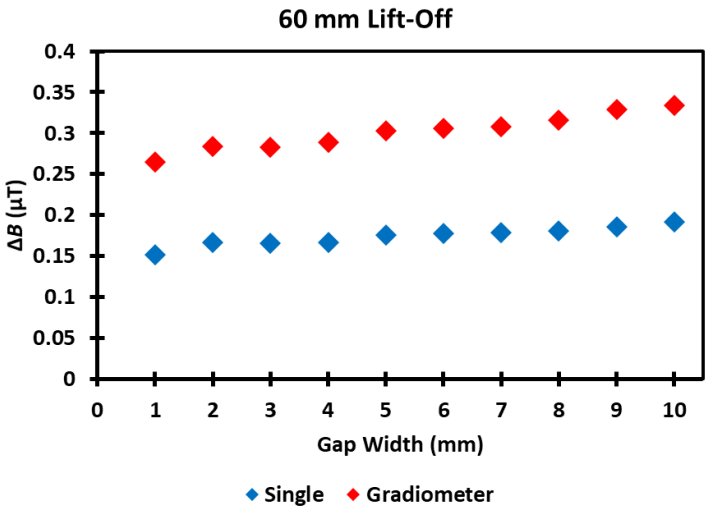
60 mm Lift-Off
ΔB (μT)
0.4
0.35
0.3
0.25
0.2
0.15
0.1
0.05
0
0 1 2 3 4 5 6 7 8 9 10
Gap Width (mm)
Single
Gradiometer

c)

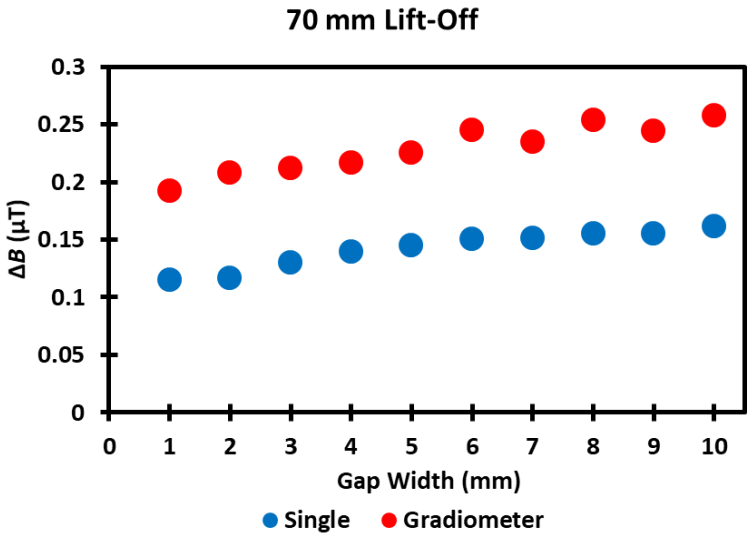
70 mm Lift-Off
ΔB (μT)
0.3
0.25
0.2
0.15
0.1
0.05
0
0 1 2 3 4 5 6 7 8 9 10
Gap Width (mm)
Single
Gradiometer

d)

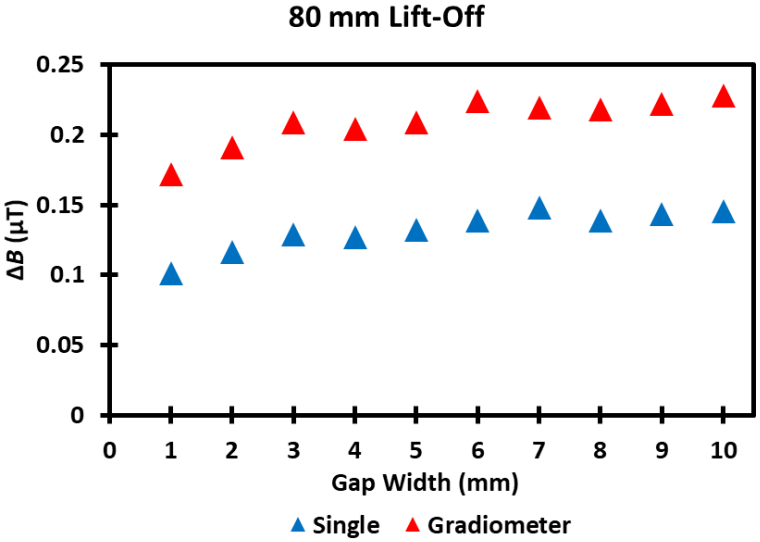
80 mm Lift-Off
ΔB (μT)
0.25
0.2
0.15
0.1
0.05
0
0 1 2 3 4 5 6 7 8 9 10
Gap Width (mm)
Single
Gradiometer

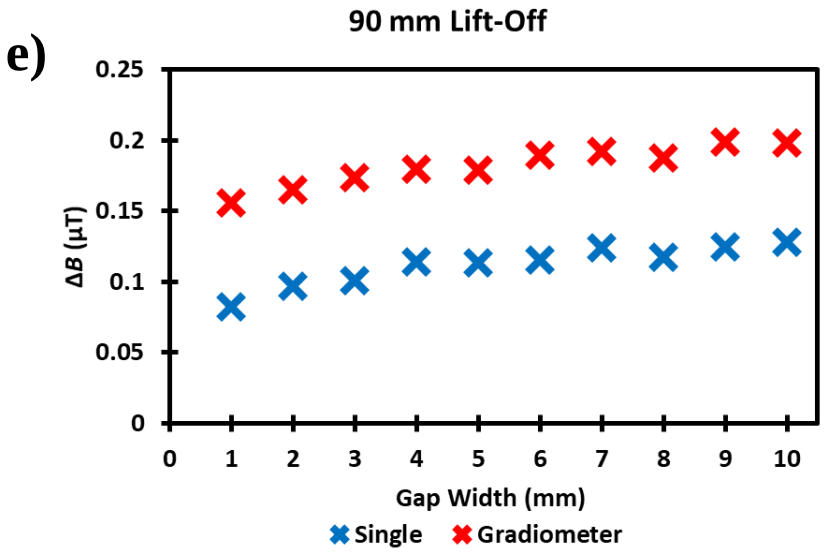

Figure 5.1: Results of the gap width dependence on ΔB, for their respective lift-offs. (a) 40 mm, (b) 60 mm, (c) 70 mm, (d) 80 mm, and (e) 90 mm.

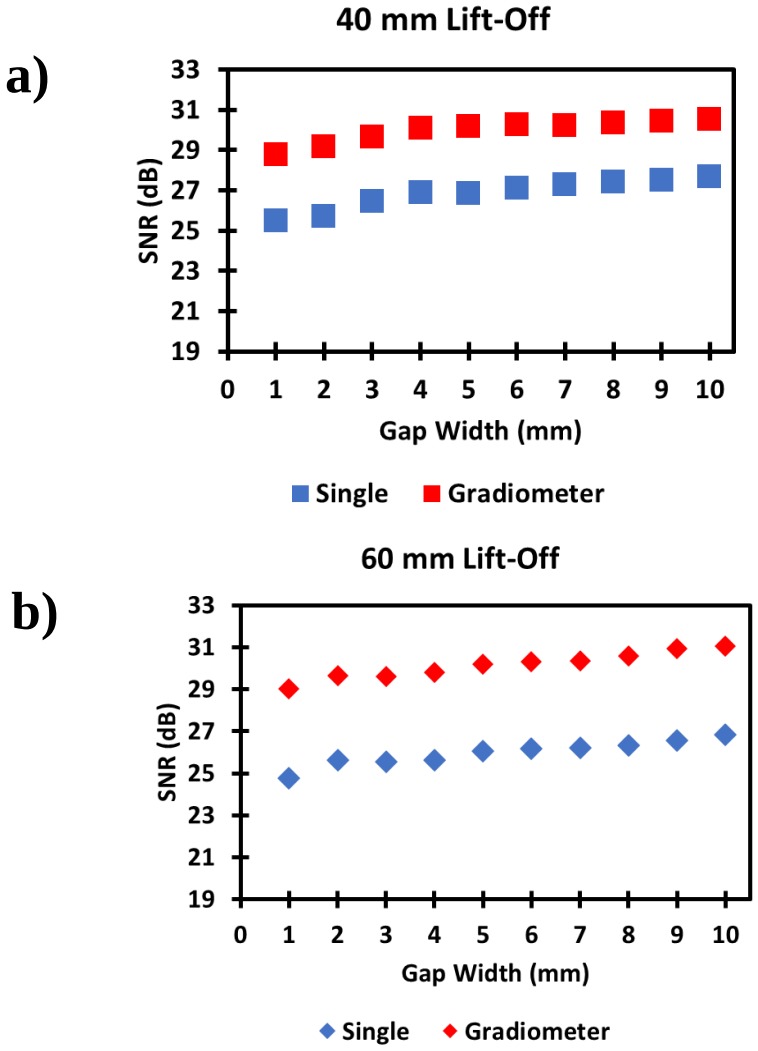

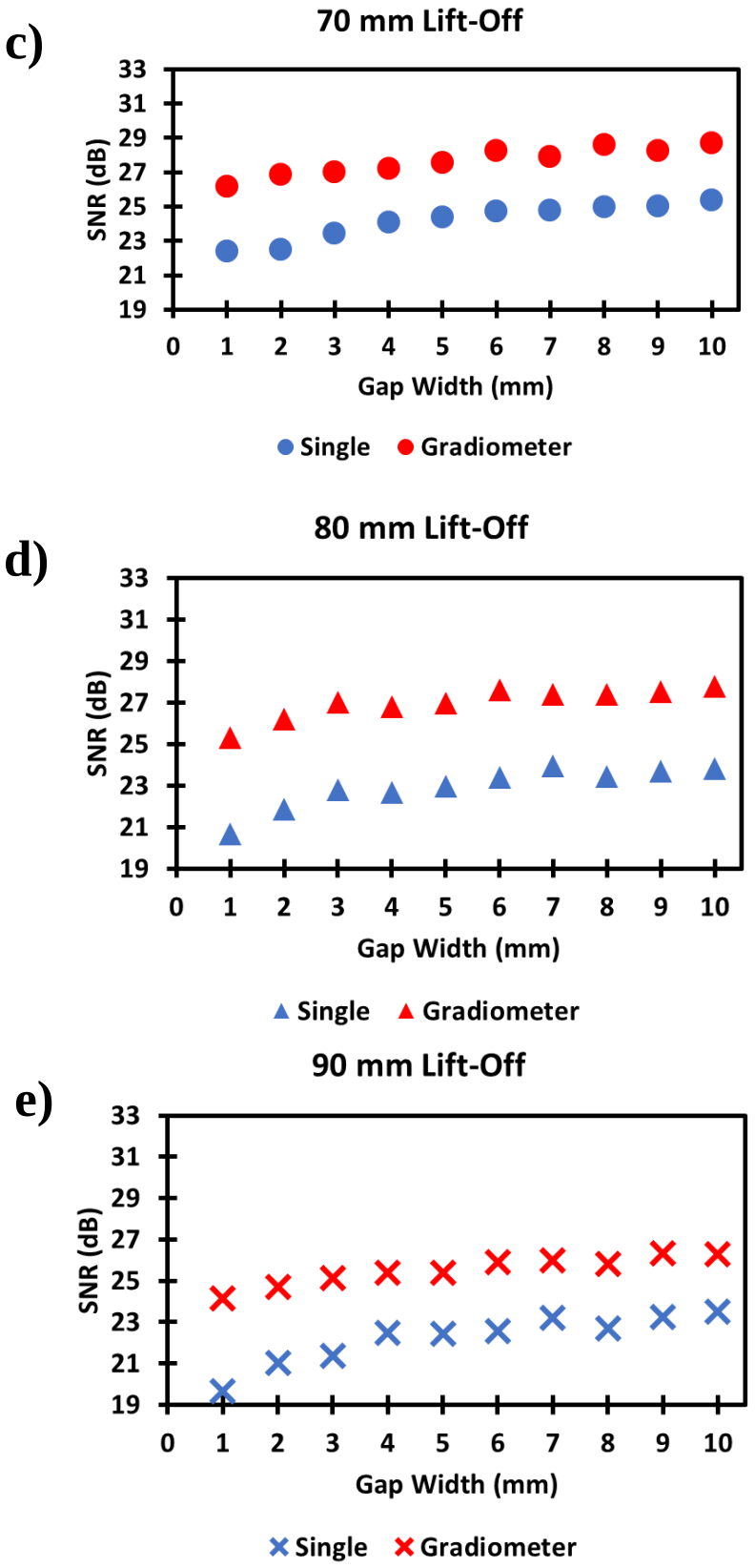

Figure 5.2: Results of the SNR for their respective lift-offs. (a) 40 mm, (b) 60 mm, (c) 70 mm, (d) 80 mm, and (e) 90 mm.

The results for all the measurements are shown in Figure 5.1 according to their respective lift-off values. For every measurement, it could be clearly seen that all gradiometer signals are always higher than the single sensor signal, as expected. It could also be observed that there is a linear-like relationship to the signal as the gap width increased for both signals. Compared to the single sensor results, the gradiometer system performed better at increasing the overall signal (>50% increase). In addition, by observing the signal-to-noise ratio (SNR) of each respective measurement, the gradiometer constantly performed better than the single sensor setup, as shown in Figure 5.2. Although it is not as predicted in theory, it shows potential for application in real world situation.

5.1.2 Gap Location Prediction

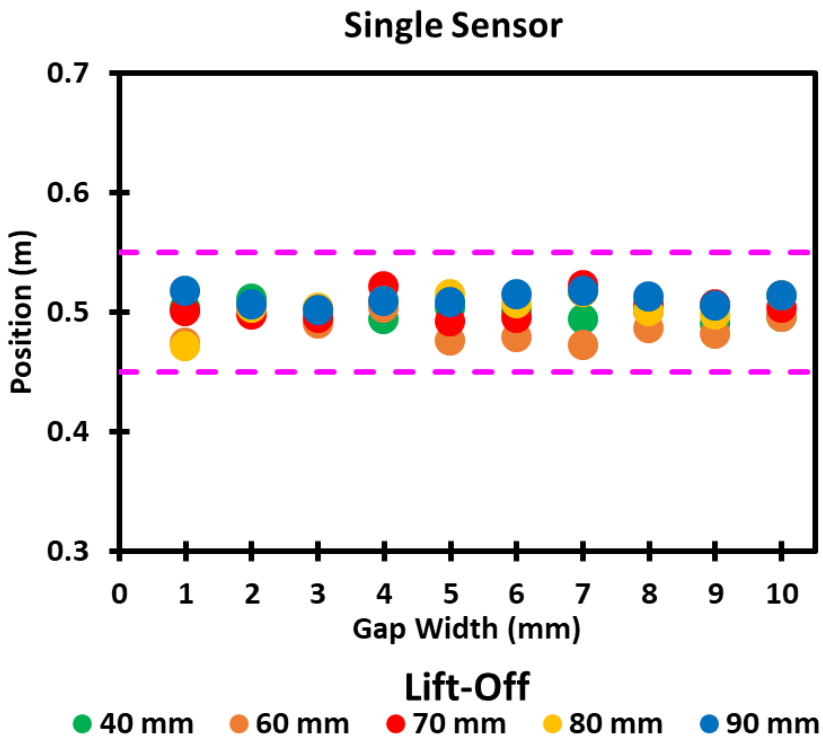

Figure 5.3: The predicted gap location for the single MTJ sensor module. Pink dashed lines indicate the maximum and minimum distribution.

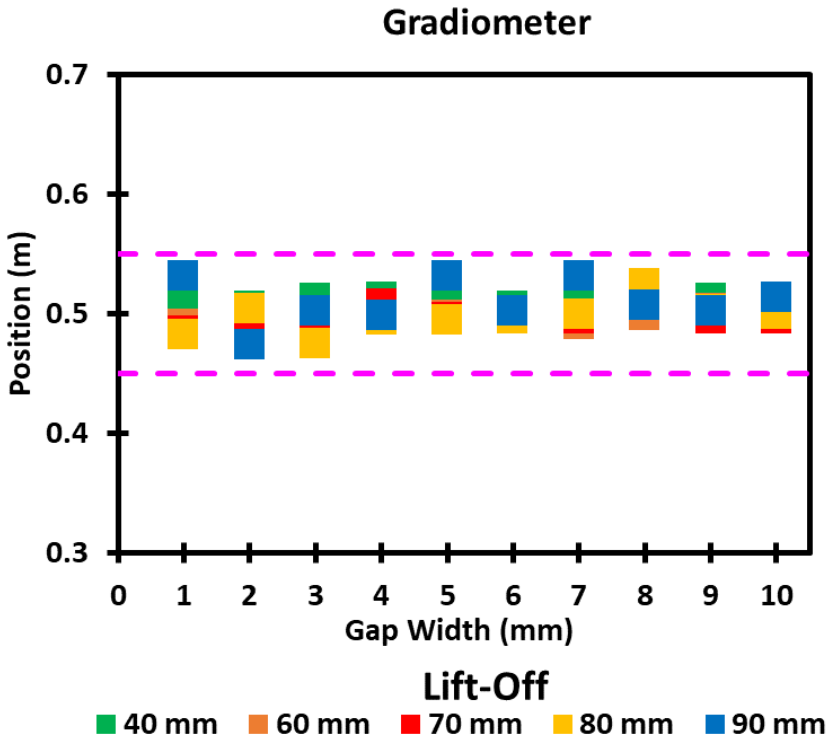

Figure 5.4: The predicted gap location for the gradiometric sensor system. Pink dashed lines indicate the maximum and minimum distribution.

From Figure 5.3 and Figure 5.4, both setups predicted the gap location within the accepted error range. Comparing both results, both gradiometer and single setup have large distribution on their predicted value, especially for gradiometer at 90 mm. Nevertheless, I can confirm that the MTJ based gradiometric system is able to predict the location of the gap within an error rate of $\pm 10\%$.

5.1.3 Discussion

From the results, in section 5.1.1, I could see that the at either measurement setup, both signals had a linear-like dependence to the gap width. The relationship could be better explained by the equation below:

$$\boldsymbol{m} = pl \qquad \textbf{5.1}$$

where,

$\boldsymbol{m}$ = magnetic dipole moment, p = magnetic pole strength, l = vector separating

By focusing on the ***m*** (magnetic dipoles) as in equation 5.2, I understood that it relates to the p (magnetic pole strength) and l (vector separating the dipoles). In our gap width dependence measurements, I can assume that p does not change, only l since it can be attributed to the gap width. Therefore, it is proven that the gap width has a linear dependence on the overall magnetic flux signal, assuming that the measurement is taking place at the same lift-off.

5.2 High Lift-off Performance

5.2.1 ΔB vs Lift-Off

Since my target for the gradiometric system is to be able to measure at high lift-offs, I investigated its ability to measure the steel bar with larger increments in the lift-off value. The gap width is set to 10 mm throughout the measurements, at lift-offs = 40 mm, 80 mm, 120 mm, 160 mm, 200 mm.

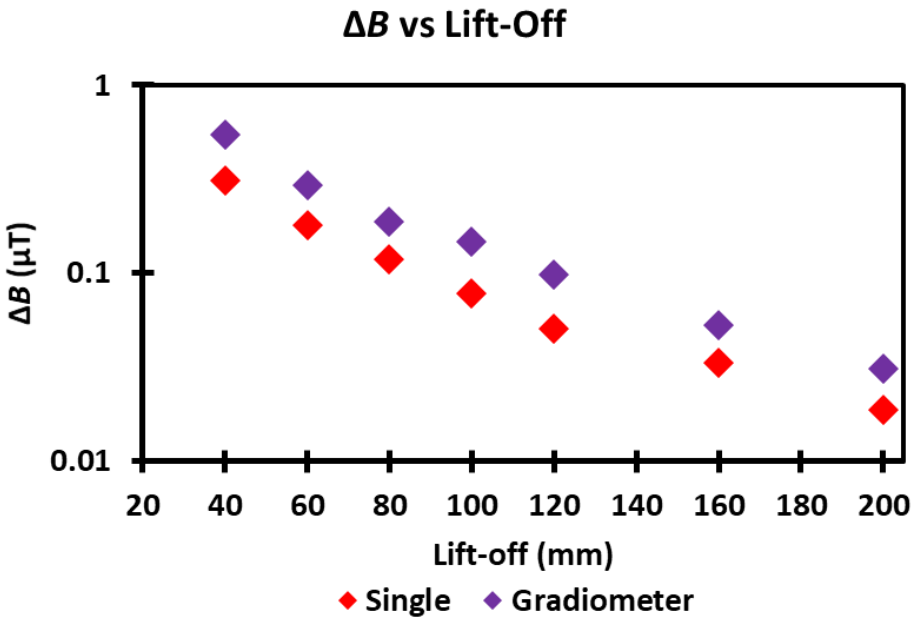

Figure 5.5: ΔB for single sensor and gradiometer setup at different lift-offs.

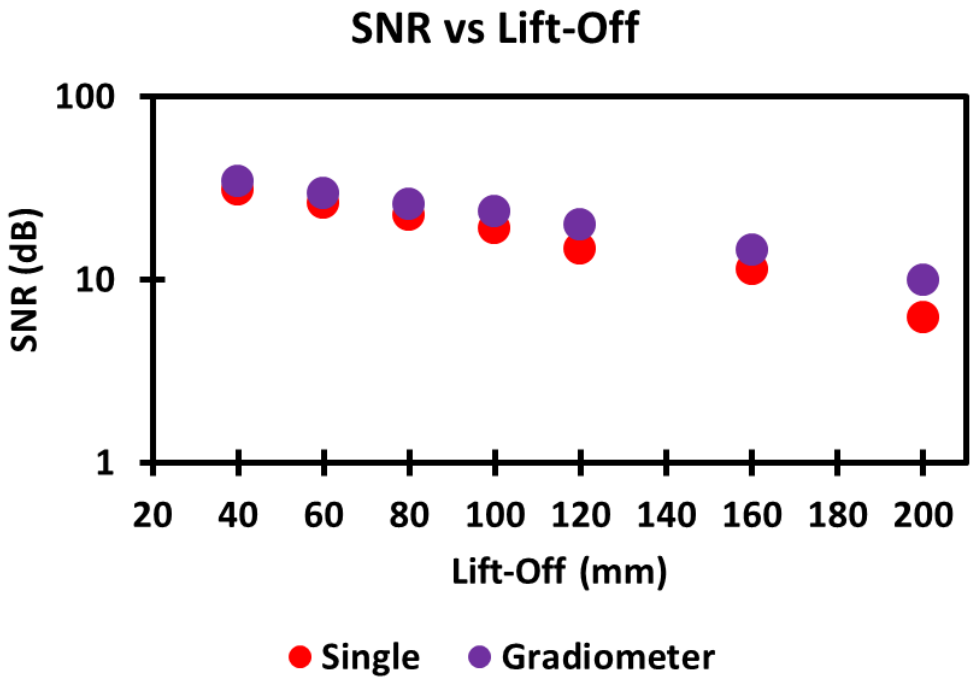

Figure 5.6: SNR for single sensor and gradiometer setup at different lift-offs.

Based on the results in Figure 5.5 and Figure 5.6, an increase in lift-off will result in the decrease in sensor signal, regardless of the setup. This agrees well with the magnetic dipole theory, which states that the magnetic flux density is heavily dependent on the lift-off value. As predicted, the gradiometer is able to increase the sensor signal across all lift-off values, as well maintaining a large SNR value compared to the single sensor regardless of lift-off.

5.2.2 Gap Location Prediction

It is also important to confirm the effectiveness of the sensor to predict the location of the gap. Similar to the previous section, I set the condition of accuracy to be within ±10% of the actual gap location (0.45 m ~ 0.55 m).

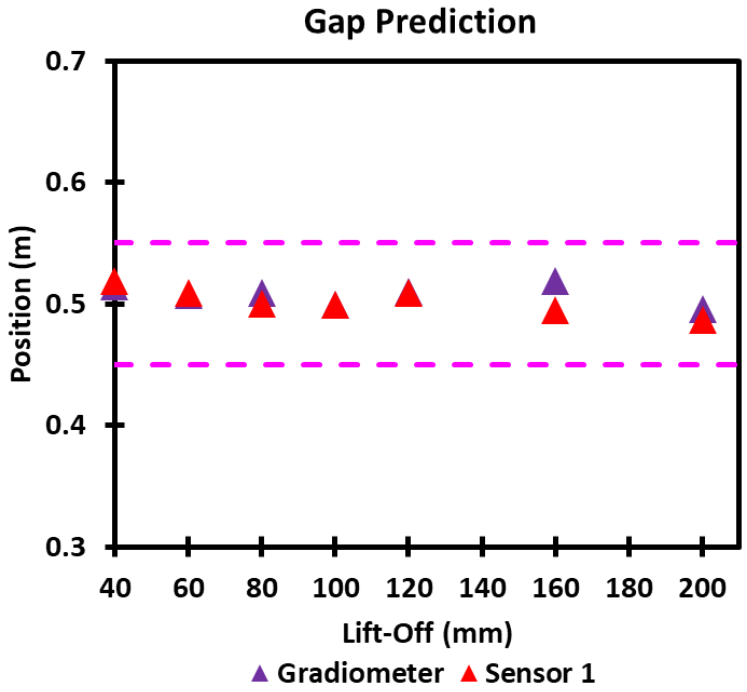

Figure 5.7: The predicted gap location for both single sensor and gradiometer. The dashed line indicates the actual gap location.

Figure 5.7 shows the results for the predicted gap location for the varying lift-offs. From the graph, I can conclude that both setups predicted location were well within the specified range. Therefore, the MTJ based gradiometric system was able to detect a gap of 10 mm at a lift-off of 200 mm.

5.2.3 Discussion

Through the investigation, the system was able to successfully detect the 10 mm gap even at a lift-off of 200 mm. The results showed that, as stated by the magnetic dipole theory and other reports [79][89], the signal weakens as the lift-off increases. Regarding the large distribution of the predicted gap location, a main factor could be from the magnetic field distribution at high lift-off. From the simulation results in Figure 5.8, I could see that the gap has caused a disturbance in the magnetic field. At low lift-off (< 150 mm), the disturbance is apparent and more define, as seen in the arrows in Figure 5.6, making it easier to identify the presence and location of the gap. In contrast, at high lift (> 150 mm), the disturbance is quite ambiguous, making it more difficult to accurately

identify the gap. Even with the improved detectivity of the gradiometer setup, the accuracy of the signal might still be influenced. Combined with the random fluctuations of the electrical noise, I deemed the error rate within ±10% is enough to compensate for the distribution of the predicted gap location.

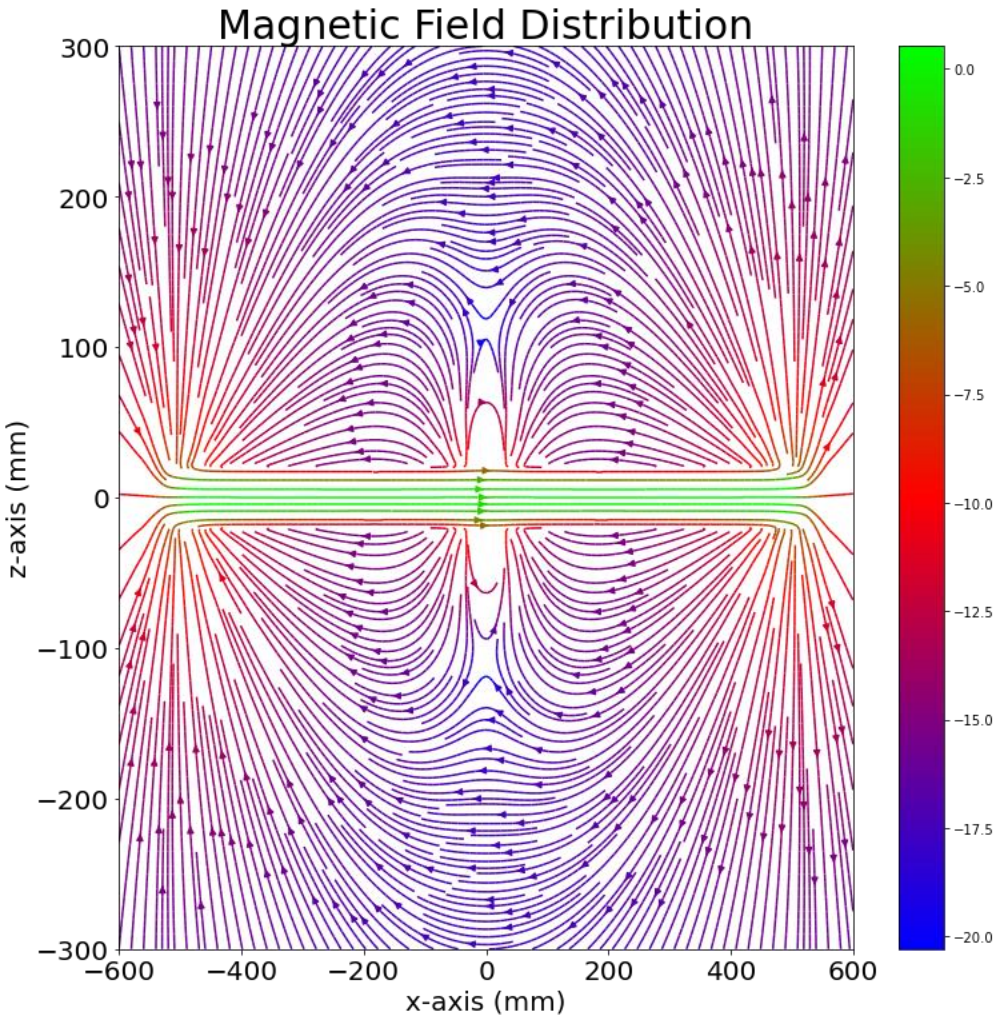

Figure 5.8: The simulated magnetic field distribution of the steel bar simulation. The steel bar condition is similar to the experiment.

5.3 200 mm Lift-off Measurement

With the confirmation that the system is able to measure at 200 mm lift-off, I next investigated whether it could measure gaps with smaller width values. I expect the system to show the same linear dependence as the previous experiments. As before, the gap width is set to a range of 1 mm ~ 10 mm.

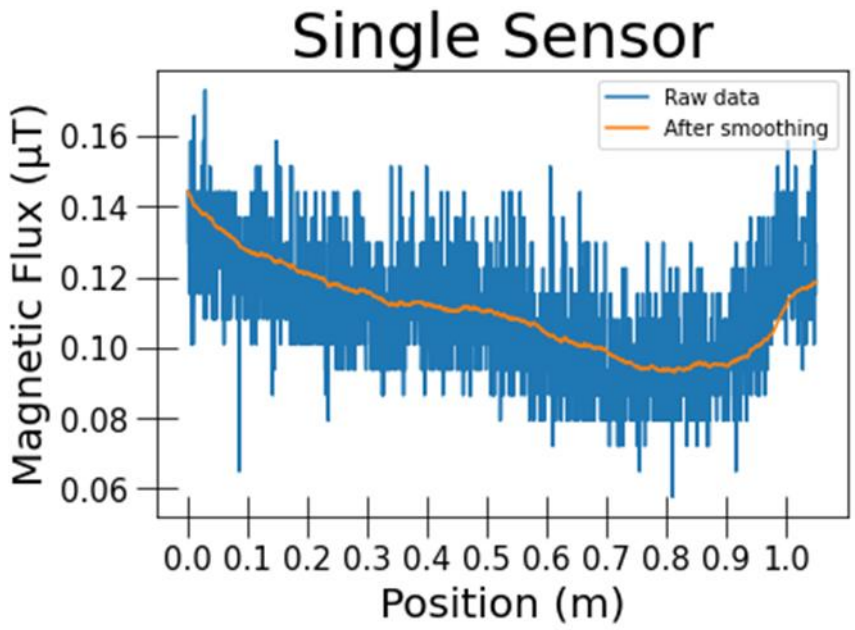

Figure 5.9: Sensor signal for gap width = 1 mm

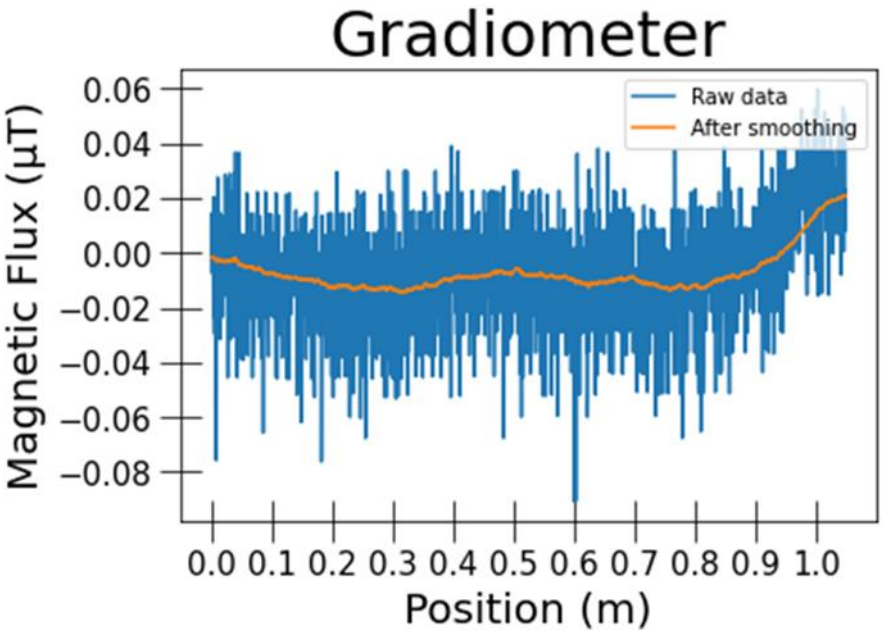

Figure 5.10: Gradiometer signal for gap width = 1 mm.

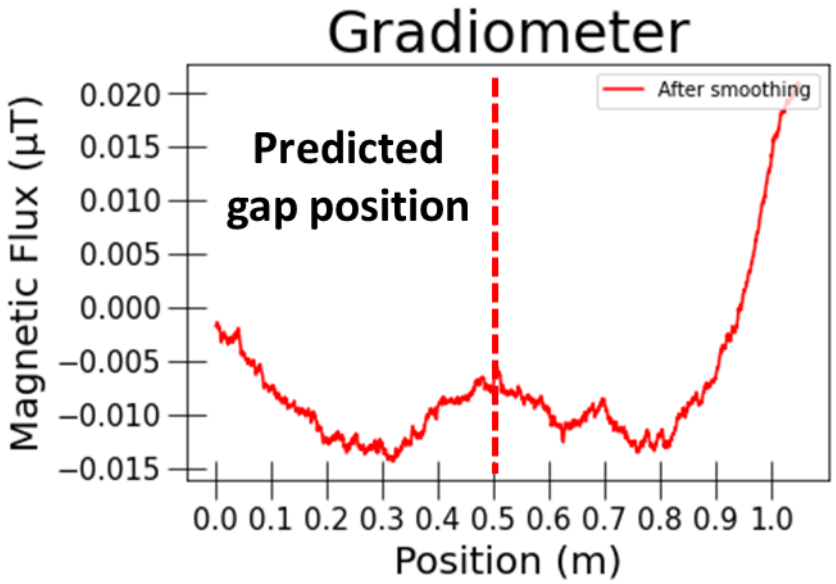

Figure 5.11: Gradiometer signal after the moving average smoothing process.

In Figure 5.9, I could see that at a gap width of 1 mm, the single sensor is unable to detect the leaked magnetic flux even at 200 mm lift-off. From the raw data it could be seen that the signal is noisy, and it is difficult to determine the exact location of the gap. Even after the moving average smoothing process, there is no clear evidence of the peak-and-trough signal caused by the gap. Through the gradiometric setup, we are able to immediately see the gaps' location due the signal changing into a signal peak signal after the smoothing process, as shown in Figure 5.10. In Figure 5.11, I isolated the signal after the smoothing process has been applied to the raw data, from there, the single peak signal was observed clearly, indicating the predicted gap position.

Figure 5.12 shows the predicted gap location for the measurements at 200 mm lift-off, and it can be seen that both setups performed well within the accepted error rate. The results confirm the ability of the designed MTJ based gradiometric sensor to detect gaps of width 1 mm at high lift-of values of 200 mm.

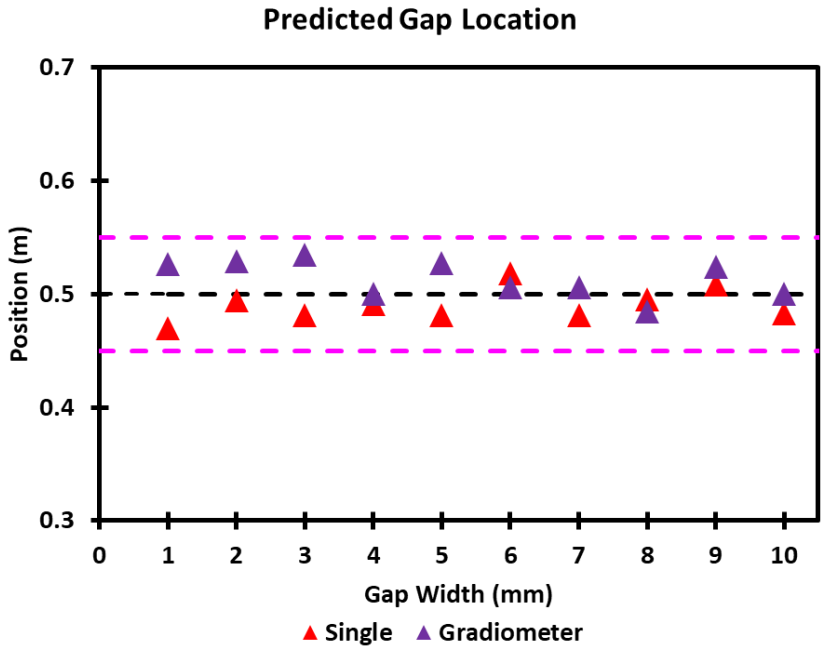

Figure 5.12: The predicted gap location for each measurement setup.

5.4 Performance Assessment Based on Simulation

From the obtained results based on the multiple measurements made and combining it with data from simulations, I was able to make a performance chart of lift-off vs gap width to predict the limit of the designed system.

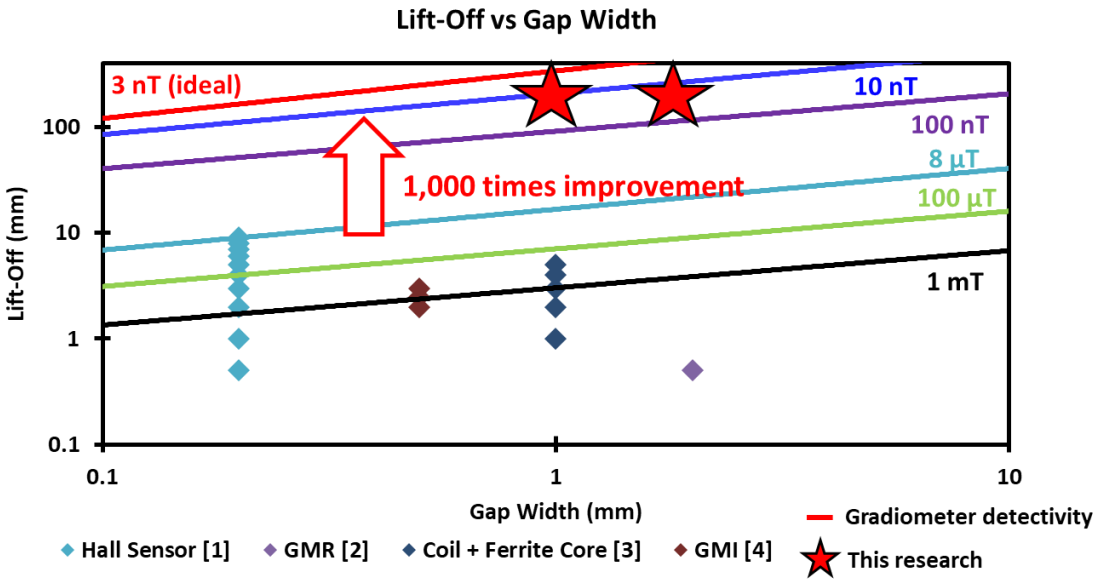

Figure 5.13: Predicted performance across different gap width vs lift-off. The solid lines show the detection limit for each respective setup. Data results from previous reports were also plotted as comparison.

By taking the gap signal value from the simulations over several gap width (0 mm ~ 5 mm) and several lift-offs (0 mm ~ 40 mm) and plotting data points based on the single sensor detectivity, gradiometer detectivity, and the measured data, was able to predict the performance ability of the different setups. Not only that, but I also compared our data with the performance of other reports using other magnetic sensors.

Based on Figure 5.13, I could predict how my designed system was able to perform at other gap width values. From the measured data line, I could assume that the system could still measure gaps even smaller than what I measured. Based on the results, the limit for gap width of 0.1 mm is at 50 mm lift-off, which is similar to the actual limit of the single sensor setup (12 nT). In contrast, since the gradiometer setup has a better detectivity (8 nT), it is able to perform better, with the predicted ability to detect gaps of 0.1 mm at 100 mm lift-off. Compared to data from other reports, my system performed better than other magnetic sensors used for non-destructive testing, such as Hall sensors [89], GMR sensors [90], coil + ferrite core sensors [91], and GMI sensors [92]. The gap width investigated in other reports are usually in the < 1 mm order and at extremely low lift-offs (< 10 mm order). Not only that, but most of them also used an electromagnetic coil to magnetize the specimens while measuring, therefore they are able to produce higher magnetic field densities, resulting higher defect signals even at low lift-off. Nevertheless, from the results in Figure 5.11, I predict that my MTJ based gradiometric system is able to detect 0.1 mm gaps at lift-off of 100 mm.

5.5 Summary

Based on the results, an increase in lift-off will result in the decrease in sensor signal, regardless of the setup. This agrees well with the magnetic dipole theory, which states that the magnetic flux density is heavily dependent on the lift-off value. As predicted, the gradiometer is able to increase the sensor signal across all lift-off values, while maintaining a larger SNR than its single sensor counterpart. Not only that, the gradiometric system was able to detect the gap location well within the accepted error rate.

With the confirmation that the system is able to measure at 200 mm lift-off, I next investigated whether it could measure gaps with smaller width values to a range of 1 mm ~ 10 mm. From the raw data we could see that the signal is noisy, and it is difficult to determine the exact location of the gap. Through the gradiometric setup, I was able to immediately see the gaps' location due the signal changing into a large signal peak signal, therefore I proved that the system shows great performance regardless of the gap width at 200 mm lift-off. By calculating the difference between the signal values from each setup, we determined how much the signal is improved. The results confirm the ability of the designed MTJ based gradiometric sensor to detect gaps of width 1 mm at high lift-of values of 200 mm.

Finally, I used the obtained results based on the multiple measurements made and combining it with data from simulations, I was able to make a performance chart of lift-off vs gap width to predict the limit of the designed system. By taking the gap signal value from the simulations over several gap width (0 mm ~ 5 mm) and several lift-offs (0 mm ~ 40 mm) and plotting data points based on the single sensor detectivity, gradiometer detectivity, and the measured data, I predicted the performance ability of the different setups. Not only that, but I also compared my data with the performance of other reports using other magnetic sensors. I was able to predict that the MTJ gradiometric system is able to detect a gap with 0.1 mm width at a lift-off value of 100 mm, which is significantly higher than previous reports, which measured gap of < 1 mm order and at lift-offs of <10 mm.

Chapter 6: Summary and Future Work

Chapter 1

This thesis aimed for the development of a MTJ based gradiometric sensor for MFL testing applications of reinforced concrete with a better performance in terms of detection, sensitivity, and efficiency. The mainstream field for MTJ sensors is in the field of memory storage and bio-medical, so this presents a challenge in terms of attempting to prove that MTJ has further applications outside of those fields and could satisfy the demands of the NDT field, in this case, being able to detect the presence and determine the location of small fracture(s). The MTJ sensors used throughout this thesis were designed and fabricated by Tohoku University's Spin Sensing Factory (SSF). Since this research focuses on the application of 2 MTJ sensor in a planar gradiometric setup, it is important that both MTJs have similar properties in order to have the same output for efficient signal increase and noise cancellation.

Chapter 2

Even though the steel bar type and size used for this research is different to in the actual concrete specimen (railway sleepers), by scaling the size down, it is easier to conduct the measurements. In reality, the concrete sleeper weighs around 300 kg, therefore it would be difficult to maneuver it around, and since the steel bars are placed inside the concrete, it would be difficult to change the size of the gap. Nevertheless, in the future, we would again conduct the experiments on a real specimen, to further proof the capability of the fabricated measurement system.

MTJ sensors have researched for their applications in various fields from memory storage to biomedical due to their high sensitivity range. Therefore, it is possible that MTJ sensors could perform as well in the low magnetic field environment of MFL testing at high lift-off. However, before measurements can conducted in real field environment, it is important that the sensors are first measured in a controlled environment to observe and understand their characteristics. I measured each sensor module to evaluate the change in resistance according to an applied magnetic field. The first MTJ sensor module

has a sensitivity of 42.321 V/mT and the second MTJ sensor modules' sensitivity is 39.734 V/mT. To be able to convert the magnetic flux density into a quantifiable quantity, the MTJ sensors resistance will change according to the magnetic flux which will cause the voltage to fluctuate. From the fluctuations, the fractures presence and location will be detectable. In this research I was able to directly observe the sensor signal by passing it through an AD converter and into a PC where all the signal processing takes place.

Chapter 3

In real field application, the measurements would be conducted in the outside environment, exposing the sensors probe(s) to various noises or disturbances. The Earth's magnetic field and equipment noise may interrupt the sensors' ability to detect the leaked magnetic flux, especially if the defect signal is small. By using a gradiometric setup, the sensors are placed in the same plane (*x*-axis), which means the magnetic noise sources would affect them with the same intensity. After subtracting the sensors output, the total magnetic noise from the sensors should be close to zero.

By measuring the response of the gradiometric setup towards a bias magnetic field with various intensity, the designed gradiometric setup was able to improve on the detectivity of the single sensor from 12 nT to 8 nT. However, as mentioned in the previous chapter, there is a slight difference in their sensitivity value, resulting in a different output for each respective sensor module at each bias magnetic field. By adjusting the sensor output through calculations, I was able to determine that in an ideal case, the systems detectivity could further be improved to 3 nT.

Another important point is regarding the difference between the noise sources, specifically magnetic noise, and electrical noise. In this experiment, the reduction of environment noise was investigated, with the bias magnetic field simulating the magnetic noise source. However, for electrical noise, in this case the noise coming from the circuitry, it is quite different, and it is independent of the bias magnetic field. Since the circuits are separate for each module, it is difficult to cancel the electrical noise.

Chapter 4

Before experimenting with the steel bar, I used simulation to determine the disturbance caused by a defect in a steel bar. The $2\Delta x$ optimization is important for the planar gradiometer because the signal depends on giving a single peak signal after subtracting the signals of sensor 1 module and sensor 2 module, by creating an overlap of the trough and peak of each respective sensors, the final gradiometer signal will create a larger single signal peak. The location of the signal peak will determine the location of the measured defect and from a practicality point of view, the single-peak signal is preferred than the peak-and-trough signal, since it is much easier to determine its precise location.

From the simulation it could be observed that the gradiometer changes the shape of the peak of the signal output from a peak-trough signal to a single peak signal, regardless of the $2\Delta x$ value. However, it was observed that there is a dependence on the value $2\Delta x$ to the change in the gradiometer signal, as shown in Figure 4.5. The gradiometer signal increases with $2\Delta x$, however, at a certain point ($2\Delta x$ = 5 cm), the signal reaches its maximum point and starts to decrease after that point. This is due to the location of the peak and trough of the single sensors are not overlapping with each other; therefore, the gradiometer signal does not increase efficiently.

Moving on to the steel bar measurements, I tried to determine the best $2\Delta x$ for out MTJ based gradiometric sensor. Initially, I tried to determine the value of $2\Delta x$ based on the peak-and-trough signal of the single sensors, since as mentioned in the previous section, the distance of the peak and trough is equal to $2\Delta x$. The results showed that the designed gradiometer managed to change the single sensor signal into a single peak for better detection, with an increase in the signal and accurate gap prediction. From my investigation, however, it is understood that in contrast to the previous report, there is no dependence on the $2\Delta x$ value on the gradiometer output, in other words, there is no optimum $2\Delta x$ value, where the output signal is at its maximum. Some of the reasons might be due to difference in lift-off values. At lower lift-off, the change in magnetic flux density is much more abrupt, therefore the slightest change in $2\Delta x$ has a large impact on

the output, while at higher lift-off, the change is less abrupt, thus allowing for a larger acceptable range of $2\Delta x$. Another factor might be due to the large sensing area of the MTJ sensors. Through simulation, it is understood that a larger sensing area will cause the p-p values of the single sensor to become broader, and this might have caused the gradiometer signal to become independent $2\Delta x$. However, from the results, it might not have a significant influence in the final signal broadening. The next factor that I considered is that for the experiment case, some parts of the steel bars are demagnetized, causing the magnetic poles to shift away from the edge of the steel bars. This results in the signal to become broader, in contrast to an ideal case from the simulations, where the magnetic poles are located at the edge, resulting in a sharp peak. Since there is no evidence of a best value for $2\Delta x$ in our results, I proceeded with choosing 140 mm as our $2\Delta x$ for the forthcoming experiments.

Chapter 5

However, in real life cases, gap width as large as 10 mm is an extreme case, therefore it is important to investigate the ability of the system to measure gaps at a smaller scale. I measured the steel bars with gap widths ranging from 1 mm ~ 10 mm, and at various lift-offs (40 mm, 60 mm, 70 mm, 80 mm, and 90 mm). Measuring at varying lift-off would also help confirm the sensors' ability to differentiate them at high lift-offs. Not only is the improvement of the sensor important, the accuracy of the predicted gap location is also vital for non-destructive testing. The error rate that I adapted throughout the measurement is $\pm 10\%$ within the actual location, i.e., between 0.45 m ~ 0.55 m, is deemed accurate.

For every measurement, it could be clearly seen that all gradiometer signals are always higher than the single sensor signal, as expected. Compared to the single sensor results, the gradiometer system performed better at increasing the overall signal (>50% increase). In addition, by observing the signal-to-noise ratio (SNR) of each respective measurement, the gradiometer constantly performed better than the single sensor setup. It was also confirmed that the MTJ based gradiometric system is able to predict the location of the gap within an error rate of $\pm 10\%$.

Next, I measured at increasing increment of lift-offs to determine the systems performance. Based on the results, an increase in lift-off will result in the decrease in sensor signal, regardless of the setup. This agrees well with the magnetic dipole theory, which states that the magnetic flux density is heavily dependent on the lift-off value. As predicted, the gradiometer is able to increase the sensor signal across all lift-off values. Not only that, the gradiometric system was able to detect the gap location well within the accepted error rate.

With the confirmation that the system is able to measure at 200 mm lift-off, I next investigated whether it could measure gaps with smaller width values to a range of 1 mm ~ 10 mm. From the single sensor data, I could see that the signal is noisy, and it is difficult to determine the exact location of the gap. Through the gradiometric setup, I was able to immediately see the gaps' location due the signal changing into a large signal peak signal, The result proves that the gradiometer performed exceptionally better, being able to detect the gap signal in a high noise and low signal environment at 200 mm lift-off. Not only that, but it can also be seen that the predicted gap position was well within the accepted error rate. The results confirm the ability of the designed MTJ based gradiometric sensor to detect gaps of width 1 mm at high lift-of values of 200 mm.

Finally, using the obtained results, I was able to make a performance chart of lift-off vs gap width to predict the limit of the designed system. By taking the gap signal value from the simulations over several gap width (0 mm ~ 5 mm) and several lift-offs (0 mm ~ 40 mm) and plotting data points based on the single sensor detectivity, gradiometer detectivity, and the measured data, I predicted the performance ability of the different setups. By comparing the data with the performance of other reports using other magnetic sensors. I was able to predict that the MTJ gradiometric system is able to detect a gap with 0.1 mm width at a lift-off value of 100 mm, which is significantly higher than previous reports, which measured gap of < 1 mm order and at lift-offs of <10 mm.

Future Work

Future work should focus on the methods to reduce the fluctuations caused by the electrical noise. I believe that most of the electrical noise comes from the circuitry that is separate for each respective module. Even though the circuits are basically the same, it could not guarantee that each electrical noise are the same, causing the gradiometer setup unable to successfully cancel it. Therefore, altering the circuit into one or using other components that have lower noise value would help reduce the noise influence on the measurement system. Another factor that should be focused on is using sensors that are identical to each other. Since the sensors have some differences in the sensitivity, their output is not the same. Ideally, both sensors must have the same sensitivity, noise base level, and detectivity, however, having all of the properties similar is quite difficult in reality. Having said that, I think that using sensors with even closer properties is next best method to proceed.

On the topic of sensors, I think that using ultra-sensitive MTJ sensors in this setup would even produce better results. During the time finishing this thesis, the collaboration between SSF and Ando Laboratory have managed to fabricate MTJ sensors that are able to detect a weak, sub-pT, magnetic field at a low frequency, demonstrating real-time measurement of MCG and NMR of protons. Therefore, I believe if we could apply them to the gradiometric system, defects with even smaller sizes could be determine at even higher lift-offs.

Improvement of the system could not only prove vital in the development of MFL testing but also in other NDT methods. This research proves that MTJ sensor has potential in various fields and hopefully the application of MTJ sensors in everyday electronic appliances will a norm in the near future.

References

[1]Sposito, G.; *et al.* A review of Non-destructive Techniques for the Detection of Creep Damage in Power Plant Steels. *NDT & E International* **2010**, *43*, 7

[2]Allin, J.; *et al.* Adhesive Disbond Detection of Automotive Components using First Mode Ultrasonic Resonance. *NDT & E International* **2003**, *36*, 7

[3]Pohl, R.; *et al.* NDT Techniques for Railroad Wheel and Gauge Corner Inspection. *NDT & E International* **2004**, *37*, 2

[4]Newman, T.; Jain, A. A Survey of Automated Visual Inspection. *Computer Vision and Image Understanding* **1995**, *61*

[5]Abend, K. Fully Automated Dye Penetrant Inspection of Automotive Parts. *SAE Technical Paper* **1998**, 980739

[6]Uhlmann, N.; *et al.* X-ray based Methods for Non-destructive Testing and Material Characterization. *2008 IEEE Nuclear Science Symposium Conference Record* **2008**

[7]Wilcox, P.; Drinkwater, B. Ultrasonic Arrays for Non-destructive Evaluation: A Review. *NDT & E International* **2006**, *39*, 7

[8]Bhagi, P.C.R. Magnetic Flux Leakage Testing: Basics. *Journal of Non-destructive Testing and Evaluation* **2012**, *11*, 3

[9]Hirose, M.; *et al*. Establishment of the Criterion in Non-destructive Test Method for Fracture of Reinforcing Steel Bar by Measuring Magnetic Flux Density. *Journal of Structural Engineering* **2012**, *58A*

[10]Hall, E. H. On a New Action of the Magnet on Electric Currents. *American Journal of Mathematics* **1879**, *2*, 3

[11]García-Arribas, A. The Performance of the Magneto-Impedance Effect for the Detection of Superparamagnetic Particles. *Sensors* **2020**, *20*, 1961

[12]Phan, M. H.; *et al.* Giant Magnetoimpedance Materials: Fundamentals and Applications. *Progress in Material Science* **2008**, *53*, 2

[13]McGuire, R.T.; *et al.* Anisotropic Magnetoresistance in Ferromagnetic 3d Alloys. *IEEE Transactions on Magnetics* **1975**, *MAG-11*, 4

[14]Tian, Y.; *et al.* Anisotropic Magnetoresistance and Weak Spin-orbital Coupling in doped ZnO Thin Films. *Applied Physics Letters* **2012**, *100*, 052408

[15]Nickel, J. Magnetoresistance Overview. *Hewlett Packard* **1995**

[16] Velev, J.; *et al*. Ballistic Anisotropic Magnetoresistance. *Physical Review Letters* **2005**, *94*, 127203

[17]Baibich, M.N.; *et al.* Giant Magnetoresistance of (001)Fe/(001)Cr Magnetic Superlattices. *Physical Review Letters* **1988**, *61*, 21

[18]Binasch, G.; *et al.* Enhanced Magnetoresistance in Layered Magnetic Structures with Antiferromagnetic Interlayer Exchange. *Physical Review B* **1989**, *39*, 7

[19]Mott, N.F. Electrons in Transition Metals. *Advances in Physics* **1964**, *13*

[20]Julliere, M. Tunneling between Ferromagnetic Films. *Physics Letters A* **1975**, *54*, 3

[21]Moodera J.S.; *et al.* Spin-polarized Tunneling in Ferromagnetic Junctions. *Journal of Magnetism and Magnetic Materials* **1999**, 200

[22]Meservey, R.; Tedow, P.M. Spin-polarized Electron Tunnelling. *Physics Reports* **1994**, *238*, 4

[23]Yuasa, S; Djayaprawira, D. D. Giant tunnel magnetoresistance in magnetic tunnel junctions with a crystalline MgO (001) barrier. *Journal of Physics D: Applied Physics* **2007**, *40*, R337

[24]Hempstead, R.; *et al.* Antiferromagnetic Ferromagnetic Exchange Bias Films. *US Patent 4* **1978**, *103*, 315

[25]Bai, R.; *et al.* Effects of Different Relevant Layers on Magnetic Properties of Bottom Synthetic IrMn Spin Valves. *Key Engineering Materials* **2013**, *562-565*

[26]Pong, P.W.T.; Egelhoff, W.F. Enhancement of Tunnelling Magnetoresistance by Optimization of Capping Layer Thicknesses in CoFeB/MgO/CoFeB Magnetic Tunnel Junctions. *Journal of Applied Physics* **2008**, *105*, 07C915

[27]Helm. D.E.; Parkin, S. Magnetoresistive Spin Valve Sensor with Improved Pinned Ferromagnetic Layer and Magnetic Recording System using the Sensor. *US Patent* **1995**, *5465185*

[28]Meguro, K.; *et al.* Spin-valve Films using Synthetic Ferrimagnets for Pinned Layer. *IEEE Transactions on Magnetics* **1999**, *35*, 2925

[29]Ruderman, R; Kittel, C. Indirect Exchange Coupling of Nuclear Magnetic Moments by Conduction Electrons. *Physical Review* **1954**, *96*, 1

[30]Butler, W. H; *et al.* Spin-dependent tunneling conductance of Fe/MgO/Fe sandwiches. *Physical review B* **2001**, *63*, 54416

[31]Meservey, R.; Tedrow, P. M. Spin-polarized electron tunneling. *Physics reports* **1994**, 238.4

[32]Parkin, S.; *et al.* Magnetically Engineered Spintronic Sensors and Memory. *Proceedings of the IEEE* 2003, *91*,

[33]Yuasa, S.; *et al.* Spin-polarized Resonant Tunnelling in Magnetic Tunnel Junctions. *Science* **2002**, *297*, 5579

[34]Nagahama, T; *et al*. Spin-dependent Tunnelling in Magnetic Tunnel Junctions with a Layered Antiferromagnetic Cr (001) Spacer: Role of Band Structure and Interface Scattering." *Physical Review Letters* **2005**, *95*, 086602

[35]Mathon, J.; Umerski, A. Theory of tunneling magnetoresistance of an epitaxial Fe/MgO/Fe (001) junction. *Physical review B* **2001**, *63*, 220403(R)

[36]Bowen, M.; *et al.* Large Magnetoresistance in Fe/MgO/FeCo(001) Epitaxial Tunnel Junctions on GaAs(001). *Applied Physics Letters* **2001**, *79*, 1655

[37]Yuasa, S; *et al.* Giant room-temperature magnetoresistance in single-crystal Fe/MgO/Fe magnetic tunnel junctions. *Nature materials* **2004**, *3*, 868

[38]Nakano, T. PhD Thesis. *Tohoku university* **2017**

[39]Bagayoko, D.; *et al*. Band structure of bcc cobalt. *Physical Review B* **1983**, *27*, 7046

[40]Parkin, S. S. P.; *et al.* Giant Tunnelling Magnetoresistance at Room Temperature with MgO (100) Tunnel Barriers. *Nature Materials* **2004,** *3*

[41]Djayaprawira, D. D.; *et al.* 230% Room-temperature Magnetoresistance in CoFeB/MgO/CoFeB Magnetic Tunnel Junctions. *Applied Physics Letters* **2005**, *86*, 92502

[42]Ikeda, S.; *et al*. Tunnel Magnetoresistance of 604% at 300 K by Suppression of Ta Diffusion in CoFeB/MgO/CoFeB Pseudo-spin Valves Annealed at High Temperature. *Applied Physics Lett*ers **2008**, *93*, 82508

[43]Fujiwara, K. 生体磁場測定用強磁性トンネル接合の作製と 微小磁場センシング. *Tohoku University* **2013**

[44]Wiśniowski, P.; *et al.* Effect of Free Layer Thickness and Shape Anisotropy on the Transfer Curves of MgO Magnetic Tunnel Junctions. *Journal of Applied Physics* **2008,** 103

[45]Kato, D.; *et al.* Fabrication of Magnetic Tunnel Junctions with Amorphous CoFeSiB Ferromagnetic Electrode for Magnetic Field Sensor Devices. *Applied Physics Express* **2013**, *6*, 103004

[46]Klement, W.; *et al.* Non-crystalline Structure in Solidified Gold–Silicon Alloys. *Nature* **1960**, *187*

[47]Fujimori, H.; *et al.* On the Magnetization Process in an Iron-Phosphorus-Carbon Amorphous Ferromagnet. *Japanese Journal of Applied Physics* **1974**, *13*

[48]Kato, D.; Fabrication of Magnetic Tunnel Junctions with Amorphous CoFeSiB Electrode for Bio-magnetic Field Sensor Applications. *Tohoku University* **2015**

[49]Umeyama, M.; *et al.* Real Time Measurement of Random Magnetization Switching in CoFeSiB Free Layer of a Magnetic Tunnel Junction. *JSAP 60th Spring Meeting* **2013**, 10–062

[50]Cubells-Beltrán, M.-D.; *et al.* Integration of GMR Sensors with Different Technologies. *Sensors* **2016**, *16***,** 939

[51]Tondra, M.; *et al.* Picotesla Field Sensor Design using Spin-dependent Tunneling Devices. *Journal of Applied Physics* **1998**, *83*

[52]Mazumdar, D.; *et al.* Field Sensing Characteristics of Magnetic Tunnel Junctions with (001) MgO Tunnel Barrier. *Journal of Applied Physics* **2008**, *103***,** 113911

[53]Negulescu, B.; *et al.* Wide Range and Tuneable Linear Magnetic Tunnel Junction Sensor using Two Exchange Pinned Electrodes. *Applied Physics Letters* **2009**, *95*, 112502

[54]Jiang, L.; *et al.* Low-frequency Magnetic and Resistance Noise in Magnetic Tunnel Junctions. *Physical Review B* **2004**, *69*, 05440

[55]Johnson, J. Thermal Agitation of Electricity in Conductors. *Physical Review* **1928**, *32*

[56]Nyquist, H. Thermal Agitation of Electric Charge in Conductors. *Physical Review* **1928**, *32*

[57]Schottky, W. Uber Spontane Stromschwankungen in verschiedenen Elektrizitatsleitern. *Annelen der Physik* **1918**, *362*

[58]George, P. K.; *et al.* Shot Noise in Low-resistance Magnetic Tunnel Junctions. *Applied Physics Letters* **2002**¸ *80*, 682

[59]Whitea, S.; *et al.* Quantative Analysis of Surface Barkhausen Noise Measurements," *AIP Conference Proceedings* **2008**, *975*, 445

[60]Kogan, S. Electronic Noise and Fluctuations in Solids. *Cambridge University Press* **2008**.

[61]Han, G.; *et al.* Magnetic Field Dependence of Low Frequency Noise in Tunnel Magnetoresistance Heads. *Journal Applied Physics* **2010**, *107*

[62]Lei, Z. Q.; *et al.* Review of Noise Sources in Magnetic Tunnel Junction Sensors. *IEEE Transactions on Magnetics* **2011**, *47*

[63]Scola, J.; *et al.* Noise in MgO Barrier Magnetic Tunnel Junctions with CoFeB Electrodes: Influence of Annealing Temperature. *Applied Physics Letters* **2007**, *90*

[64]Mazumdar, D. Low Frequency Noise in Highly Sensitive Magnetic Tunnel Junctions with (001) MgO Tunnel Barrier. *Applied Physics Letters* **2007**, *91*, 033507

[65]Nowak, E. R.; *et al.* Electrical Noise in Hysteretic Ferromagnet-Insulator-Ferromagnet Tunnel Junctions. *Applied Physics Letters* **1999**, *74*

[66]Liou, S. H.; *et al.* Dependence of Noise in Magnetic Tunnel Junction Sensors on Annealing Field and Temperature. *Journal of Applied Physics* **2008**, *103*

[67]Nor, A. F. M.; *et al.* Boron Effects on Noise in Magnetic Tunnel Junctions. *Journal of Magnetism and Magnetic Materials* **2007**, *310*

[68]Egelhoff Jr, W. F.; *et al.* Critical Challenges for Picotesla Magnetic Tunnel Junction Sensors. *Sensors and Actuators A: Physical* **2009**, 155

[69]Chaves, R. C.; *et al.* Low Frequency Picotesla Field Detection using Hybrid MgO based Tunnel Sensors. *Applied Physics Letters* **2007**, *91*, 102504

[70]Ferreira, R.; *et al.* Tuning of MgO Barrier Magnetic Tunnel Junction Bias Current for Picotesla Magnetic Field Detection. *Journal of Applied Physics* **2006**, *99*, 08K706

[71]Freitas, P. P.; *et al.* Optimization and Integration of Magnetoresistive Sensors. *SPIN* **2011**, *11*

[72]Guerrero, R.; *et al.* Low Frequency Noise in Arrays of Magnetic Tunnel Junctions Connected in Series and Parallel. *Journal of Applied Physics* **2009**, *105*, 113922

[73]Fernando Filipe Rodrigues Franco. Master's Thesis. *TECNICO LISBOA* **2014**

[74]Zhenhu Jin. PhD thesis. *Tohoku University* **2018**

[75]Koch, R. H.; *et al.* Three SQUID Gradiometer. *Applied Physics Letters* **1993**, *63*, 403

[76]Chwala, A.; *et al.* Underwater Operation of a Full Tensor SQUID Gradiometer System. *Superconductor Science and Technology* **2019**, *32*, 024003

[77]What is a SQUID – SQUIDs (google.com). Institute of Applied Science and Intelligent System "E.Caianiello", National Research Council ,Italy

[78]Hashizume A. Hironaga N. (2016) Principles of Magnetoencephalography. In: Tobimatsu S., Kakigi R. (eds) Clinical Applications of Magnetoencephalography. Springer, Tokyo.

[79]Dehui, W.; *et al.* A Novel Non-destructive Testing Method by Measuring the Change Rate of Magnetic Flux Leakage. *Journal of Nondestructive Evaluation* **2017**, *36*, 24

[80]Oogane, M.; *et al.* Sub-pT Magnetic Field Detection by Tunnel Magneto-resistive Sensors. *Applied Physics Express* **2021**, *14*, 123002

[81]Sonusen, S.; *et al.* Single layer graphene Hall sensors for scanning Hall probe microscopy (SHPM) in 3–300K temperature range. *Applied Surface Science* **2014**, *308*

[82]da Silva, F. C.; *et al*. 256-channel magnetic imaging system. *Review of Scientific Instruments* **2008**, *79*, 013709

[83]Romero-Arismendi, N. O.; *et al.* Design method for a GMR-based eddy current sensor with optimal sensitivity. *Sensors and Actuators A: Physical* **2020**, *314*, 112348

[84]Murzin, D.; *et al*. Ultrasensitive Magnetic Field Sensors for Biomedical Applications. *Sensors* **2020**, *20*, 1569

[85]Fong, L. E.; *et al.* High-resolution room-temperature sample scanning superconducting quantum interference device microscope configurable for geological and biomagnetic applications. *Review of Scientific Instruments* **2005**, *76*, 053703

[86]Hirohata, A.; *et.al.* Review on Spintronics: Principles and Device Applications *Journal of Magnetism and Magnetic Materials* **2020**, *509*, 166711.

[87]Cao, J; *et al.* Wheatstone bridge sensor composed of linear MgO magnetic tunnel junctions. *Journal of Applied Physics* **2010**, *107*, 09E712

[88]Ortner, M.; *et al.* Magpylib: A Free Python Package for Magnetic Field Computation. *SoftwareX*, **2020**, *11*, 100466,

[89]Okolo, C. K.; Meydan, T. Pulsed Magnetic Flux Leakage Method for Hairline Crack Detection and Characterization. *AIP Advances* **2018**, *8*, 047207

[90]SharatchandraSingh, W.; *et al.* Flexible GMR Sensor Array for Magnetic Flux Leakage Testing of Steel Track Ropes. *Journal of Sensors* **2012**, *2012*, 129074

[91]Wu, J.; *et al.* A Lift-Off-Tolerant Magnetic Flux Leakage Testing Method for Drill Pipes at Wellhead. *Sensors* **2017**, *17*, 201.

[92]Tehranchi, M. M.; *et al.* Double Core Giant Magneto-impedance Sensors for the Inspection of Magnetic Flux Leakage from Metal Surface Cracks. *Sensors and Actuators A: Physical* **2011**, *170*

Acknowledgement

First, I would like to express my sincere gratitude to Professor Hiroaki Matsueda as my supervisor and chief examiner, taking his time to comment and advise me in making my thesis more concise and complete. To Professor Yasuo Ando and Professor Satoshi Okamoto as my jury members for sharing their time and experience. Their advice and comments encouraged and helped in shaping a better thesis. I want to express my gratitude to Associate Professor Mikihiko Oogane, acting as my research advisor. Words are not enough to describe how grateful I am for all his teachings, comments, and ideas, which helped and inspired me not only in this research but my time in this group as well. I want to express my gratitude to Associate Professor Masakiyo Tsunoda, also as a jury member and for sharing his time, experience and valuable advises even though my research topic is different from his. The discussions and ideas during seminars provided me with new perspective.

I am thankful to Dr. Zhenhu Jin, Dr. Kosuke Fujiwara, and Dr. Al-Mahdawi Muftah for their contributions and fruitful discussions. All of them provided me with advice that paved the way for my research and helped make my experiments and research life much better. I am also grateful to Mr. Hiroshi Wagatsuma for all the healthy discussions and help concerning the electronic circuits that I have no idea in the first place. Sincere gratitude to professors and members from Graduate School in Spintronics for giving me the chance to further my studies to PhD level in Tohoku University.

I want to express my thanks to past and present members of our laboratory for all their help, teaching, discussion, and friendship. I want to thank people who were with me during conferences and travels for all the bittersweet memories.

Finally, I want to thank my mother Nor Fariza binti Ngah, my father Mohd Noor Sam bin Kasah, my brother Muhamad Afiq Ikhwan, and my sister Sofia for all their support and encouragements. To my parents thank you for everything and one day I will repay them by being a man that can make them proud, to my siblings I wish them good luck on their studies, and I will always be there for them. A great big thanks to my lovely wife Siti Masturah binti Fakhruddin for all her physical and mental support. She is my greatest joy and my greatest distraction.